Fall 2011

Laboratory studies of the physicochemical properties of mixed organic/mineral dust atmospheric aerosols: hygroscopicity and cloud condensation nuclei activity

Kelly M. Gierlus
University of Iowa

LABORATORY STUDIES OF THE PHYSICOCHEMICAL PROPERTIES OF MIXED ORGANIC/MINERAL DUST ATMOSPHERIC AEROSOLS: HYGROSCOPICITY AND CLOUD CONDENSATION NUCLEI ACTIVITY

by

Kelly M. Gierlus

An Abstract

Of a thesis submitted in partial fulfillment
of the requirements for the Doctor of
Philosophy degree in Chemistry
in the Graduate College of
The University of Iowa

December 2011

Thesis Supervisor: Professor Vicki H. Grassian

ABSTRACT

Mineral dust aerosol generated from windblown soil can contribute to climate forcing either directly through scattering or absorbing solar radiation or indirectly through acting as cloud condensation nuclei (CCN). In recent field studies organic materials, such as oxalic acid and humic-like substances (HULIS), have been shown to be present in mineral dust aerosol. The presence of these internally mixed organic compounds can alter the physicochemical properties of the dust particles in the Earth's atmosphere. Thus, in this dissertation research the hygroscopic growth and CCN activity of model humic and fulvic acids and of calcite ($CaCO_3$) particles coated with humic and fulvic acids have been measured. Furthermore, the CCN activity of calcite aerosol reacted with oxalic acid ($H_2C_2O_4$) has been measured and compared to that of the humic and fulvic acids. The CCN measurements indicate that humic- or fulvic acid-coated calcite particles are significantly more CCN active than uncoated calcite particles, whereas reacted oxalate/calcite particles are not significantly more CCN active than the unreacted calcite particles, because the enhancement in CCN activity is reduced due to the reaction of calcite with oxalic acid to yield calcium oxalate. These results show that atmospheric processing of mineral dust through surface adsorption and/or heterogeneous reactions can alter hygroscopicity and CCN activity to an extent which depends on mineralogy and chemical speciation.

Abstract Approved: _____
Thesis Supervisor

_____
Title and Department

_____
Date

LABORATORY STUDIES OF THE PHYSICOCHEMICAL PROPERTIES OF MIXED ORGANIC/MINERAL DUST ATMOSPHERIC AEROSOLS: HYGROSCOPICITY AND CLOUD CONDENSATION NUCLEI ACTIVITY

by

Kelly M. Gierlus

A thesis submitted in partial fulfillment
of the requirements for the Doctor of
Philosophy degree in Chemistry
in the Graduate College of
The University of Iowa

December 2011

Thesis Supervisor: Professor Vicki H. Grassian

Graduate College
The University of Iowa
Iowa City, Iowa

CERTIFICATE OF APPROVAL

_____

PH.D. THESIS

_____

This is to certify that the Ph.D. thesis of

Kelly M. Gierlus

has been approved by the Examining Committee
for the thesis requirement for the Doctor of Philosophy
degree in Chemistry at the December 2011 graduation.

Thesis Committee: _____
Vicki H. Grassian, Thesis Supervisor

_____
Sarah C. Larsen

_____
Mark A. Young

_____
Edward G. Gillan

_____
Gregory R. Carmichael

To my family

ACKNOWLEDGMENTS

First, I want to thank my advisor, Professor Vicki Grassian. From the beginning, your enthusiasm for this research has been contagious and has given me the inspiration to keep going. I will always be grateful for the support and encouragement you gave me over the years. Thank you also to my committee members: Professors Sarah Larsen, Mark Young, Ed Gillan, and Greg Carmichael.

Thank you also to the Grassian group members. I owe many thanks to Lizzie Gibson and Paula Hudson for training me on MAARS and to Courtney Hatch for working with me. I also want to thank Pragati Galhotra for her friendship.

Thank you also to all of the friends who have been there for me over the past few years. A special thanks to Kristina Rogers and Tim Paschkewitz. I'm not sure how I would have survived grad school without you.

Most importantly, I need to thank my family. Mom and Dad, I wouldn't be here if it weren't for the love and support you've given me my whole life. I'm not sure I could ever thank you enough. Kristen, thank you for being not just my sister, but my best friend. Greg, thank you for being a supportive brother and good friend. Joseph, you're only a couple of months old, but I'm very proud to have you for a nephew. I am so thankful for each of you. I love you more than I can put into words.

ABSTRACT

Mineral dust aerosol generated from windblown soil can participate in climate forcing either directly through scattering or absorbing solar radiation or indirectly through acting as cloud condensation nuclei (CCN). In recent field studies organic material, such as oxalic acid and humic-like substances (HULIS), has been shown to be present in mineral dust aerosol. The presence of these internally mixed organic compounds can alter the physicochemical properties of the dust particles in the Earth's atmosphere. Thus, in this dissertation research the hygroscopic growth and CCN activity of model humic and fulvic acids and of calcite ($CaCO_3$) particles coated with humic and fulvic acids has been measured. Furthermore, the CCN activity of calcite aerosol reacted with oxalic acid ($H_2C_2O_4$) has been measured and compared to that of the humic and fulvic acids. The CCN measurements indicate that humic- or fulvic acid-coated calcite particles are significantly more CCN active than uncoated calcite particles, whereas reacted oxalate/calcite particles are not significantly more CCN active than the unreacted calcite particles, because the enhancement in CCN activity is reduced due to the reaction of calcite with oxalic acid to yield calcium oxalate. These results show that atmospheric processing of mineral dust through surface adsorption and/or heterogeneous reactions can alter hygroscopicity and CCN activity to an extent which depends on mineralogy and chemical speciation.

TABLE OF CONTENTS

LIST OF TABLES

Table

LIST OF FIGURES

Figure

CHAPTER ONE

INTRODUCTION

1.1 Direct and Indirect Climate Forcing

Aerosols impact the climate through both direct and indirect forcing. Direct climate forcing involves the scatter, absorption, and re-emission of both incoming solar radiation and outgoing thermal radiation by the aerosol. Indirect climate forcing occurs through cloud droplet nucleation by cloud condensation nuclei (CCN) and the subsequent scatter, absorption, and re-emission of radiation by the droplets. Two major effects are attributed to the indirect effect. The first is the Twomey effect, which refers to the fact that increased number of CCN lead to smaller and more numerous cloud droplets leading to increased solar reflectivity. The second effect is lengthened cloud lifetimes resulting from a decrease in precipitation efficiency of the smaller cloud droplets, which in turn increases the reflectivity over the lifetime of the cloud.[1]

Figure 1-1 shows the most recent estimate of radiative forcing effects as determined by the Intergovernmental Panel on Climate Change (IPCC). Anthropogenic sources include such sources as greenhouse gases, ozone, and aerosol. The total aerosol, as shown in the Figure 1-1, includes the direct effect and the cloud albedo effect, or indirect effect. Radiative forcing is estimated at -0.9 to -0.1 W m^{-2} and -1.8 to -0.3 W m^{-2} for direct and indirect aerosol effects, respectively.[2] Both are given a negative value reflecting that they are effects which lead to the cooling of the atmosphere. The IPCC rates direct and indirect forcing as having medium to low or low levels of scientific understanding. This can also be observed by the large uncertainty shown in the reported radiative forcing contributions. In order to gain a better understanding of the radiative forcing effects of atmospheric aerosols it is necessary to better understand their compositions and hygroscopic properties.

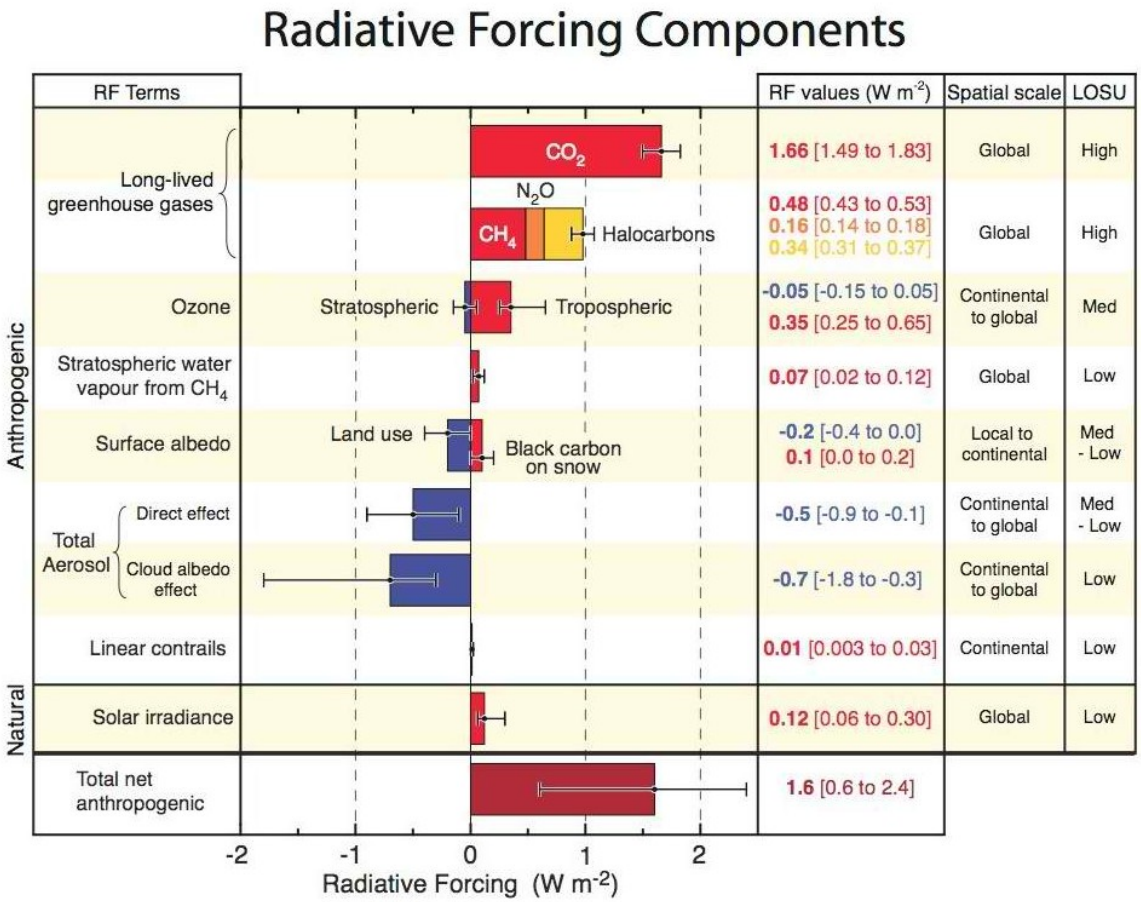

Figure 1-1 Natural and anthropogenic radiative forcing components and their estimated impact, as determined by the IPCC in 2007.[2]

1.2 Mineral Dust Aerosol

Mineral dust aerosol is generated from windblown soil at an estimated rate of 800-2000 Tg/yr.[3] The majority of this dust originates from large desert regions such as the Saharan desert in Africa or the Gobi desert in Asia, and can have atmospheric lifetimes of up a couple weeks. Figure 1-2 shows a satellite image of a dust storm off of the coast of Africa creating a plume of aerosolized dust particles over the Atlantic Ocean. Due to the long lifetimes of mineral dust aerosol produced by such storms, the aerosol can be transported globally. The exact mineralogy of the mineral dust has been shown to depend on the region from which it had originated, however, it is generally composed of clays, oxides, silicates and carbonates.[4-5]

Figure 1-2 A satellite image of dust plumes off the west coast of Africa and over the Atlantic Ocean on September 23, 2011 as captured by the Moderate Resolution Imaging Spectroradiometer (MODIS) on NASA's Terra satellite.

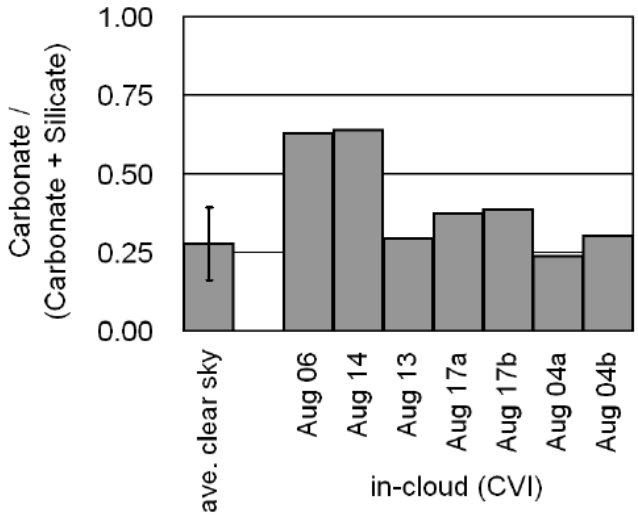

Figure 1-3 Results from a recent field study by Matsuki et al. suggest that carbonates may be significantly enriched in some cloud residual samples. From ref. 6.

Along with heterogeneous gas-phase reactions,[7-10] cloud processing has also been shown to be an important pathway for the formation of coated or internally mixed mineral dust aerosol. [6, 11] Coating of mineral dust particles can also occur through cloud processing as the particles are collected by existing cloud droplets which were nucleated by soluble particles and that dissolved soluble material is redistributed until evaporation leaves internally mixed particles. On a global average it has been estimated that any particular atmospheric aerosol has undergone the evaporation/condensation cycle three times, [12] and repetition of this cycle has been shown to significantly increase the mass of soluble material incorporated in dust particles.[13] Data from a recent field study, shown in Figure 1-3, found carbonates to be significantly enriched in cloud residual samples on Aug 06 and Aug 14 as compared to the average clear sky paricles.[6] Although there are only a few measurements it does suggest that the presence of carbonates in cloud droplets is something which should be studied further.

Mineral aerosol, like other insoluble species,[14-15] are known to be less hygroscopic and CCN active than common soluble salts, such as ammonium sulfate.[16] However, atmospheric processing resulting in the presence of more soluble coatings on clay and carbonate particles can enhance the hygroscopicity and CCN activity,[15, 17] as well as impact the location of the deposition of the dust. [18] Since large molecular weight organics are known to be associated with dust in the atmosphere,[19-21] and the presence of organic films can impact the hygroscopic properties of aerosol particles,[13, 22] organic or humic coatings on mineral aerosol can alter the climate effects of the dust particles. However, the study of water adsorption on these mixtures over the full dynamic range of water uptake from hygroscopic growth to CCN activity has yet to be explored.

1.3 Presence of Organics in Mineral Dust Aerosol

A significant fraction of tropospheric aerosols, ranging from 25% to 90%, consists of organic matter.[23-24] This is especially true in regions of high biogenic activity.[24] Considering the large amount of organic matter in tropospheric aerosols, there is still a rather poor understanding of the optical properties of such organic aerosol particles.[25-26] Additionally, work is needed to understand the role of organic compounds in the CCN activation of tropospheric aerosols, known as the indirect aerosol effect. Thus, a more well-developed description of the hygroscopicity and CCN activity of organic aerosols is needed.

The hygroscopicity and CCN activity of an aerosol particle is dependent on its chemical composition.[27-31] In the case of organic-rich particulate matter, this presents a problem because organic particles often contain hundreds to thousands of distinct chemical constituents.[32-35] A significant class of organic compounds found in atmospheric aerosols is water-soluble organic compounds (WSOC).[24, 33, 36] These compounds can dissolve into the particles and reduce the surface tension, thereby increasing the hygroscopicity of the aerosols.[28, 37-38] In contrast, the hygroscopicity of

aerosol particles could in theory be lowered by the formation of a film of water-insoluble organic compounds (e.g. fatty acids).[39]

A significant fraction of the WSOC content found in atmospheric aerosols consist of organic acids,[38, 40] including dicarboxylic acids (e.g. oxalic, malonic, and succinic acids) and tricarboxylic acids (e.g. citric and tricarballylic acids) with comparable or greater amounts of macromolecular polyacids.

1.3.1 Humic-like Substances (HULIS)

Humic substances are naturally produced by microbial oxidative degradation of plant and animal matter.[41] Humic substances are macromolecular, multifunctional organics, consisting of a heterogeneous mixture of functional groups, including aliphatic, aromatic, hydroxyl, carbonyl and carboxylic acid groups. Figure 1-4 presents the

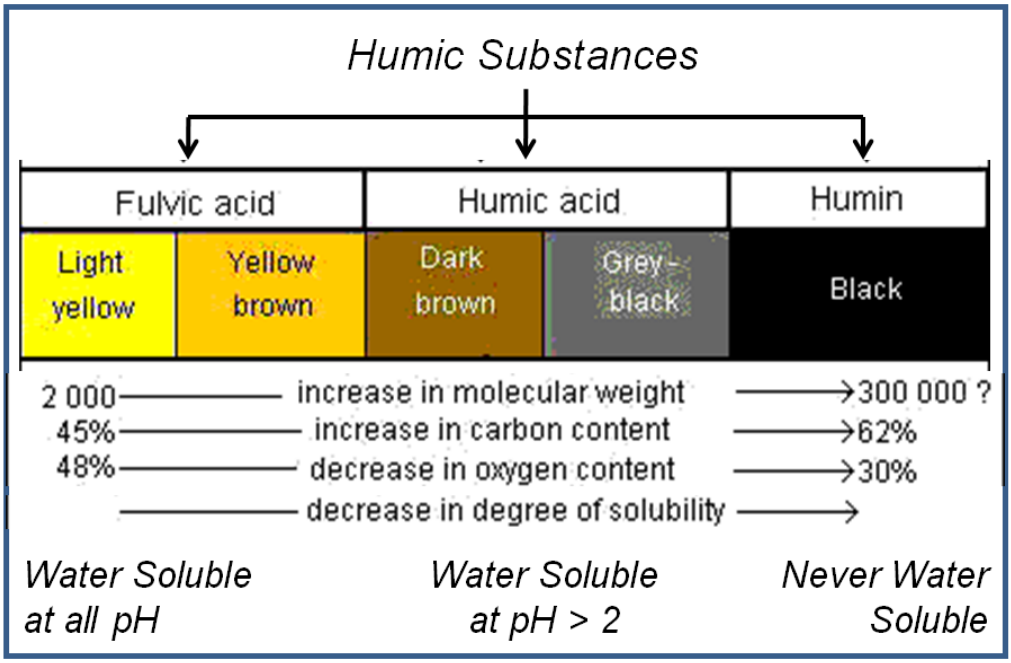

Figure 1-4 Classification of humic substances as fulvic acid, humic acid, or humin, by molecular weight, carbon and oxygen content and solubility. Adapted from ref. 42.

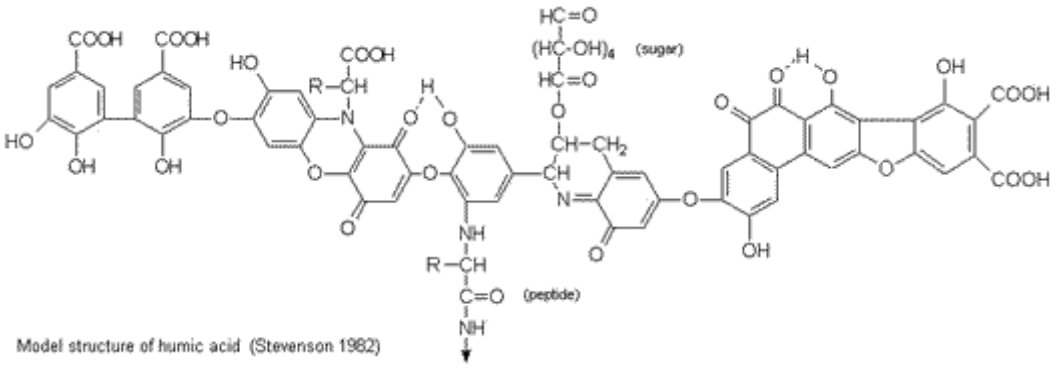

Figure 1-5 A proposed model structure of humic acid. From ref. 42.

classification of humic substances as fulvic acid, humic acid, or humin. The three types of humic substances are typically differentiated based on their water solubility, since fulvic acid is water soluble at all pH's, whereas humic acid is only soluble at pH > 2, and humin is insoluble in water. Figure 1-5 consists of a model structure for humic acid proposed by Stevenson.[42] This model demonstrates the complexity in the structures of such molecules.

Humic substances can be emitted by primary sources such as with wind-blown marine,[43-44] mineral[19, 45] and biomass burning[46-47] particles. For example, the WSOC-content of aerosols generated during Amazonian biomass burning events may be predominately composed of macromolecular, polyacids that resemble humic substances.[33, 48-49] These humic substances are often found as an internal mixture with other components such as mineral dust. It has been estimated that 6-11% of the total organic carbon extracted from urban dust samples can be attributed to humic and fulvic acids.[45]

Mayol-Bracero et al.[48] determined that polyacids accounted for up to 32% of the carbon in WSOCs extracted from biomass burning aerosol samples. It has been

suggested that the thermal degradation of plant polysaccharides (e.g. cellulose and lignin) may be a source of WSOCs, including polyacids.[33, 48] These higher-molecular weight, polyacidic, macromolecular compounds are typically referred to as Humic-like substances (HULIS), because they are in some ways similar to terrestrial and aquatic humic and fulvic acids. The infrared spectrum of fulvic acid from terrestrial systems has been shown to closely resemble that of atmospheric HULIS and WSOC-derived HULIS from dust samples.[41, 45] There are, however, differences between HULIS and aquatic and soil derived humic substances, and their relationship is not clear and has been addressed in a recent review by Graber and Rudich.[50] While some of the HULIS observed in atmospheric aerosols may arise from primary emissions of humic and fulvic acids, it is likely that secondary sources of HULIS are more significant. There are several *in situ* pathways for the formation of HULIS. These include the aggregation of lower molecular weight organic acids and mineral acids yielding supramolecular associations; and the oxidation and/or ultraviolet photolysis of humic and fulvic acids. [50] In some cases HULIS may be a complex mixture of lower molecular weight compounds[50] or an aggregate of oligomeric or polymeric compounds formed in the atmospheric aging process. Oligomer-forming heterogeneous reactions include ozonolysis,[51-52] acid-catalyzed reactions such as aldol-condensation,[53-54] photooxidation,[55-56] and Fenton chemistry.[57] Additionally, HULIS may also be produced by the sulfuric acid-catalyzed oxidation of isoprene or α-pinene.[58] The differences between HULIS and aquatic and soil derived humic substances include the fact that HULIS tends to have higher surface activity, less aromatic functionalities, weaker acidity and smaller molecular sizes than the fulvic acids[45, 50, 59]

It is clear that a better understanding of the formation pathways and chemical speciation of humic substances is needed. Moreover, due to climatic implications of these compounds arising from indirect aerosol radiative effects, a better understanding of the hygroscopic properties of this class is needed. HULIS has been found in recent studies

to comprise a significant portion of atmospheric organic aerosol[50] and expected to play an important role in cloud nucleation.[46] Approximately 60% of water soluble organic carbon (WSOC) from rural atmospheric aerosol was found to be composed of HULIS in one recent field study.[60] This suggests that HULIS may play a significant role in climate forcing by modifying optical and water adsorption properties of atmospheric aerosol.

1.3.2 Oxalate

Another significant portion of organic aerosol consists of dicarboxylic acids (DCAs). Oxalic acid, the most abundant, has been estimated to account for as much as 84% of the total DCAs. [61-67]Oxalic acid concentrations as high as 1.43 μg m^{-3} have been reported. [63] As with HULIS, one primary source is biomass burning. [68-69] Known secondary sources include the photo oxidation longer-chain DCAs. [67, 70-71] This reaction mechanism is enhanced by aqueous-phase reactions that occur in cloud droplets.[72-74] Furthermore, a recent field study suggests that maximum concentrations of oxalic acid occurred in the droplet mode. This indicates a possible association of the formation pathway with cloud-processing.[62] A number of model simulations[73, 75] and field studies[76] have reported the production of secondary organic aerosols (SOAs) to be enhanced in the presence of clouds. It has additionally been shown that fraction of oxalic acid in total WSOC concentrations increases during nighttime as compared to daytime. [63] This suggests the oxalic acid is being produced by oxidation of longer-chain DCAs in the more abundant aqueous aerosols found during the more humid nighttime conditions.

A recent study of Asian aerosol determined that on average 10% of mineral dust particles contained a detectable amount of oxalic acid. [10] Figure 1-6 shows a representation of the submicron particles studied. The samples were classified as remote marine, polluted marine or polluted dust. Each of these classifications is shown divided into the type of particles, dust, sea salt, etc. The percentage listed above the bar represents the particles containing oxalate. The distribution of particles types for the

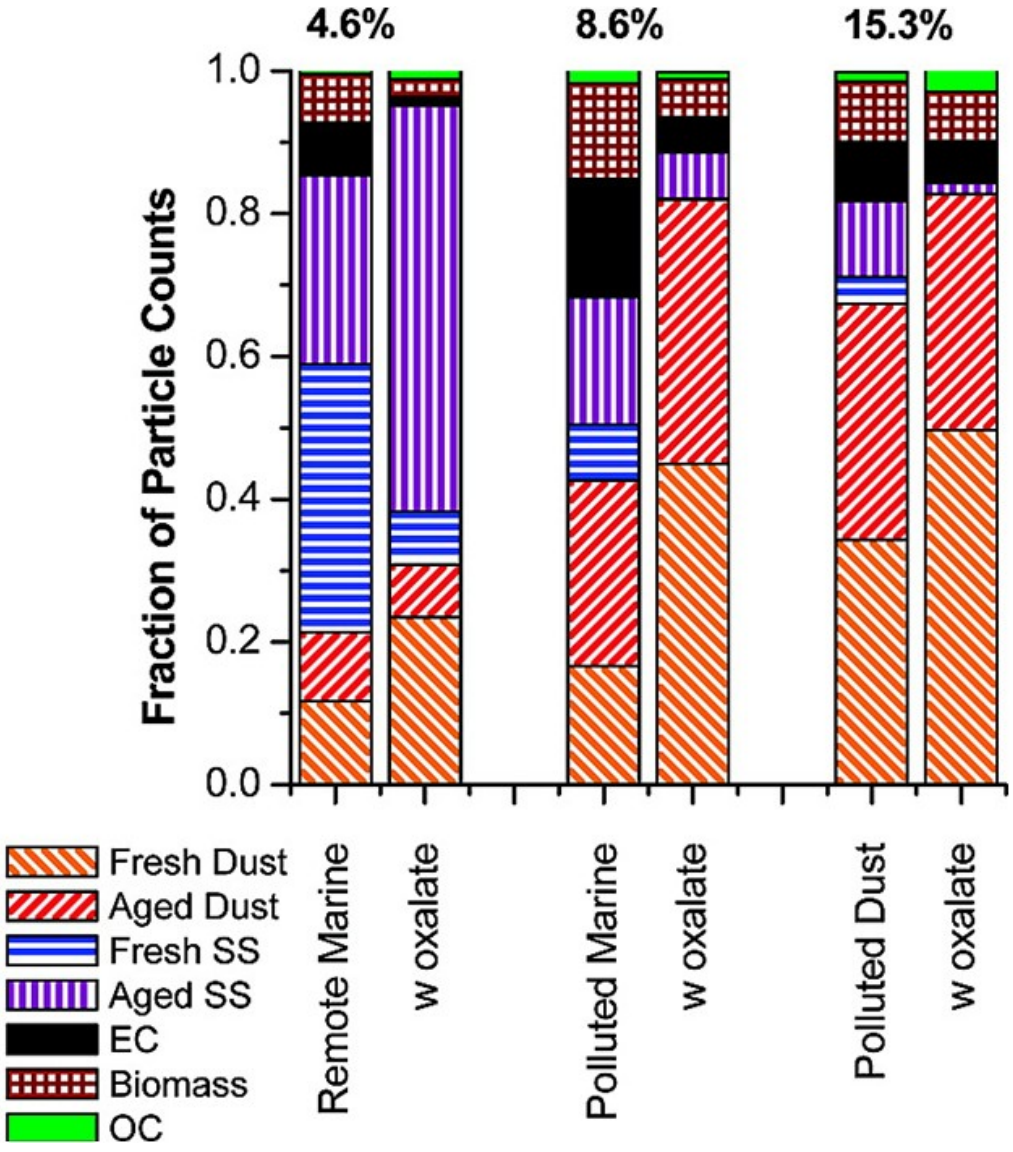

Figure 1-6 Submicron Asian aerosol categorized as remote marine, polluted marine, or polluted dust, and further divided into fresh dust, aged dust, fresh sea salt (SS), aged SS, elemental carbon (EC), biomass, or organic carbon (OC). Percentages represent the portion of each category that contained oxalate. These particles are also shown divided by type. From ref. 10.

oxalate-containing particles are also shown. In all three sample classifications, the oxalate appears to be enhanced in the dust particles. This study hypothesizes that the ability of DCAs to chelate with divalent cations such as Ca^{2+} and Mg^{2+} may be the cause of the increased concentrations. [10] Internally mixed oxalate has also been detected in other Asian dust samples, as well as Saharan dust. [21, 69] Once in contact, the oxalic acid and calcite can react to form calcium oxalate, according to:

$$CaCO_3 + H_2C_2O_4 \leftrightarrow CaC_2O_4 + CO_2 + H_2O \quad (1\text{-}1)$$

Although the CCN activity [21] and hygroscopicity [18, 77-78] of DCAs such as oxalic acid has been measured previously, it is still not clear how internally mixed DCAs may impact the climate forcing properties of mineral dust.

1.4 Thesis Outline

The purpose of this thesis is to obtain quantitative measurements of the hygroscopicity and CCN activity of internally mixed or reacted mineral dust aerosol. In Chapter Two, the experimental descriptions will be given, including a description of a Multi-Analysis Aerosol Reactor System (MAARS). MAARS is capable of measuring hygroscopicity, CCN activity, and IR extinction spectra.

In Chapter Three, the hygroscopicity of fulvic and humic acid is determined by hygroscopic tandem differential mobility analysis (hTDMA). Additionally, attenuated total reflectance (ATR) and extinction Fourier transform infrared (FTIR) spectroscopy, are used as complementary methods to the (hTDMA) studies. The measured hygroscopic growth is modeled with Köhler theory, using a single parameter, ρ_{ion}. The critical supersaturation, s_c, of fulvic and humic acid aerosol particles was determined from these Köhler curves. Finally, the hygroscopicity parameter, κ, was determined from the

hygroscopic growth measurements and compared to previously reported values based on hTDMA and CCN measurements of similar samples.

In Chapter Four, the water adsorption and CCN activity of calcite ($CaCO_3$) has been measured with and without humic coatings. Calcite was used as a model dust component because a previous study found carboxylic acids and carbonyl groups associated with $CaCO_3$ particles by mapping organic coatings on individual aerosol particles.[20] The CCN activity of pure humic and fulvic acids has also been measured. As atmospheric HULIS may have different properties depending on the source, humic acid was used as a surrogate for HULIS because it can be co-emitted with mineral aerosol. To explore the effectiveness of humic coatings on insoluble particles, the CCN activity of coated polystyrene latex spheres (PSLs) has been measured. Finally, since many studies have shown that traditional Köhler theory does not work well for insoluble particles,[14] new theoretical methods are emerging. A modified Köhler theory based on particle growth by multilayer water adsorption on insoluble particles is tested using experimental results for water adsorption on $CaCO_3$.[79]

In Chapter Five, measurements of the CCN activity of internally mixed particles generated from mixtures of either calcite ($CaCO_3$) or polystyrene latex spheres (PSLs) in an aqueous solution of oxalic acid were made. $CaCO_3$ and PSLs were used as models for mineral dust aerosol with one being a reactive component and the other an unreactive, insoluble component. Additionally attenuated total reflectance (ATR) Fourier transform infrared (FT-IR) measurements were performed to confirm speciation of oxalate in the internally mixed calcite particles.

CHAPTER TWO

EXPERIMENTAL METHODS

2.1 Abstract

In this dissertation research, the physicochemical properties of mixed organic/mineral dust aerosol have been measured using a Multi-Analysis Aerosol Reactor System (MAARS). Specifically MAARS has been used to measure hygroscopic growth and FTIR extinction spectra as a function of relative humidity (RH), as well as cloud condensation nuclei (CCN) activity of the atmospheric aerosols. Additionally, attenuated total reflectance infrared (ATR-FTIR) spectroscopy, quartz crystal microbalance (QCM) and transmission electron microscope (TEM) have been utilized as complementary techniques. Details of the above mentioned experimental techniques are discussed.

2.2 Introduction

The Multi-Analysis Aerosol Reactor System (MAARS)[80-81] has been used to measure the following physicochemical properties of aerosol particles: hygroscopic growth as a function of relative humidity (RH), extinction spectra in the infrared region, and cloud condensation nuclei (CCN) activity. A schematic diagram of MAARS is shown in Figure 2-1.

Aerosols are generated using a constant output atomizer, and then dried to a RH typically less than 10%. The polydisperse dry particles are then either directed immediately into the hydration chamber or first size selected using the first differential mobility analyzer (DMA-1). Once in the hydration chamber the aerosol may be combined with humidified air. This humidified air can be varied to condition the aerosol to RH's between 3 and 90% for size selected experiments. It should be noted, however, that for measurements requiring full size distributions (by bypassing DMA-1) it is difficult to reach a RH above 60% because of the much larger amount of aerosol flow that is mixed with the humidified air. From the conditioning chamber the aerosol flows

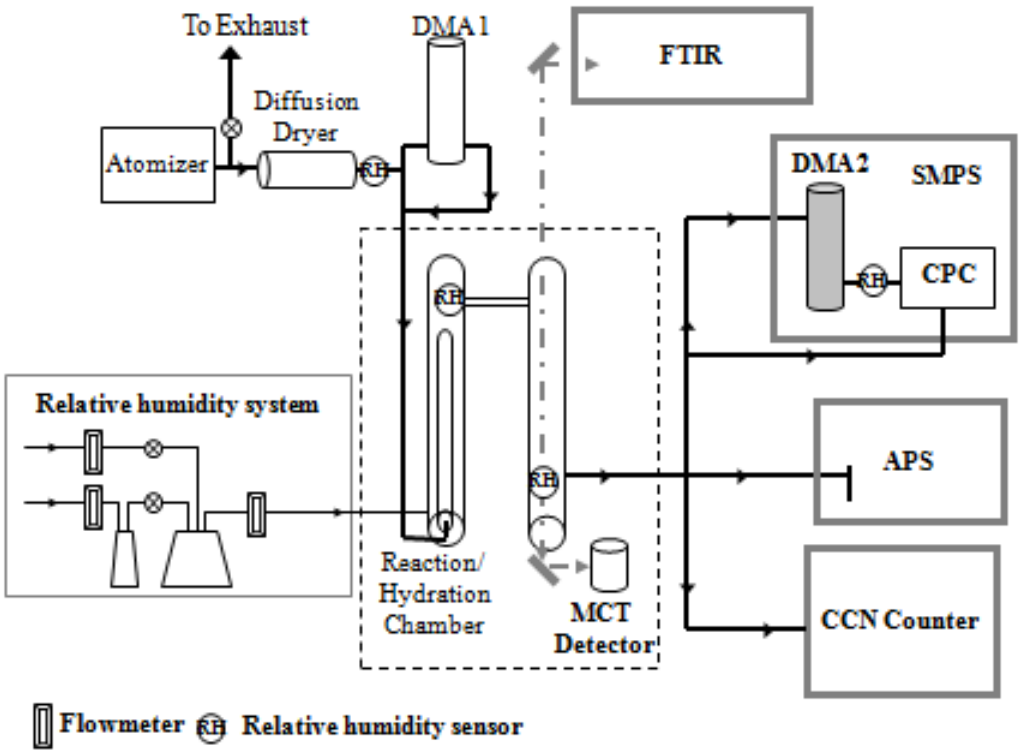

Figure 2-1 A schematic diagram of MAARS demonstrates the flow of aerosols from the atomizer through the diffusion dryer to a variety of instrumentation including a differential mobility analyzer (DMA-1) for size selection, a sizing mobility analyzer (SMPS) or aerodynamic particles sizer (APS) for measuring size distributions, a cloud condensation nuclei (CCN) counter and a FTIR spectrometer.

into an observation tube positioned along the path of an IR spectrometer, which can be used to measure the IR extinction spectra from 800 to 7000 cm^{-1}. Upon exiting the hydration chamber the aerosol can then be directed to either a continuous flow streamwise thermal-gradient CCN counter or a scanning mobility particle sizer (SMPS). For hygroscopic growth measurements, the SMPS is used to measure a particle size distribution through the use of a second DMA (DMA-2) and a condensation particle counter (CPC). The aerosol is split between the CCN counter and the CPC when measuring the CCN activity.

2.3 Chemical Materials

The following chemicals used in this study were commercially available and used as received: ammonium sulfate (ACS) obtained from Fisher Scientific, oxalic acid (99.999%) from Aldrich, calcium oxalate monohydrate (99.9985%) from Alfa Aesar, calcite from OMYA, and polystyrene latex spheres (PSLs) (Cat. #07304) from Polysciences, Inc. The following humic substances (i.e. humic and fulvic acid) used in this study were commercially available and used without further purification: humic acid sodium salt (NaHA) obtained from Sigma-Aldrich (Product #16752) and Suwannee River fulvic acid (SRFA) from the International Humic Substances Society (Denver, Colorado, USA, product #15101F). Aerosols were generated from a solution or suspension using water (Optima, Fisher Scientific).

2.4 Multi-Analysis Aerosol Reactor System

2.4.1 Aerosol Generation

Aerosol particles were generated using a constant output atomizer (TSI, Inc. Model 3076), shown in Figure 2-2. A purge gas generator (Parker Balston, Model 75-62) provides compressed air to the atomizer at a flow rate of approximately 1.5 lpm. In the atomizer assembly block, schematic shown in Figure 2-3, the stream of compressed air is

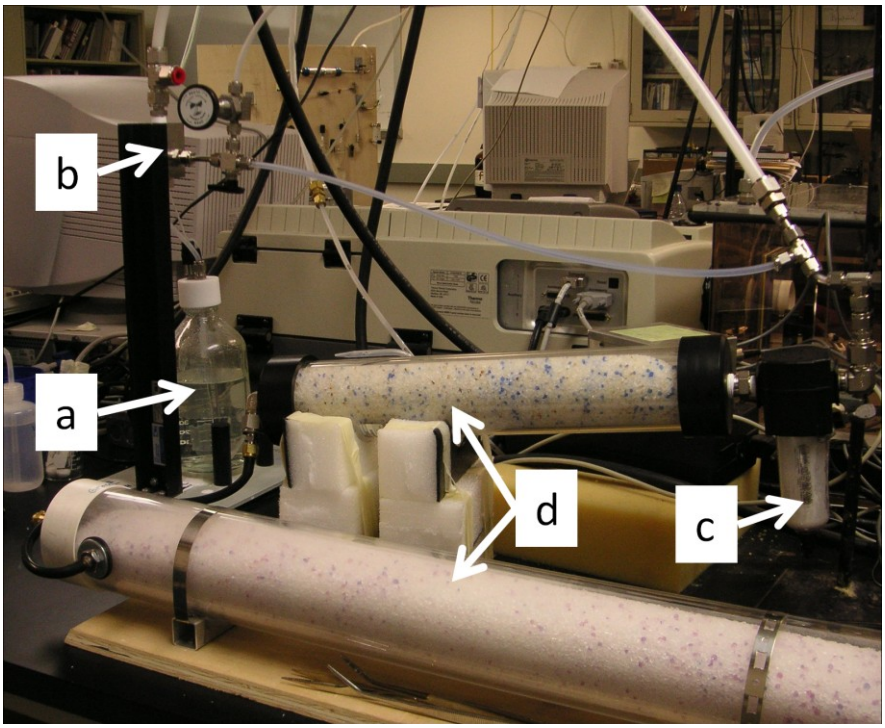

Figure 2-2 Aerosols were generated using a constant output atomizer. Aqueous samples are placed in the atomizer bottle (a), and are drawn into the atomizer assembly block (b). The droplets then exit through the top of the atomizer and are directed through a water trap (c) and two silica packed drying tubes (d).

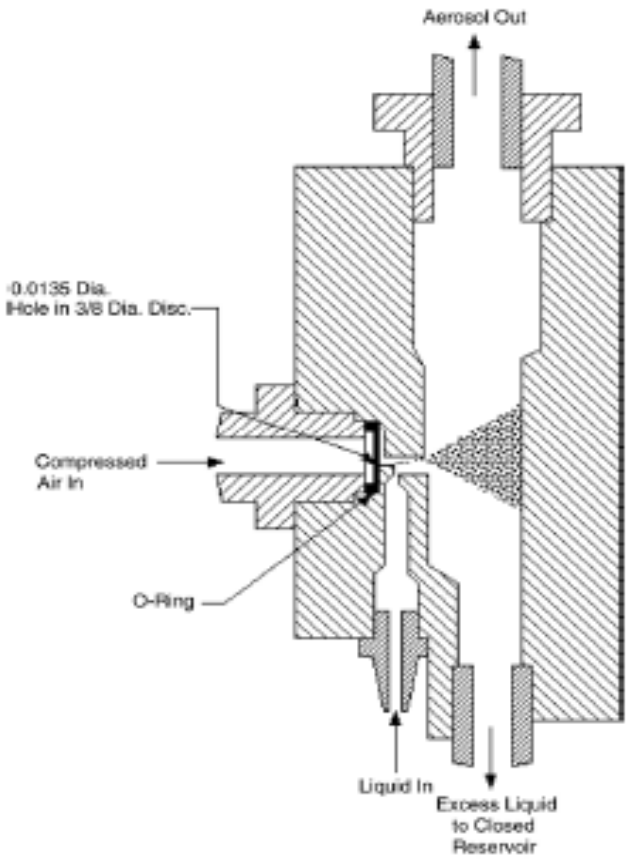

Figure 2-3 A schematic of the atomizer assembly block. From TSI, Inc.

forced through an orifice to create a jet of high-velocity air which atomizes the liquid being drawn up through a tube from the aqueous solution contained below. This polydisperse aerosol exits the top of the atomizer while an excess liquid is drained back into the atomizer bottle.

The atomizer is manufactured to produce aerosols from aqueous salt solutions. In hygroscopic growth and FTIR studies, aerosols were typically generated from either a 1 or 2 weight percent by volume (wt%) aqueous solution. In CCN studies, the concentration of the solutions ranged from 0.01-1.0 wt%. With a slight modification, the atomizer is able to generate aerosols from insoluble powders as well. This modification involves using a Pyrex test tube (Fisher Scientific, 18 × 150 mm) placed inside of the manufacturer's atomizer bottle in order to reduce the volume of solution needed. The test tube is able to hold approximately 15 mL of a suspension containing approximately 2 g of the insoluble material, usually calcite or polystyrene latex spheres (PSLs) in water or an aqueous solution. The end of the liquid feed tube is positioned at the bottom of the test tube in order to access any insoluble material that settles downwards. Tubing has also been added to ensure that any excess liquid drains back into the test tube. In order to produce internally mixed or reacted particles, the insoluble material is simply atomized in an aqueous solution of the material desired for the coating. Due to the fact that the particles are atomized in an aqueous solution this atomization technique simulates cloud-processing that particles may undergo.

Upon exiting the atomizer aerosol particles are directed to an exhaust valve that allows the flow rate to be adjusted by removing excess aerosol flow. Next the aerosol passes through a water trap to remove any large droplets. At this point the aerosols still contain a large amount of water. In order to further dry the particles, the aerosol passes through two diffusion dryers (TSI Inc., Model 3062) at which point the aerosol is dried to an RH less than 12%.

2.4.2 Particle Size Distributions

MAARS contains two differential mobility analyzers (DMA), shown in Figure 2-4, which classify aerosol particles by diameter. The first, DMA_1, is primarily used to size-select particles of a specific diameter. The second, DMA_2, is used as part of a scanning mobility particle sizer (SMPS; TSI, Inc., model 3936) to measure full size distributions. The SMPS contains an electrostatic classifier (TSI, Inc., model 3080) and a condensation particle counter (CPC; TSI, Inc., model 3025A), and is able to measure aerosol size distributions in the range of 2.5-1000 nm. Both the DMA and CPC are described in more detail below.

Upon reaching the electrostatic classifier which contains the DMA, the aerosol flow must first pass through an impactor, which is designed to remove large particles through impaction. In this work, the primary nozzle used (0.0457 cm) corresponds to a cut point diameter of 769 nm at an aerosol flow rate of 0.2 lpm, and 615 nm at an aerosol flow rate of 0.3 lpm, respectively. Next the particles flow into the Kr-85 bipolar charger, where they reach a known bipolar charge distribution.[82-83] Next, the particles enter into the top of the DMA along with a sheath flow which must be maintained at a ratio of 10:1 sheath:aerosol flow rate. The DMA, schematic shown in Figure 2-5, contains an inner metal cylinder, to which a negative voltage is applied, and an outer metal cylinder which is kept grounded. This creates an electric field through which the particles must move. Particles with a positive charge will be pulled through the sheath air towards the negatively charged inner rod. The electric mobility (Z_p), described in the following equation, determines the point at which each particle will reach the inner rod.[84]

$$Z_p = \frac{neC}{3\pi\mu D_p} \tag{2-1}$$

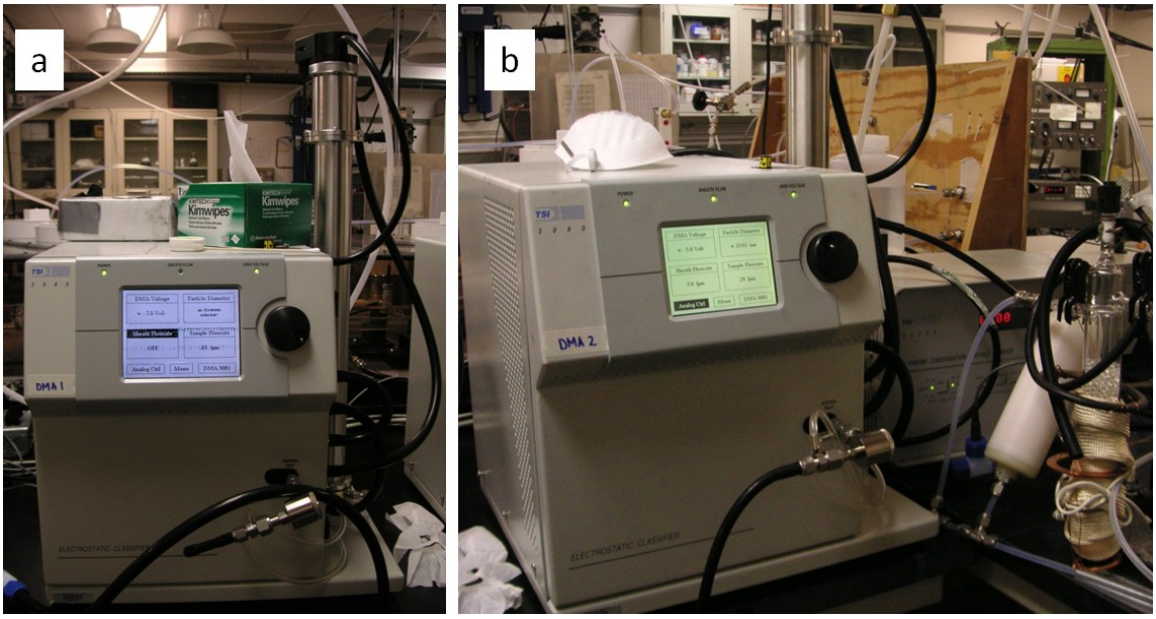

Figure 2-4 MAARS is equipped with two electrostatic classifiers which utilize differential mobility analyzers (DMA). The first, DMA-1, is used to size selected particles. DMA-2 (b) is paired with a condensation particle counter (CPC) as part of a scanning mobility particle sizer (SMPS).

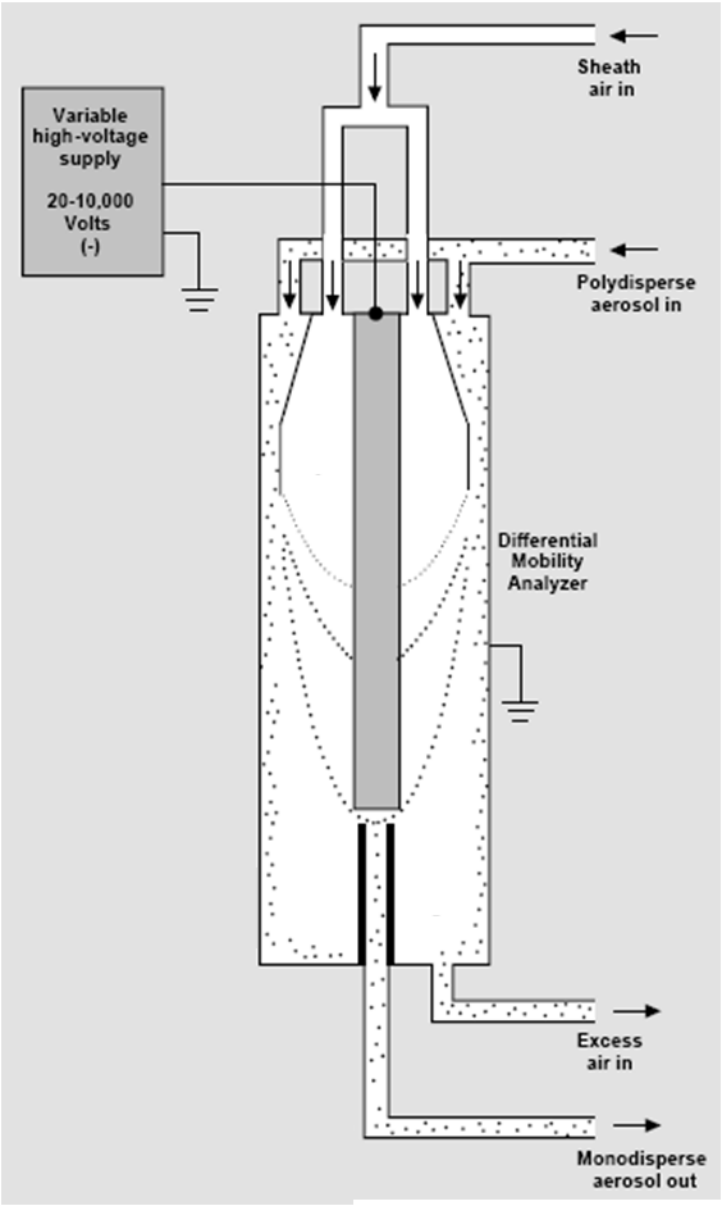

Figure 2-5 A schematic of the inside of the differential mobility analyzer (DMA). The aerosol, represented by the dots, flows in through a port on the top. Some particles are deposited on the center rod, while the monodisperse size selected aerosol exits through a slit beneath the rod, and excess flow exits at the bottom of the DMA. From TSI, Inc.

where n is the number of elementary charges on the particle, e is the elementary charge (1.602177×10^{-19} Coulomb), C is the Cunningham slip factor, μ is the gas viscosity, and D_p is the particle diameter (cm). The particle diameters that will be able to exit the DMA depends not only on the electric mobility, but also the classifier parameters, as shown below:[85]

$$\frac{D_p}{C} = \frac{2neVL}{3q_{sh}\mu \ln\frac{r_2}{r_1}} \tag{2-2}$$

where, V is the average voltage on the collector rod (Volts), L is the length between the polydisperse aerosol inlet and the exit slit (44.369 cm for the TSI model 3081 DMA), q_{sh} is the sheath flow (lpm), and r_1 and r_2 are the inner and outer radius of annular space (0.937 and 1.961 cm, respectively, for the TSI model 3081 DMA). For size-selecting particles the voltage on DMA_1 is manually adjusted on the instrument, so that particles with the corresponding mobility diameter are able to exit the DMA. Particles that are larger will exit with the excess sheath flow, and particles that are smaller will collect along the inner rod.

Size distributions can be measured using the SMPS which consists of a second DMA and a CPC, and is designed such that as the DMA scans a range of voltages, the CPC counts particles. In this case the voltage of the DMA rod is controlled by the computer program Aerosol Instrument Manager (AIM) Software (TSI, Inc. Version 5.4.0.0). The range of diameters which can be measured depends on the flow rates and the scan time. The flow rates are set manually, and are typically a sheath to aerosol ratio of either 2.0:0.2 or 3.0:0.3. The scan time is also controlled by the AIM software, and for all of the experiments described here a 210 s total scan time (180 s scanning up, 30 s scanning down in voltage) was used.

As the DMA is scanning voltages the CPC measures particle counts at each diameter. The CPC can accurately measure concentrations from 100 to 99,900 particles cm^{-3} for particles larger than 3 nm. The CPC operates by condensing a supersaturated vapor, in this case butyl alcohol (Sigma Aldrich, BT105-1L, minimum 99%). onto the particles so that they are large enough to be detected by an optical detector.

For studies in which the aerosol is exposed to humidified air, the relative humidity must be kept constant as the aerosol travels through the DMA. To ensure a constant humidity, a humidified external sheath flow is used in place of the DMA's internal sheath flow. A schematic of this is shown in Figure 2-6. The dry air for this external sheath is provided from the same air generator that supplies the atomizer. One mass flow controller (MFC, MKS Instruments, M100B) is used to control the rate of the air. It is then split with some flowing through a heated water bubbler, and some bypassing the bubbler before recombining and passing through a HEPA filter (TSI, Inc., #1602051). A valve is used to control how the air splits, and therefore the RH of the sheath flow. The

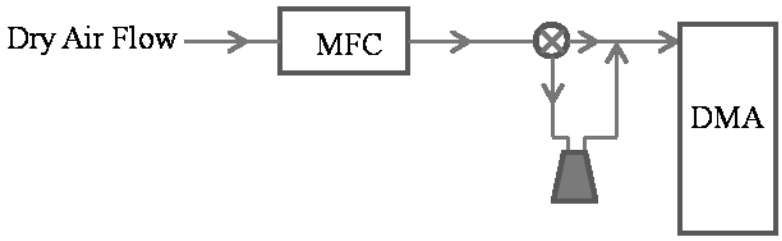

Figure 2-6 Diagram of the external sheath flow. The dry air flows through a mass flow controller (MFC). A valve is then used to control the flow of the air either directly to the DMA or first through a bubbler to humidify the air.

external sheath flow tube is then attached to the top of the DMA where the internal sheath flow tube typically is. The internal sheath flow is directed to an exhaust, along with the excess flow exiting the DMA. The RH of the sheath flow can be monitored either as it enter the DMA or between the DMA exit and the CPC entrance.

2.4.3 Cloud Condensation Nuclei Activity

MAARS utilizes a continuous flow streamwise thermal-gradient CCN counter (Droplet Measurement Technologies, Model CCN-2) shown in Figure 2-7. To measure the CCN activity the flow of a size selected aerosol is split between the CCN counter and the CPC. In this way it is possible to determine the ratio of the number of particles that act as CCN (#CCN) to the total number of particles (#CN).

A key component of the CCN counter is the saturation column. Particles enter through the top of the column and flow down the center where they are exposed to supersaturated water vapor. The supersaturation in the column is produced by the thermal gradient applied to the column with water saturated walls. Because water vapor diffuses faster than heat in air a supersaturation of water vapor occurs along the center line of the column.[86] Upon exiting the column particles that have activated droplets are counted by an optical particle counter (OPC).

A calibration must be performed in order to relate the temperature gradient (ΔT) to the percent supersaturation (%SS) of the column centerline. At a specific temperature gradient setting, the CCN activity of ammonium sulfate is measured over a range of particle diameters. This generates a CCN curve like the example shown in Figure 2-8 for ammonium sulfate at a temperature gradient of 4.85 K. Due to counting inefficiencies in the CCN and CPC, the maximum #CCN/#CN measured is typically around 0.9. All data is normalized in order to achieve a maximum at a ratio of 1. Further analysis, done using IgorPro software, includes fitting the curve with a sigmoidal curve fit. From the inflection point of this curve fit the critical diameter is determined. The critical diameter

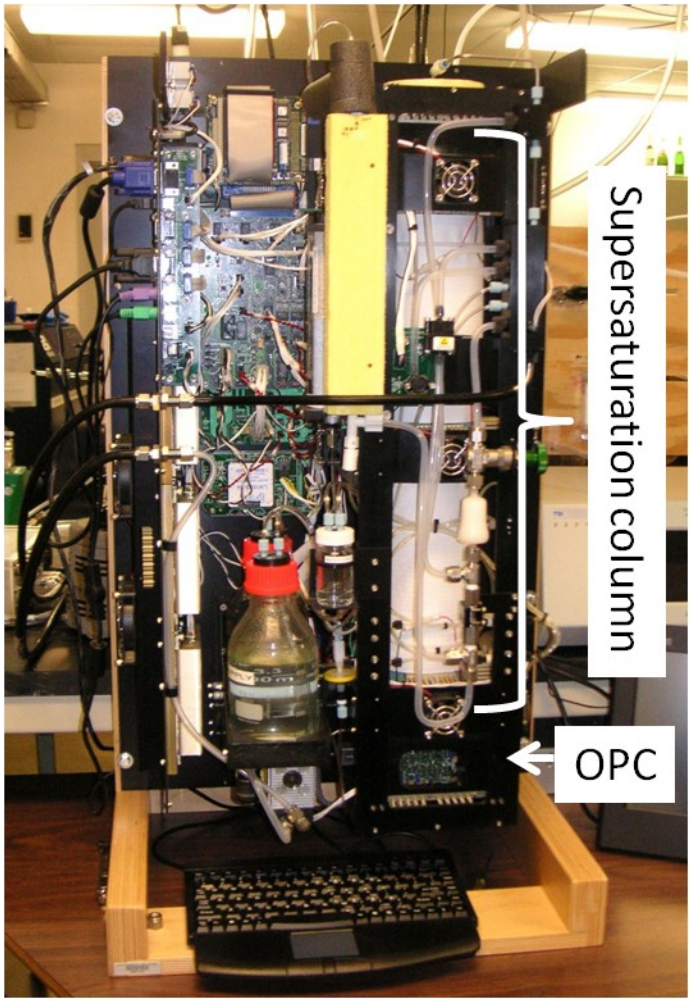

Figure 2-7 The continuous flow streamwise thermal-gradient CCN counter. The supersaturation column is placed vertically along the right side of the instruments. Below the column is an optical particle counter (OPC).

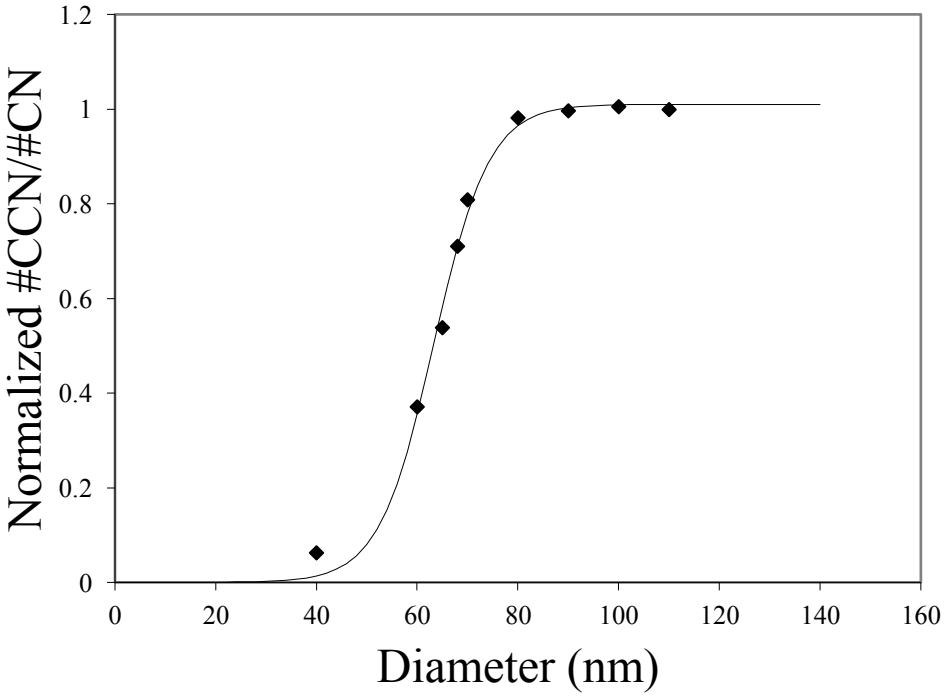

Figure 2-8 The CCN activation (#CCN/#CN) as a function of particle diameter for ammonium sulfate measured at a temperature gradient of 4.85 K. Data has been normalized to achieve a maximum #CCN/#CN equal to 1. The solid line represents a sigmoidal curve fit to the data.

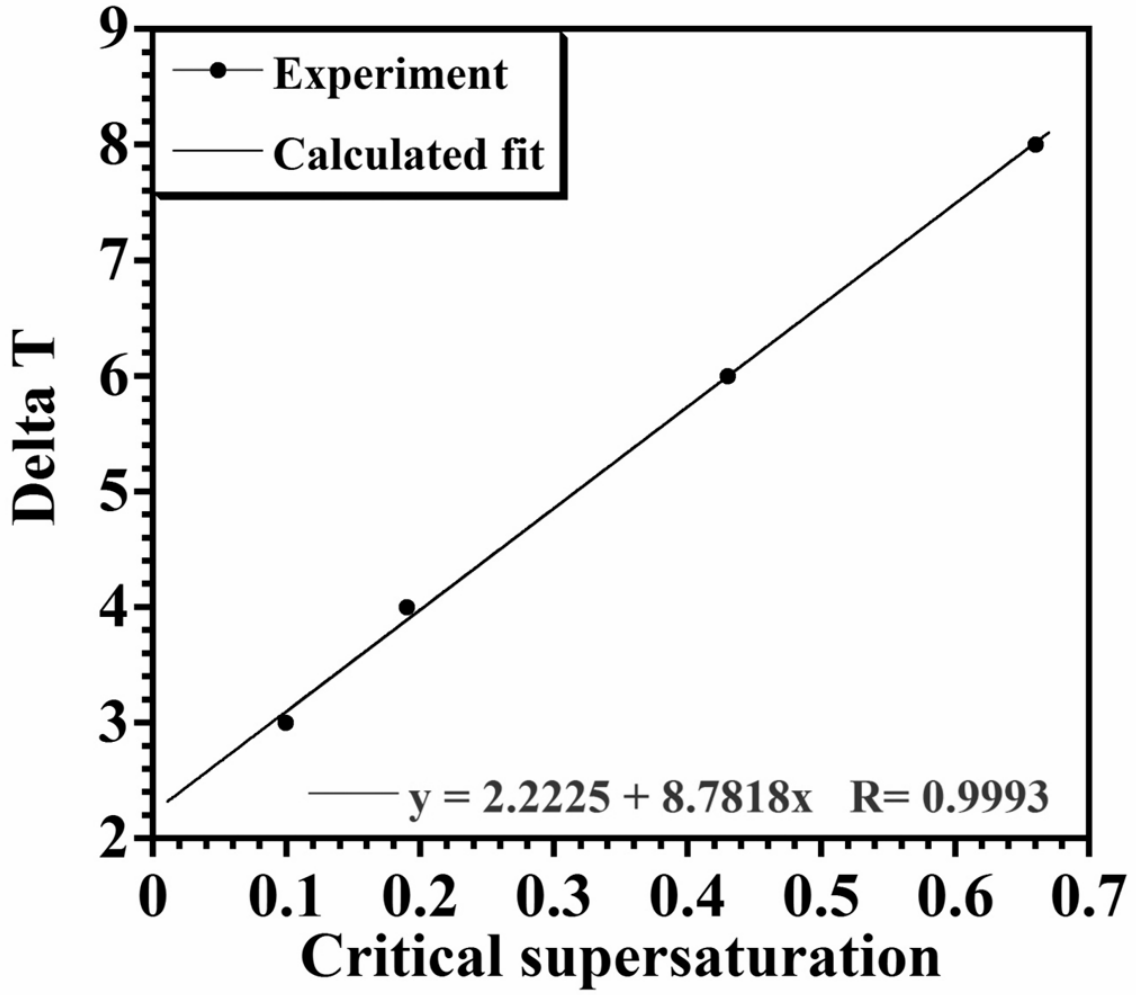

Figure 2-9 A CCN counter calibration. The critical supersaturation is calculated from the critical diameter measured at each temperature gradient.

(D_c) of an aerosol is defined as the diameter at which 50% of particles are activated for a given supersaturation. This critical diameter can them be used to calculate the %SS based on Köhler theory and the water activity data from Tang and Munkelwitz.[87] This type of measurement is done for temperature gradients of 3,4,6 and 8K and plotted versus the calculated %SS as shown in Figure 2-9. The linear fit from the calibration plot is then used by the CCN counter to convert temperature gradients to %SS.

2.4.4 Flow Hydration Chamber and FTIR Spectrometer

As shown in Figure 2-1, after exiting the diffusion dryers or DMA-1 particles may be directed through the hydration chamber. In this chamber the aerosol is mixed with either dry or humidified air. Upon leaving this chamber the aerosol flows into the observation chamber which is aligned with the beam from a Thermo Nicolet spectrometer (Nexus Model 670). An external MCT-A detector is placed at the opposite end of the chamber. All FT-IR extinction spectra are referenced a spectra obtained with the atomizer turned off. The RH is monitored by sensors (Honeywell, HIH-3602-L) in both chambers.

2.5 Complementary Techniques

2.5.1 Attenuated Total Reflectance Infrared Spectroscopy

Attenuated total reflectance infrared (ATR-FTIR) spectroscopy was used to measure the vibrational spectrum of thin films of humic substances employing a single beam spectrometer (Infinity Series, Gold Model, Mattson Instruments), equipped with a nitrogen-cooled, narrow-band HgCdTe detector. The modified ZnSe ATR horizontal liquid cell apparatus (Pike Technologies) used in this research has been described previously.[88] Aqueous samples of humic substances (1.0 wt%) were spray-deposited on a 7.3 by 0.7 cm area of the ATR-FTIR internal reflection element (IRE), resulting in a homogeneously dispersed sample, which was dried under a constant flow of air (ca. 12

hours, RH less than 5%). Spectra were obtained from 750 to 4000 wavenumbers (cm^{-1}) at 4 cm^{-1} resolution by averaging 500 scans. All ATR-FTIR spectra reported were referenced to the background signal of the blank IRE collected under dry conditions. For water absorption measurements, a humidified air stream passed through the ATR cell for 30 min. prior to making measurements to ensure equilibration, as measured by the *RH* sensor placed within the cell.

In addition, ATR-FTIR spectroscopy was used to measure the vibrational spectrum of thin films of calcium oxalate, calcite, and calcite reacted with oxalate employing a different single beam spectrometer (Thermo Nicolet, Model 6700, equipped with a nitrogen-cooled MCT/A detector). The modified ATR horizontal liquid cell apparatus used in these studies was the same mentioned above,[88] however, for these experiments an AMTIR crystal was used. For these measurements samples were spray deposited and dried as described above. Spectra were collected from 800 to 4000 wavenumbers (cm^{-1}) at 4 cm^{-1} resolution by averaging 256 scans. Again all ATR-FTIR spectra were referenced to the background signal of the blank IRE collected under dry conditions.

2.5.2 Quartz Crystal Microbalance

Gravimetric measurements were collected to quantify bulk water adsorption on $CaCO_3$ and mixtures of $CaCO_3$ with NaHA or SRFA using a 5 MHz quartz crystal microbalance flow cell (QCM 200, Stanford Research Systems) previously described in the literature.[88] The QCM measures a change in frequency that is used to determine the mass of water adsorbed to the sample. The relationship between the change in frequency, Δf (Hz), and the change in mass, Δm ($\mu g/cm^2$), is given by the Sauerbrey equation shown below:[89]

$$\Delta f = -C_f \times \Delta m \tag{2-3}$$

where C_f is the sensitivity factor, 56.6 Hz $\mu g^{-1} cm^{-2}$, specific to the 5 MHz AT-cut quartz crystal used in this study.

The samples were spray-deposited on the quartz crystal from an aqueous suspension of the sample. The suspension consisted of 2 g $CaCO_3$ in 20 mL of Optima water (Fischer Scientific) or a 0.01 wt% NaHA or SRFA solution. The deposited sample was dried with dry air, less than 5% RH, overnight. Adsorbed water was quantified by monitoring the change in frequency upon increasing the RH through the flow cell. The RH, monitored with a RH sensor (Honeywell, HIH-3602-L), was regulated by changing the ratio of wet/dry air. Each sample was allowed to equilibrate with water vapor for 30 minutes at each RH studied. The QCM quantifies adsorbed water in terms of a mass ratio of adsorbed water to the dry sample mass. The fractional monolayer coverage, assuming one monolayer is $1x10^{15}$ molecules cm^{-2}, was estimated using the measured BET surface area of $CaCO_3$.

2.5.3 Transmission Electron Spectroscopy

A transmission electron microscope (TEM: JEOL JEM-1230) was used to obtain images of various aerosol particles. These samples were prepared for imaging by exposing carbon-coated copper TEM grids (Ted Pella, Inc., Type-B, 300 mesh) to the flow of the size-selected aerosol after DMA_1.

CHAPTER THREE
WATER UPTAKE OF HUMIC AND FULVIC ACID: MEASUREMENTS AND MODELING USING SINGLE PARAMETER KÖHLER THEORY

3.1 Abstract

Humic and fulvic acids are macromolecular, multifunctional, polyacidic compounds that are important proxies for humic-like substances (HULIS), which are ubiquitous components of tropospheric particulate matter. The hygroscopic nature of these substances suggests that they can contribute to direct and indirect climate forcing. Thus, the effects of water adsorption on humic-like particles in the atmosphere must be better characterized. The water uptake of humic and fulvic acid aerosols was determined by hygroscopic tandem differential mobility analysis (hTDMA) and extinction Fourier transform infrared (FTIR) spectroscopy. Water uptake on humic and fulvic acid thin films was also investigated using attenuated total reflectance (ATR) FTIR spectroscopy. The hygroscopic growth of monodisperse, 100 nm (dry) Suwannee River fulvic acid (SRFA) and humic acid sodium salt (NaHA) aerosols was determined and modeled using Köhler theory. A single parameter, the ionic density (ρ_{ion}), which contains physical properties that are not well-established for these substances, was determined for SRFA and NaHA to be $2.1 \diamond 10^{-3}$ and $7.0 \diamond 10^{-3}$ mol cm^{-3}, respectively. The hygroscopic growth was then modeled using the ρ_{ion}-Köhler equation and the critical parameters determined. The critical percent supersaturation of SRFA and NaHA was determined to be 0.60 and 0.33%, respectively, using the surface tension of water; and 0.35 and 0.19%, respectively, using the surface tension of aqueous HULIS. κ-Köhler theory, was also used to calculate the critical supersaturation and was found to be in good agreement with the ρ_{ion} representation. Both extinction FTIR of aerosols and ATR-FTIR absorption

measurements of thin films confirm enhanced water uptake with increasing relative humidity (RH).

3.2 Introduction

Organic matter makes up a significant fraction (ca. 25–90%) of tropospheric aerosols,[23-24] particularly in regions of high biogenic activity. Despite the abundance of organic matter in tropospheric aerosols, there are still considerable limitations in understanding of the optical properties of organic aerosol particles.[25-26] Moreover, there is concern regarding the role of organic compounds in the indirect aerosol effect arising from the CCN activation of tropospheric aerosols. Thus, a more well-developed description of the hygroscopicity of organic aerosols is needed.

The hygroscopicity of an aerosol particle is dependent on its chemical composition,[27-31] which, in the case of organic-rich particulate matter, presents an inherent conundrum since most organic particles contain hundreds to thousands of distinct chemical constituents.[32-35] A significant class of organic compounds found in atmospheric aerosols is water-soluble organic compounds (WSOC).[24, 33, 36] These compounds can increase the hygroscopicity of aerosols by dissolution within the particles and by reducing the surface tension of these particles.[28, 37-38] In contrast to the effects on the hygroscopicity of particles derived from WSOC, water-insoluble organic compounds (e.g. fatty acids) could in theory lower the hygroscopicity of aerosol particles by film formation, decreasing the mass transport of water across the air-particle interface.[39]

Organic acids make up a significant contribution of the WSOC content of fine atmospheric aerosols[38, 40] including dicarboxylic acids (e.g. oxalic, malonic, and succinic acids) and tricarboxylic acids (e.g. citric and tricarballylic acids) with comparable or greater amounts of macromolecular polyacids. For example, the WSOC-content of aerosols generated during Amazonian biomass burning events may be predominately composed of high-molecular weight compounds and may have a very high polyacid

content.[33, 48-49] Mayol-Bracero et al.[48] determined that WSOCs extracted from biomass burning aerosol samples contained polyacids accounting for up to 32% of the carbon. It has been suggested that polyacids and other WSOCs may arise in-part from the thermal degradation of plant polysaccharides (e.g. cellulose and lignin).[33, 48] These higher-molecular weight, polyacidic, macromolecular compounds are typically referred to as HUmic-LIke Substances (HULIS) since they bear some similarities to terrestrial and aquatic humic and fulvic acids.

The relationship between terrestrial and aquatic humic and fulvic acids and HULIS detected in atmospheric aerosol particles is not clear and has been addressed in a recent review by Graber and Rudich.[50] Some of the HULIS observed in atmospheric aerosols may arise from primary emissions of humic and fulvic acids. For example, in one study 6 – 11% of the total organic carbon extracted from urban dust was determined to be humic and fulvic acids.[45] Other primary emission sources for HULIS, including marine emissions[44, 90] and biomass burning[47-48, 91] have been described. It is likely that secondary sources of HULIS are more significant than the contributions from primary emissions. As suggested by Graber and Rudich,[50] HULIS may be formed by several *in situ* pathways including the aggregation of lower molecular weight organic acids and mineral acids yielding supramolecular associations; and the oxidation and/or ultraviolet photolysis of humic and fulvic acids. Additionally, HULIS may be a complex mixture of poorly-resolved, lower molecular weight compounds.[50] Furthermore, recent observations of heterogeneous reactions contributing to significant yields of oligomers also suggests that HULIS may be (in part) an aggregate of oligomeric or polymeric compounds formed in the atmospheric aging process. These oligomer-forming heterogeneous reactions include ozonolysis,[51-52] acid-catalyzed reactions such as aldol-condensation,[53-54] photooxidation,[55-56] and Fenton chemistry.[57] It is clear that a better understanding of the formation pathways and chemical speciation of humic substances is needed. Moreover,

due to climatic implications of these compounds arising from indirect aerosol radiative effects, a better understanding of the hygroscopic properties of this class is needed.

In this study, the hygroscopicity of fulvic and humic acid is investigated using attenuated total reflectance (ATR) and extinction Fourier transform infrared (FTIR) spectroscopy, as complementary methods to the hygroscopic tandem differential mobility analysis (hTDMA) studies. Additionally, the hygroscopic properties of humic and fulvic acid aerosols, as determined by hTDMA, are investigated. The measured hygroscopic growth is modeled with Köhler theory, using a single parameter, ρ_{ion}. This parameter accounts for properties (i.e. density, molecular weight, osmotic coefficient, and the number of ions per solute molecule) that are not known or show high variability and unacceptable uncertainty.[92] Köhler curves for fulvic and humic acids are calculated using ρ_{ion}, with and without accounting for the respective surface tensions due to these polyacidic compounds. The critical supersaturation, s_c, of fulvic and humic acid aerosol particles was determined from these Köhler curves. Finally, the hygroscopicity parameter, κ, was determined from the hygroscopic growth measurements and compared to previously reported values based on hTDMA and CCN measurements of similar samples.

As a final note to these introductory comments, it should be emphasized that, due to the nature of humic and fulvic acids, these aerosols are inherently internally-mixed, multi-component particles and represent a proxy to HULIS. However, some key points of difference may exist between these proxies and HULIS found in atmospheric aerosols. As discussed in the review by Graber and Rudich,[50] HULIS differs from humic and fulvic acids by having a lower molecular weight and lower aromatic content. These factors and others may give rise to differences in the hygroscopic properties of HULIS and terrestrial and aquatic humic and fulvic acids. For example, HULIS typically has greater surface and droplet activation ability than fulvic acid.[50] Dinar et al.[93] have recently compared the activation of aerosols containing atmospheric HULIS to size-fractionated and non-

fractioned (i.e. bulk) aquatic fulvic acid and correlated it with the molecular weight and surface tension. The aerosol-extracted HULIS samples activated at lower diameters than both size-fractionated and bulk fulvic acid. However, due to the wide variability in the physical properties of HULIS, including the significant variability in density (1.5-1.7 g/cm^3),[91, 94] molecular weight (200-700 u),[60, 95-96] and van't Hoff factors (4.5 – 9),[95] some caution, as done here, should be applied in making a generalization regarding the comparative hygroscopicity of HULIS with fulvic and humic acids.

3.3 Experimental Methods

3.3.1 Humic Materials

The humic substances (i.e. humic and fulvic acid) used in this study were commercially available and used without further purification. Humic acid sodium salt (NaHA) was obtained from Sigma-Aldrich (Product #16752) and Suwannee River fulvic acid (SRFA) was obtained from the International Humic Substances Society (Denver, Colorado, USA, product #15101F).

3.3.2 Hygroscopic Growth Measurements

The hygroscopic growth of the humic substances was determined using the University of Iowa's *M*ulti-*A*nalysis *A*erosol *R*eactor *S*ystem (MAARS). A detailed discussion of the apparatus has been given in previous work.[80-81] hTDMA analysis was employed for growth measurements. Aerosol was generated by a constant output atomizer (Model 3076, TSI, Inc.) from an aqueous solution of 1.0 wt% NaHA or 0.5 wt% SRFA, and the particles were subsequently dried by passing the aerosol through two diffusion dryers (Model 3062, TSI, Inc.) that were maintained at a low relative humidity ($RH \leq 12\%$). The dried aerosol was size-selected in the first differential mobility analyzer (DMA_1; Model 3080, TSI, Inc.) to produce 100 nm monodisperse particles. One hundred nanometer size-selected particles were used to represent the accumulation

mode of water soluble organic carbon aerosols containing high concentrations of particulate organic matter.[97] The 100 nm particle size was verified by flowing the dry, size-selected aerosol into a scanning mobility particle sizer (SMPS; Model 3936, TSI, Inc.), which consists of a second DMA (DMA_2) coupled to a condensation particle counter (CPC; Model 3025A, TSI, Inc.). Using this method, the diameter of the 100 nm, size-selected aerosol was found to vary by ~1 nm. To measure water uptake, the monodisperse aerosol was directed to a hydration chamber and flow reactor, positioned in series, with an aerosol residence time that has been shown to be sufficient for the equilibration of water vapor with the aerosol particles.[98] After equilibration with water vapor, the aerosol was directed into the SMPS. The sheath air in DMA_2 was maintained at the same RH as the hydration chamber. The RH across MAARS was monitored by four RH sensors (Model HIH-3602-L, Honeywell). The first sensor was placed at the exit of the diffusion dryer, the second and third within the hydration chamber and flow tube, respectively, and the final sensor monitors the sheath air between DMA_2 and the CPC. These sensors have an uncertainty of $\pm$3%, with the difference in the RH between the hydration chamber/flow tube and the sheath air in DMA_2 less than 2%. Size distributions from multiple scans of the SMPS were averaged and fit to a Gaussian distribution to determine the peak mobility diameter of the wet particles, D_p. Hygroscopic growth factors, *g(RH)* were determined at each RH value using the following equation:

$$g(RH) = \frac{D_p}{D_o} \tag{3-1}$$

where D_o represents the dry particle mobility diameter.

3.3.3 Infrared Absorption Measurements

The vibrational spectra of humic substances by infrared measurements were determined on thin films and aerosol particles using ATR-FTIR spectroscopy and FTIR extinction spectroscopy, respectively. ATR-FTIR spectroscopy was used to measure the vibrational spectrum of thin films of humic substances from 750 to 4000 wavenumbers (cm^{-1}) at 4 cm^{-1} resolution by averaging 500 scans, employing a single beam spectrometer (Infinity Series, Gold Model, Mattson Instruments), equipped with a nitrogen-cooled, narrow-band HgCdTe detector. The modified ZnSe ATR horizontal liquid cell apparatus (Pike Technologies) employed in these studies has been described previously.[88] Aqueous samples of humic substances (1.0 wt%) were spray-deposited on a 7.3 by 0.7 cm area of the ATR-FTIR internal reflection element (IRE), resulting in a homogeneously dispersed sample, which was dried under a constant flow of air (ca. 12 hours, RH less than 5%). All ATR-FTIR spectra reported herein were referenced to the background signal of the blank IRE collected under dry conditions. For water absorption measurements, a humidified air stream passed through the ATR cell for 30 min. prior to making measurements to ensure equilibration, as measured by the *RH* sensor placed within the cell.

The University of Iowa's MAARS facilitates both the measurements of hygroscopic growth and FTIR extinction spectra of aerosol particles. In the case of the latter measurements, DMA_1 was bypassed, and the full distribution of aerosol (i.e. polydisperse aerosol) was directed into the hydration chamber and then into the IR cell, which is positioned along the path of the IR beam from a Thermo Nicolet spectrometer (Nexus Model 670) equipped with an MCT-B detector. FTIR extinction spectra were used to measure the vibrational spectra of aerosol organic constituents from 900 to 7000 cm^{-1} at 16 cm^{-1} resolution by averaging over 250 scans. Employing the full distribution of particle sizes gives the maximum concentration of aerosol to facilitate direct measurement of the aerosols *in situ*. Unfortunately, the RH range is limited to

approximately 10 – 65%.[80] Gas-phase water absorption bands were subtracted from all extinction spectra at the appropriate *RH*.

3.3.4 Theoretical Methods

A technique for modeling hygroscopic growth of humic substances has been developed by Wex et al.[92] that combine physical properties that are undetermined or show high variability into a single parameter, the ionic density (ρ_{ion}), defined as:

$$\rho_{ion} = \frac{\varphi \upsilon \rho_s}{M_s} \tag{3-2}$$

where φ denotes the osmotic coefficient (accounting for non-ideality of the solution), υ denotes the number of ions per solute molecule, ρ_s is the density of the solute, and M_s is the molecular weight of the solute. For humic substances and HULIS these properties are not well defined. Using Köhler theory, the water vapor saturation ratio, S, over the droplet surface can be written as follows:

$$S = \exp\left(\frac{-\rho_{ion} V_s}{n_w} + \frac{4 M_w \sigma_s}{RT \rho_w D_p}\right) \tag{3-3}$$

where V_s is the volume of the dry particle, n_w is the number of moles of water, M_w is the molecular weight of water, σ_s is the solution surface tension at the solution/air interface, R is the gas constant, T is the temperature, ρ_w is the density of water, and D_p is the wet droplet diameter. In this work, the experimental hygroscopic growth data was used to determine ρ_{ion} via the Köhler equation. This calculation is based on the assumption that the dry particle is spherical such that the moles of water, n_w, in the particle are given by Eq. (3-4).

$$n_w = \frac{\pi \rho_w}{6M_w}(D_p^3 - D_o^3) \tag{3-4}$$

Upon insertion of Eq. (3-4) into Eq. (3-3), ρ_{ion} was determined using the experimental hygroscopic growth data and an estimated upper and lower limit to the solution surface tension, represented by the surface tension of water, σ_{H2O} = 72.8 mN/m assuming a temperature of 20ºC, and the surface tension of HULIS, σ_{HULIS} = 50 mN/m, respectively.[37, 60, 92] The average of ρ_{ion} obtained from the upper and lower limits of σ was then re-incorporated into Eq. (3-3) to generate Köhler curves and obtain the critical supersaturation, s_c, required for droplet activation obtained from the maximum value of the Köhler curve. The calculated s_c was then compared to the critical value determined from another recently developed single-parameter representation of hygroscopic growth, namely "κ-Köhler theory".[99-100]

In κ-Köhler theory, the saturation ratio, S, is given by:

$$S = \left(\frac{D_p^3 - D_o^3}{D_p^3 - D_o^3(1-\kappa)} \right) \exp\left(\frac{4M_w \sigma_s}{RT\rho_w D_p} \right) \tag{3-5}$$

where κ is the hygroscopicity parameter. Eq. (3-5) is valid over the entire range of experimental RH values studied here and can be used to predict conditions for cloud droplet activation. The hygroscopicity parameter was determined from experimental hygroscopic growth data using the following equation:[99]

$$\frac{RH}{\exp\left(\frac{A}{D_o g(RH)}\right)} = \frac{g(RH)^3 - 1}{g(RH)^3 - (1-\kappa)} \tag{3-6}$$

where *g(RH)* is the growth factor obtained over a range of RH values and

$$A = \frac{4\sigma_s M_w}{RT\rho_w} \tag{3-7}$$

As with determination of ρ_{ion}, the hygroscopicity parameter was calculated based on an upper ($\sigma_{H2O)}$ and lower (σ_{HULIS}) limit to the solution surface tension.

3.4 Results and Discussion

3.4.1 Hygroscopic Growth of 100 nm NaHA and SRFA

Given the large variability in previously reported hygroscopicity measurements of humic materials, the hygroscopic growth of humic and fulvic acids was determined using hTDMA measurements. Figure 3-1a shows a plot of the hygroscopic growth of 100 nm NaHA particles upon varying the RH to 79% in terms of *g*(*RH*) compared to previously reported growth curves.[101-102] The error represents the standard deviation of triplicate measurements taken at the same RH. Continuous water uptake was observed over the range of RH values studied and deliquescent behavior was not observed. The value of *g*(*RH*) for 100 nm NaHA in our studies is slightly less than those determined by Badger et al.,[101] with the exceptions of *g*(*RH*) determined at RH values greater than 70%. Conversely, our experimental *g*(*RH*) values for NaHA are greater than those determined by Gysel et al.,[102] particularly at RH values greater than 60%. Figure 3-1b shows the hygroscopic growth of 100 nm SRFA obtained upon increasing the RH to 86%. The error represents the standard deviation of triplicate measurements. The hygroscopic

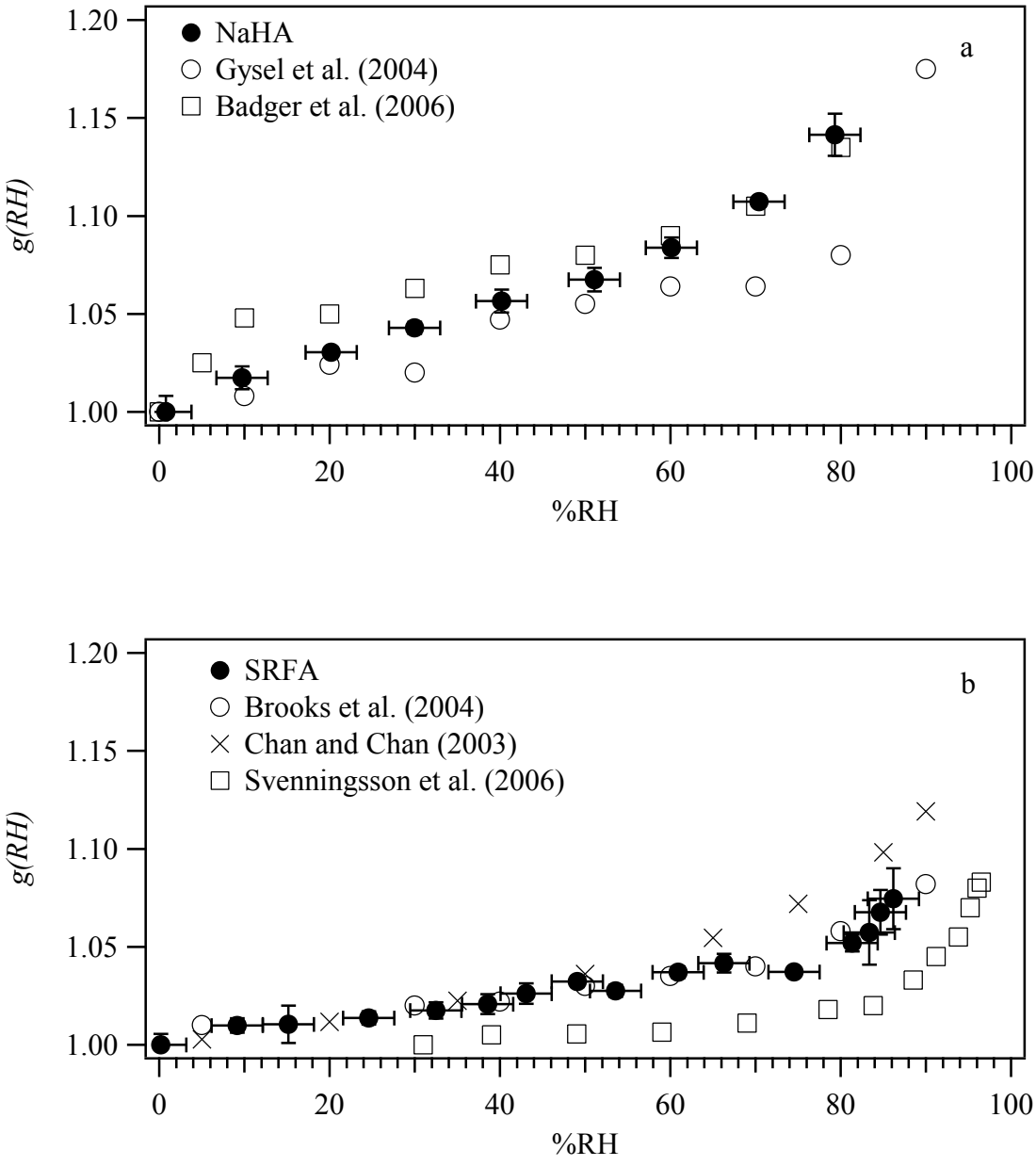

Figure 3-1 hTDMA measured hygroscopic growth of 100 nm (a) NaHA and (b) SRFA. Results from the current study are compared to previous measurements. The error bars represent the standard deviation of triplicate measurements.

growth behavior is similar to that reported by Brooks et al.[103] However, our experimental $g(RH)$ for SRFA was greater than that determined by Svenningsson et al.[104] for all values of RH. Conversely, for RH ca. 30% and greater, $g(RH)$ was less than that determined by Chan and Chan.[28] Thus, for both growth curves, the experimental values reported here fall within the range of previously reported growth curves.

While the hygroscopic growth of both SRFA and NaHA was in good overall agreement with previous studies, the differences between these studies merits consideration. Since the previously reported studies[101-102] use the same technique and dry diameter of NaHA (100 nm) as in the present study, the slight variability in measurements is likely not due to differences in particle size or technique. However, it is conceivable that the material is likely to show variability being a technical grade product (Aldrich, No. H16752), which is isolated from crude lignite. The significant variability of batch-to-batch composition of commercial humic substances, such as ash content, has been described previously,[105] and may contribute to the differences in hygroscopic growth. Additionally, differences in the pretreatment (e.g. filtration) of the humic acid solutions prior to atomization may further contribute to differences in the reported hygroscopic growth measurements. The hygroscopic growth of 100 nm SRFA was also found to slightly deviate from previous measurements.[28, 104] In particular, results previously reported by Svenningsson et al.[104] are sharply different than the results of the present work. Previous hygroscopicity measurements by Brooks et al.[103] showed that particle size has little effect on hygroscopic growth and given that previous hTDMA measurements were performed on 100 nm particles, with the exception of Chan and Chan[28] who measured hygroscopicity using an electrodynamic balance (EDB), variations in particle size is likely not responsible for the discrepancies shown in Fig. 1b. Thus, the variation of the growth curves reported by Svenningsson et al.[104] compared to other reported measurements and the work herein could be due to batch-to-batch variability of the SRFA standard materials or differences in conditioning time at the reported RH.

3.4.2 Calculation of Critical Supersaturation from Hygroscopic Growth

The s_c of NaHA and SRFA were calculated using the ρ_{ion} parameterization of Köhler theory and κ-Köhler theory and ρ_{ion} is reported in Table 3-1. The ionic density, ρ_{ion}, was calculated from the hygroscopic growth data using Eq. (3-3) as described previously for each RH at which growth was measured. An average ρ_{ion} value was obtained using the upper and lower limit to the surface tension. It should be noted that the variation in ρ_{ion} calculated using the two different surface tension values was within error of the calculated mean value reported below and did not show a significant dependence on the choice of surface tension, as shown in Table 3-1. Thus, the ρ_{ion} parameter is not sensitive to the surface tension used in the calculation. However, some variation in ρ_{ion} was observed with increasing RH; therefore, a dependence of ρ_{ion} on the acid concentration is implied. However, since ρ_{ion} was specifically determined for use in Köhler theory calculations to determine s_c, only the values of ρ_{ion} determined under the most dilute conditions were used in all subsequent calculations. The average values for ρ_{ion} in this

Table 3-1 Calculated ρ_{ion} values averaged for the most dilute solutions measured for NaHA and SRFA samples based on the choice of surface tension used compared to the mean ρ_{ion} value.

	ρ_{ion} (mol cm^{-3})
NaHA (σ_{H2O})	$6.9\text{x}10^{-3}$
NaHA (σ_{HULIS})	$7.0\text{x}10^{-3}$
NaHA (*average*)	$(7.0\pm0.3)\text{x}10^{-3}$
SRFA (σ_{H2O})	$2.12\text{x}10^{-3}$
SRFA (σ_{HULIS})	$2.06\text{x}10^{-3}$
SRFA (*average*)	$(2.09\pm0.07)\text{x}10^{-3}$

σ_{H_2O} = surface tension of water (72.8 mN/m)

σ_{HULIS} = surface tension of HULIS (50 mN/m)

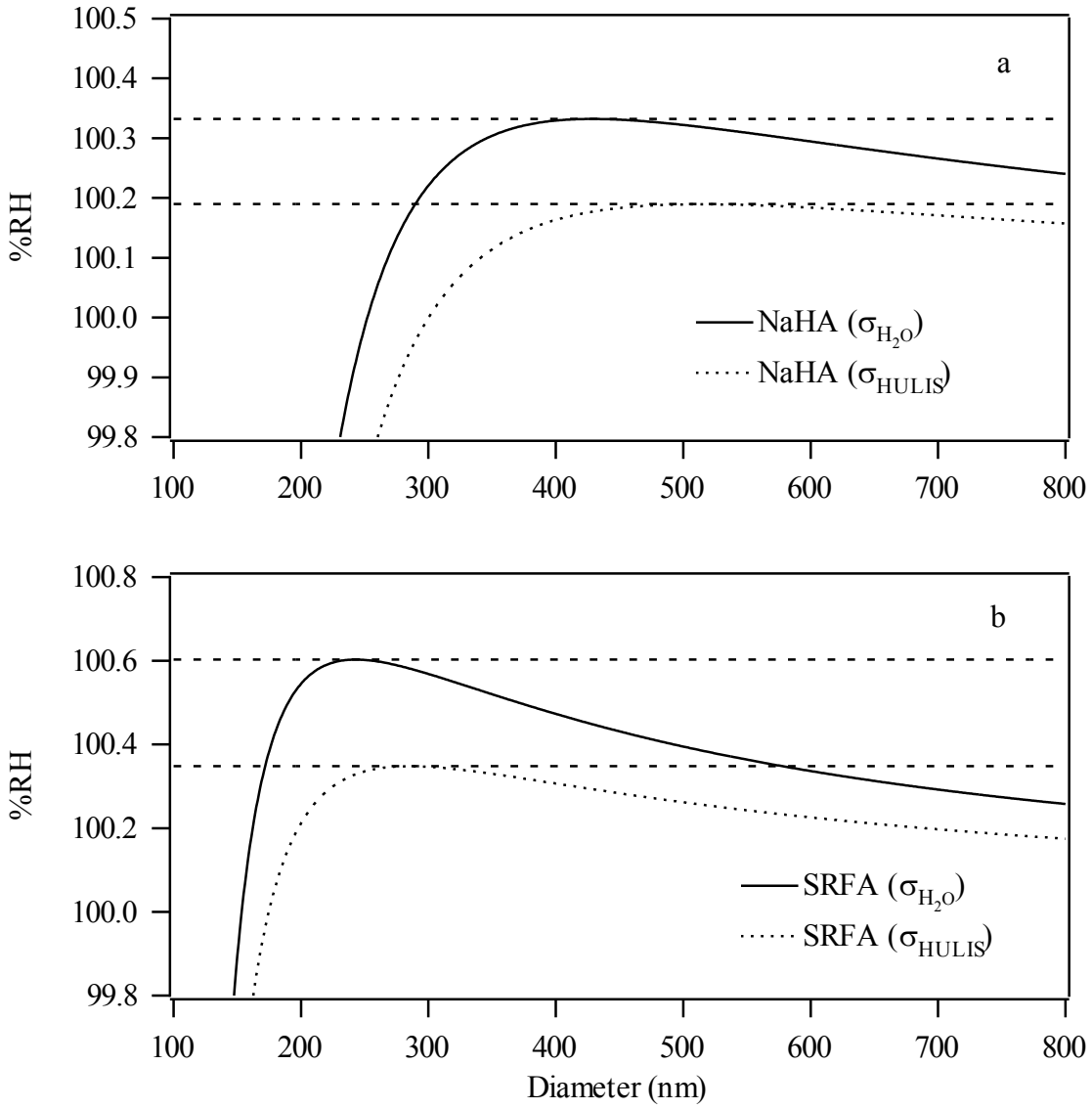

Figure 3-2 Köhler curves for 100 nm (a) NaHA and (b) SRFA, calculated using the average value of $\rho_{ion.}$ Solid and hatched lines denote calculations using ρ_{ion} assuming the surface tension of water and HULIS, respectively. Extrapolations indicate the critical saturation ratio.

Table 3-2 The critical supersaturation (%) determined using single-parameter Köhler theories based on experimental hygroscopic growth data.

	Critical Supersaturation (%)	Critical Supersaturation (%)
100 nm NaHA	when σ_{H2O} = 72.8 mN/m	when σ_{HULIS} = 50 mN/m
ρ_{ion} = 7.0x10^{-3} mol/cm^3	0.33	0.19
κ = 0.138 (RH=79%)	0.32	0.18
100 nm SRFA		
ρ_{ion} = 2.1x10^{-3} mol/cm^3	0.60	0.35
κ = 0.044 (RH=86%)	0.57	0.33

high RH range are (7.0±0.3)x10^{-3} and (2.09±0.07)x10^{-3} mol cm^{-3} for NaHA and SRFA, respectively at the 95% confidence level. In comparison, Wex et al.[92] have reported average values of the ionic density of HULIS (extracted from urban aerosols) of 5.55◈10^{-3} and 4.85◈10^{-3} mol/cm^{-3} at 95% RH using σ_{H_2O} and σ_{HULIS}, respectively. Interestingly, ρ_{ion} of HULIS is nominally close to the mean value of the average ionic densities of NaHA and SRFA calculated in this study. This indicates that HULIS may have intermediary hygroscopicity relative to SRFA and NaHA, supporting the role of these materials as proxies for HULIS.

Figures 3-2a and b depict the Köhler curves calculated for NaHA and SRFA, respectively. To generate the Köhler curves shown in Figure 3-2, the ρ_{ion} value averaged over the highest RH values in which growth was measured was used. These values, reported above for NaHA and SRFA, were incorporated into Eq. (3-3) using an upper and lower limit to the surface tension, represented by σ_{H_2O} and σ_{HULIS}.[92] The Köhler curves hown in Fig. 3-2 were then used to determine s_c values which are summarized in Table 2.

Another recently developed single-parameter representation of Köhler theory, the κ-Köhler theory, was used to estimate the critical supersaturation of 100 nm NaHA and SRFA aerosol particles. From the hygroscopic growth data, the parameter κ was calculated using Eq. (3-6). The κ value was found to vary as a function of RH, particularly at low RH where Köhler theory is not valid. However, at the highest RH values studied here, 79% and 86% RH for NaHA and SRFA, respectively, minimal changes in the κ value were observed. Thus, only the κ values obtained under the most dilute conditions are reported here. Similar to the single-parameter ρ_{ion} value, the calculated κ values showed no dependence on the choice of surface tension used in Eq. (3-6). Thus, it can be concluded that the single parameters, κ and ρ_{ion}, are insensitive to the surface tension and thus can be determined using the more widely known σ_{H_2O} value. However, the use of Köhler theory to determine critical parameters based on κ and ρ_{ion} values is much more sensitive to the choice of surface tension, as observed in Figure 3-2 and discussed below.

The calculated hygroscopicity parameters are summarized in Table 3-2. The value of the κ parameter obtained at 86% RH for dilute SRFA aerosol particles was 0.044. This is in good agreement with values listed in Petters and Kreidenweis,[99] with growth factor-derived mean values for κ of 0.056 and 0.044, and CCN-derived mean values of 0.067, 0.056, and 0.033. Additionally, the value for κ for the 100 nm SRFA was in fairly good agreement with the CCN-derived value of 0.026 for 235 nm particles in an earlier work.[30] The κ value obtained at 79% RH for dilute NaHA was 0.138, which is more than a factor of two greater than the CCN-derived value reported for 235 nm particles of 0.047 by Hatch et al.[30] The difference between this work and the CCN-derived values by Hatch et al.[30] could be due to non-ideal conditions at 79% RH. It is assumed that the κ value will continue to decrease upon further droplet dilution. Thus, the value reported here must be considered as an upper limit. It should be noted that the larger κ value derived for NaHA *vs*. SRFA (*c.f.* 0.138 *vs*. 0.044) corresponds with the greater hygroscopicity of the sodium

salt compared to the protonated polyacid, SRFA, and is similar to κ values obtained from other important organic acids found in the atmosphere, such as glutaric, glutamic and pinonic acids.[99] It is still unclear as to whether the κ values obtained for humic and fulvic acids is representative of HULIS observed in atmospheric particles as κ values have yet to be determined for real HULIS.

Table 3-2 summarizes the calculated s_c values determined from the maximum of the generated Köhler curves and the values of the parameters (ρ_{ion}, κ) from the two Köhler theory models. The s_c values for NaHA determined from the ρ_{ion} and κ-Köhler theory models were in excellent agreement, 0.33 and 0.32%, respectively, when calculated using σ_{H_2O}. Additionally, s_c values for NaHA calculated using σ_{HULIS} agreed very well and were found to be 0.19 and 0.18% for the ρ_{ion} and κ-Köhler theory models, respectively. Using σ_{H_2O}, the ρ_{ion} and κ-Köhler models gave s_c of 0.60 and 0.57%, respectively, for 100 nm SRFA particles. When the σ_{HULIS} was used, these models gave respective values of 0.35 and 0.33% for 100 nm SRFA particles. The values of s_c reported herein for NaHA and SRFA using σ_{H_2O} are in good agreement with theoretical predictions based on σ_{H_2O} by Petters and Kreidenweis[99] of ca. 0.33 and 0.60%, respectively (our estimate from Figure 3-1 in that work using κ values calculated in this work). Additionally, the calculated s_c values for both NaHA and SRFA are consistent with previously measured s_c values in our laboratory.[30] Previous CCN activation measurements of these materials have shown that 235 nm NaHA and SRFA particles become CCN active at a s_c of 0.15 and 0.20%, respectively. As expected from Köhler theory, s_c values for 100 nm particles, calculated here, are higher. It is clear that the s_c values determined, unlike the ρ_{ion} and κ parameters, from Köhler theory depend on the choice of surface tension used. However, at RH values typical of cloud activation, droplets become dilute quickly. Thus, the surface tension trends toward the surface tension of pure water. Additionally, according to Kokkola et al.,[106] σ_{H_2O} is a better estimate of the surface tension of atmospheric HULIS under conditions of activation.

Thus, s_c values obtained from Köhler theory using σ_{H_2O} may be more accurate than those obtained using σ_{HULIS}.

The values of s_c for 100 nm SRFA and NaHA appear to represent the upper and lower limit, respectively, of s_c of similar size HULIS extracted from atmospheric aerosols. For example, Wex et al.[34] investigated the hygroscopic behavior of HULIS extracted from urban $PM_{2.5}$ and compared the values of s_c derived from the Leipzig Aerosol Cloud Interaction Simulator (LACIS) with modeled values using the ρ_{ion} method determined from hTDMA measurements. For 100 nm HULIS particles, they found the modeled results ($\rho_{ion} = 4.85 \diamond 10^{-3}$ mole/cm^3, $\sigma_{H_2O} = 72.8$ mN/m) to be in very good agreement with the LACIS value, ca. $s_c = 0.43\%$ (our estimate based on Figure 3-3 in Wex et al.[92]). This measured value of s_c for an atmospheric HULIS sample is nominally intermediary between our ρ_{ion} and κ-Köhler values for similar sized NaHA and SRFA using σ_{H_2O}. This result suggests that atmospheric HULIS is more hygroscopic then SRFA and less hygroscopic than NaHA with similar trends for the CCN activity as predicted based on Köhler theory. The greater hygroscopicity of aerosol-extracted HULIS compared to SRFA has also been demonstrated in previous studies[95] that show HULIS aerosol activates at smaller diameters than size-fractionated or bulk SRFA and HULIS particles are more CCN-active than all size fractions of SRFA. This effect may derive in part from the oxidative and photo-oxidative aging of atmospherically-derived HULIS particulate matter,[50, 95] resulting in a higher O:C ratio than similar size fractions of SRFA. The relatively high hygroscopicity of NaHA aerosol relative to both SRFA and HULIS may be derived from it being a sodium salt that readily undergoes dissolution.

3.4.3 Infrared Spectroscopy of NaHA and SRFA Using ATR- and Extinction FTIR.

As described, the vibrational spectra of humic substances by infrared spectroscopy were determined on thin films and aerosol particles, utilizing ATR- and

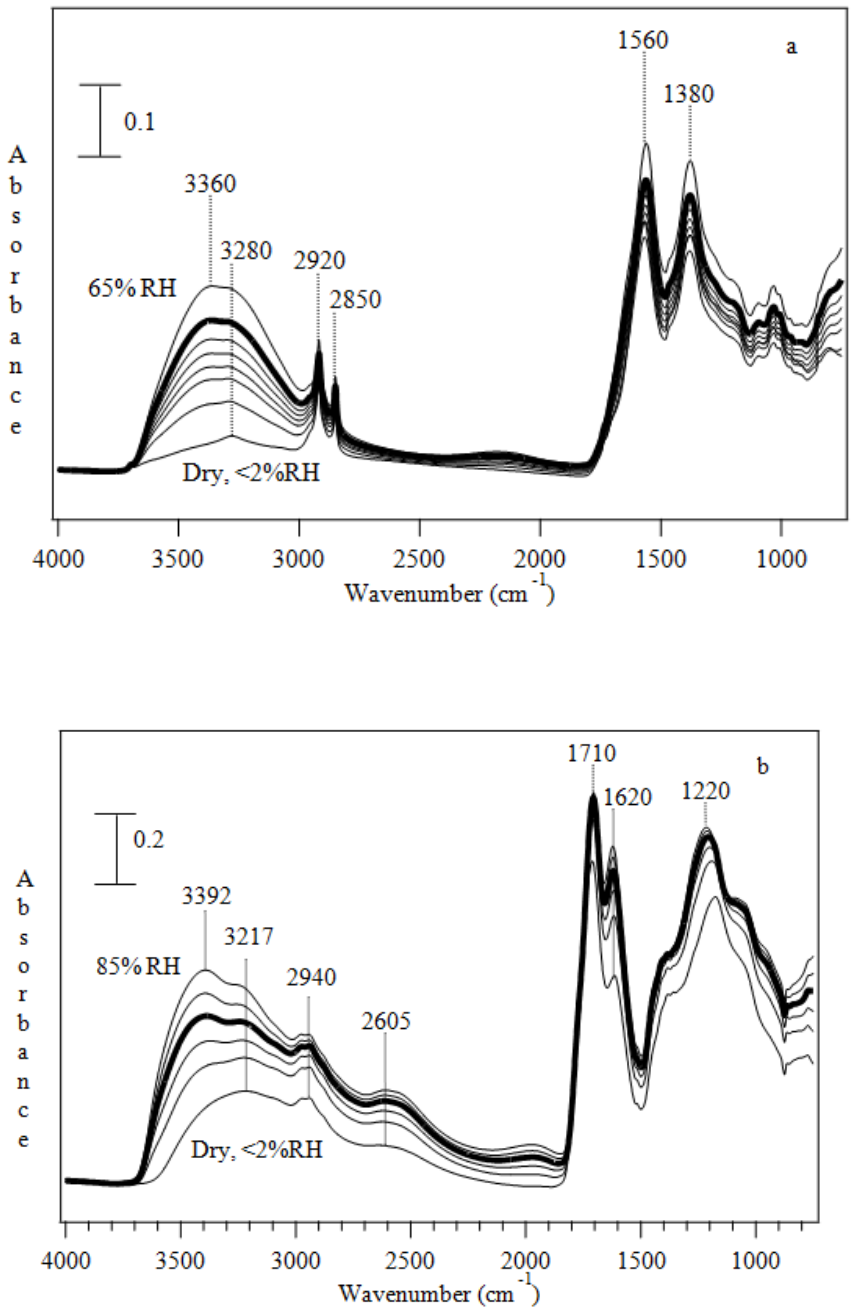

Figure 3-3 ATR-FTIR of thin films of (a) NaHA from RH = 2-75% and (b) SRFA from RH = 2-85%. The bold spectra are at RH values closest to those of the extinction FTIR spectra, 54% and 57%, respectively (see Fig. 3-4).

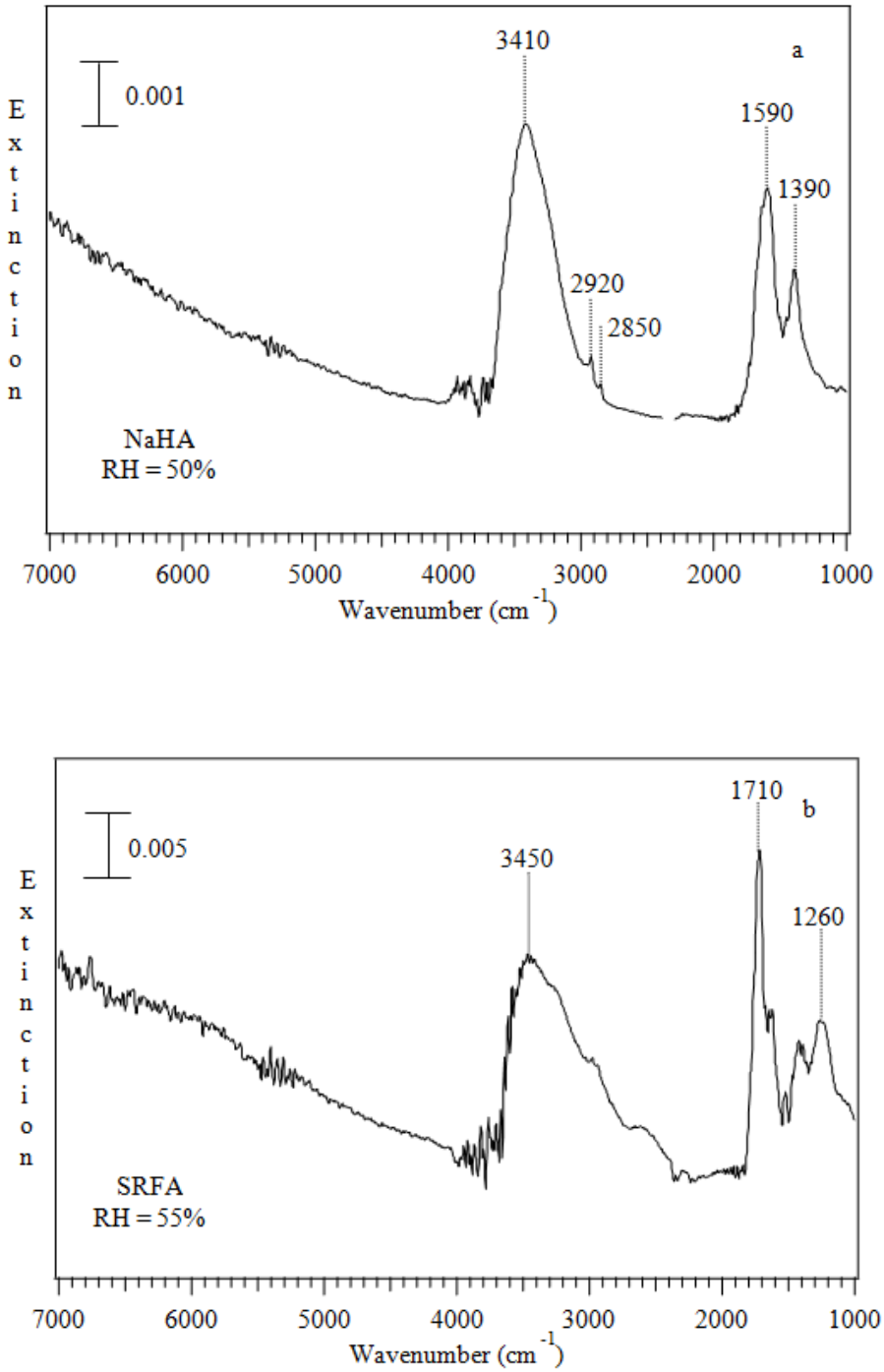

Figure 3-4 Extinction FTIR spectra of a polydispersed distribution of (a) NaHA and (b) SRFA aerosol. These spectra are taken of particles equilibrated with water at the respective RH values. The spectral region between 1000 and 4000 cm^{-1} show absorption bands of NaHA and SRFA and scattered light above 4000 cm^{-1}, as indicated by the increase in intensity with increasing wavenumber out to 7000 cm^{-1}. Gas-phase CO_2 absorptions have been removed from (a).

Table 3-3 Infrared peak assignments.

IR Peak*	Peak assignments
3000-3700 cm^{-1} (br)	O-H stretch from adsorbed water, carboxylic acids, carbohydrates and alcohols, N-H from peptides
2800-3000 cm^{-1}	C-H from aliphatics, aldehydes and aromatics
2300-2700 cm^{-1} (br) (SRFA)	Hydrogen bonded O-H from carboxylic acid
1710 cm^{-1} (SRFA)	C=O stretch from carboxylic acid
1620 cm^{-1} (SRFA)	HOH bending, peptides (-CO-NH-), quinones, olefinic unsaturated groups, carboxylates and C=C in aromatics
1480-1700 cm^{-1} (NaHA)	HOH bending and carboxylates, and C=C in aromatics
1215-1480 cm^{-1} (NaHA)	C-O stretch for carboxylate, OH deformation, C-H deformation
1000-1480 cm^{-1} (br) (SRFA)	C-O stretch and OH deformation of carboxylic acids, C-O stretching of polysaccharides, C-H deformations, and carbohydrates

*br = broad

extinction FTIR spectroscopy, respectively. In general, the multifunctional nature of the humic (Figures 3-3a and 3-4a) and fulvic (Figures 3-3b and 3-4b) materials is evident in the infrared spectra and assignment of specific infrared peaks is difficult as many of the peaks are broad and encompass a number of different functionalities. Table 3-3 includes assignments for the major infrared absorption bands for both NaHA and SRFA.[101, 107-110] The emphasis of the following discussion will highlight differences in functional groups that lend to the different hygroscopic behaviors between SRFA and NaHA.

Figure 3-3a shows the ATR-FTIR absorption spectra of NaHA collected as a function of RH from 2 to 75% RH and is in agreement with infrared spectra previously published in the literature.[101] Although only the adsorption spectra are shown in Figure 3-3, both adsorption and desorption was measured and hysteresis was not observed in the ATR-FTIR measurements. The dry NaHA spectrum, collected at less than 2% RH, shows broad absorption features below 2000 cm^{-1}, characteristic of material that is composed of a many multifunctional aliphatic and conjugated structures. The humic acid in this work is in the form of a sodium salt (i.e. NaHA), and thus the spectra show very strong absorption bands from the asymmetric and symmetric stretching of the carboxylate –C=O moiety at 1560 and 1380 cm^{-1}, respectively. Conversely, little evidence of protonated carboxylic acid groups is observed with weak shoulders from 1700 to 1730 cm^{-1} arising from the –C=O stretch of the acid. This is supported by the FTIR extinction spectrum of NaHA (Figure 3-4a), that shows the carboxylate –C=O asymmetric and symmetric bands centered at 1590 and 1390 cm^{-1}, respectively.

The most striking feature of the ATR-FTIR spectrum of NaHA (Figure 3-3a) is the pronounced increase in the broad band centered at ca. 3300-3400 cm^{-1} with increasing RH. While absorption in the region from 3000-3700 cm^{-1} is typical of O-H stretching from carboxylic acids, alcohols, and phenols,[50, 101] the pronounced increase of the broad band centered at ca. 3300-3400 cm^{-1} with increasing RH is primarily due to the stretching vibrations of absorbed water,[111] rather than the O-H stretching vibrations of carboxylic

acid dimers that are usually centered near 3000 cm^{-1}.[112] As shown in Figure 3-4a, the band arising from the O-H stretching vibration of water is also evident in the extinction FTIR spectrum of NaHA centered at 3410 cm^{-1} at RH = 50%. The O-H stretching vibration of aqueous-phase water[111] is broad and similar in breadth and width of the bands observed in the spectra shown in Figure 3-3 and Figure 3-4 providing evidence for liquid like water not structured or crystalline water.

Figure 3-3b and 3-4b, respectively, show the ATR and extinction FTIR spectra of SRFA collected as a function of RH and are in agreement with previously published spectra.[113-114] The SRFA spectra contain many of the spectral features observed in the NaHA spectra. However, the main difference is the strong absorbance peaks from the presence of protonated carboxylic acid groups, at 2605, 1710 and 1220 cm^{-1}, arising from the O-H, C=O and C-O stretches of carboxylic acid, respectively. For SRFA, unlike NaHA, the broad band arising from the O-H stretch is pronounced even at low RH, arising from the carboxylic acid groups of the former analyte, and in a similar manner to NaHA, this band blue shifts with increasing RH due to the incorporation of water and is centered near 3400 cm^{-1}. Similarly to NaHA, the O–H stretching mode is consistent with aqueous-phase water.

3.5 Summary

The water uptake of two environmentally relevant humic substances, NaHA and SRFA, has been investigated using hTDMA. Hygroscopic growth factors, $g(RH)$, were in good agreement with published data on similar size particles of the same composition.[28, 101-102, 104] Hygroscopic growth data was used to calculate the ionic density, ρ_{ion}, using the surface tension of water and aqueous HULIS. This recently developed parameterization scheme (i.e. the ρ_{ion}-Köhler theory)[92] appears advantageous for modeling the water vapor pressure over an aqueous droplet containing HULIS and humic substances because the unknown physical properties of these substances (i.e. φ, υ, ρ_s, M_s)

are combined into a single parameter, ρ_{ion}. This parameter was incorporated into the Köhler equation to determine s_c of NaHA and SRFA, reported in Table 3-2. The hygroscopic growth data was also used to calculate the hygroscopicity parameter, κ, using another single-parameter representation of Köhler theory (i.e. κ-Köhler theory).[99-100] κ-Köhler theory was then used to determine the critical properties of NaHA and SRFA and the results were in excellent agreement with the results determined from ρ_{ion}-Köhler theory. The calculated s_c values were in good agreement with previously published results.[99] Moreover, these results suggest that NaHA and SRFA are respectively more and less hygroscopic than similar size aerosol-extracted HULIS.[92, 111]

ATR and extinction FTIR absorption measurements of thin films and aerosol particles, respectively, of NaHA and SRFA support the hygroscopic properties measured by hTDMA. Both NaHA and SRFA showed pronounced increase in the broad absorption band centered ca. 3400 cm^{-1} with increasing RH. This band arises to a large extent from the O-H stretching mode of water,[111] and in the case of the acid, SRFA, there is an additional contribution from the O-H stretch of carboxylic acid groups. Qualitatively, the increase in the intensity of this band was very pronounced with the sodium salt, NaHA, and illustrates why the hygroscopicity of NaHA is greater than SRFA and HULIS, namely through the strong Raoult effect conferred by the salt upon dissolution.

This material is based on work supported by the National Science Foundation under grants CHE503854 and ATM0613124. Any opinions, findings and conclusions or recommendations expressed in this material are those of the authors and do not reflect the views of the National Science Foundation. This work has been published in Hatch, C. D.; Gierlus, K. M.; Zahardis, J.; Schuttlefield, J.D.; Grassian, V. H. "Water uptake of humic and fulvic acid: measurements and modeling using single parameter Köhler theory", *Environmental Chemistry*, **2009**, *6*, 380-388.

CHAPTER FOUR
WATER ADSORPTION AND CLOUD CONDENSATION NUCLEI ACTIVITY OF CALCITE AND CALCITE COATED WITH MODEL HUMIC AND FULVIC ACIDS

4.1 Abstract

Studies have shown that organics can alter the water adsorption and cloud condensation nuclei (CCN) activity of common deliquescent species in the Earth's atmosphere. However, very little is known about the effect of organics on water adsorption and CCN activity of insoluble nuclei such as mineral dust aerosol. A large fraction of unidentified organic material in aerosol particles is composed of poly-acidic compounds resembling humic substances. The presence of these Humic-Like Substances (HULIS) can alter the water adsorption and CCN activity of mineral dust aerosol. The CCN activity of model humic and fulvic acids and of mineral dust particles coated with these substances has been measured in the laboratory. It was found that coatings of humic and fulvic acids on calcite particles significantly increases water adsorption compared to uncoated particles. CCN measurements indicate that humic- or fulvic acid-coated calcite particles are more CCN active than uncoated calcite particles. Additionally, thicker coatings of humic or fulvic acids appear to result in more efficient CCN activity. Thus, mineral dust particles coated with high molecular weight organic materials will take up more water and become more efficient CCN in the atmosphere than uncoated mineral dust particles, potentially altering the effect of mineral dust on the Earth's climate. In addition to the experimental results, a newly modified Köhler theory has been used to predict the CCN activity of insoluble, wettable particles based on multilayer water adsorption measurements of calcite.

4.2 Introduction

Humic substances, such as humic and fulvic acids, are broadly defined as macromolecular, multifunctional organics naturally produced by microbial oxidative degradation of plant and animal matter.[41] A heterogeneous mixture of functional groups, including aliphatic, aromatic, hydroxyl, carbonyl and carboxylic acid groups are present in these macromolecular structures. Recent studies have found that humic-like substances (HULIS) comprise a significant portion of atmospheric organic aerosol[50] which is known to play an important role in cloud nucleation.[46] One recent field study has shown that approximately 60% of water soluble organic carbon (WSOC) from rural atmospheric aerosol is composed of HULIS.[60] Thus, these substances can play an important role in the delicate balance of our climate by modifying optical and water adsorption properties of atmospheric aerosol, directly and indirectly influencing the Earth's climate, respectively.

Previous studies have shown that the infrared spectrum of fulvic acid from terrestrial systems closely resembles that of atmospheric HULIS and WSOC-derived HULIS from dust samples.[41, 45] However, HULIS is different from aquatic and soil derived humic substances in many ways.[45, 50] Upon comparing WSOC-derived HULIS from fine aerosol particles to fulvic acid, HULIS tends to have higher surface activity, less aromatic functionalities, weaker acidity and smaller molecular sizes than the fulvic acids[50, 59] These results indicate that HULIS may have sources other than terrestrial soil and aquatic matter.[50]

Although probably not the dominant source of HULIS in the atmosphere, humic substances can be emitted by primary sources, such as with wind-blown marine,[43-44] mineral[19, 45] and biomass burning[46-47] particles and thus become entrained in the atmosphere, often as an internal mixture with other components such as mineral dust. For example, 6-11% of the total organic carbon extracted from urban dust samples can be attributed to humic and fulvic acids.[45] However, observed HULIS concentrations cannot

be fully explained by primary sources. Recent studies have shown that secondary sources must exist through processes such as condensation, oxidation, reaction and polymerization in the atmosphere.[58, 101, 115] For example, formation of HULIS can occur through photo-oxidation of organic precursors.[55-56] Additionally, HULIS may also be a product of sulfuric acid-catalyzed oxidation of isoprene or α-pinene.[58]

As a result of studies conducted in response to the uncertainty in climate effects of atmospheric aerosols,[2] there is currently have a good understanding of the hygroscopic growth and cloud droplet formation of single-component inorganic aerosol,[87, 116] and organic[14, 117-120] aerosols. Additionally, field, laboratory and theoretical studies have shown that multi-component aerosols can alter hygroscopic growth[22, 121-124] and cloud condensation nuclei (CCN)[118, 125-126] properties relative to the single-component particles. Furthermore, recent studies have investigated water adsorption and hygroscopic growth of humic substances and atmospheric HULIS using Humidified Tandem Differential Mobility Analyzers (HTDMA),[93, 98, 101-103] gravimetric[28] and optical[94, 127] measurements of single components or of internal mixtures with soluble species, such as ammonium sulfate. These studies show that humic substances can alter properties of the inorganic component.

Mineral aerosol, like other insoluble species,[14-15] are known to be less active CCN than common soluble salts, such as ammonium sulfate.[16] However, atmospheric processing resulting in the presence of soluble nitrate or sulfate coatings on clay and carbonate particles can enhance the CCN activity.[15] Since large molecular weight organics are known to be associated with dust in the atmosphere,[19-21] and the presence of organic films can impact the hygroscopic properties of aerosol particles,[13, 22] organic or humic coatings on mineral aerosol could alter the climate effects of the dust particles. However, the study of water adsorption on these mixtures over the full dynamic range of water uptake from hygroscopic growth to CCN activity has yet to be explored.

The water adsorption and CCN activity of calcite ($CaCO_3$) has been measured with and without humic coatings. Calcite was used as a model dust component because a previous study found carboxylic acids and carbonyl groups associated with $CaCO_3$ particles by mapping organic coatings on individual aerosol particles.[20] The CCN activity of pure humic and fulvic acids has also been measured. As atmospheric HULIS may have different properties depending on the source, humic acid was used as a surrogate for HULIS because it can be co-emitted with mineral aerosol. Fulvic acid is more representative of lower molecular weight HULIS formed from secondary processes. However, atmospheric HULIS has previously been found to be more hygroscopic than terrestrial fulvic acids.[93] Thus, water adsorption on the humic and fulvic acids reported here is expected to represent a lower limit to the behavior of HULIS. To explore the effectiveness of humic coatings on insoluble particles, the CCN activity of coated polystyrene latex spheres (PSLs) has been measured. Finally, since many studies have shown that traditional Köhler theory does not work well for insoluble particles,[14] new theoretical methods are emerging. A modified Köhler theory based on particle growth by multilayer water adsorption on insoluble particles is tested using experimental results for water adsorption on $CaCO_3$.[79]

4.3 Experimental Methods and Data Analysis

4.3.1 Materials

Commercial humic substances were used without further processing. Humic acid sodium salt (NaHA) was obtained from Sigma-Aldrich (Product #16752) and Suwannee River fulvic acid (SRFA) standard was obtained from the International Humic Substances Society (Product #15101F). These humic substances have been used in recent studies as surrogates for atmospheric HULIS.[28, 96, 103, 128] Model insoluble particles, including $CaCO_3$ (OMYA) powder and PSLs (Polysciences, Inc., 202(±10) nm), were used as received. The Brunauer, Emmett and Teller (BET) specific surface area of the $CaCO_3$,

10.1(±0.1) m^2 g^{-1}, was determined using a Quantachrome Nova 1200 surface area analyzer with nitrogen as the adsorbate.

4.3.2 Quartz Crystal Microbalance

Gravimetric measurements were collected to quantify bulk water adsorption on $CaCO_3$ and mixtures of $CaCO_3$ with NaHA or SRFA using a 5 MHz quartz crystal microbalance flow cell (QCM 200, Stanford Research Systems) previously described in the literature.[88] The QCM measures a change in frequency that is used to determine the mass of water adsorbed to the sample. The relationship between the change in frequency, Δf (Hz), and the change in mass, Δm (μg/cm^2), is given by the Sauerbrey equation shown below .[89]

$$\Delta f = -C_f \times \Delta m \tag{4-1}$$

where C_f is the sensitivity factor, 56.6 Hz $\mu g^{-1} cm^{-2}$, specific to the 5 MHz AT-cut quartz crystal used in this study.

The samples were spray-deposited on the quartz crystal from an aqueous suspension of the sample. The suspension consisted of 2 g $CaCO_3$ in 20 mL of Optima water (Fischer Scientific) or a 0.01 wt% NaHA or SRFA solution. The deposited sample was dried with dry air, less than 5% RH, overnight. Adsorbed water was quantified by monitoring the change in frequency upon increasing the RH through the flow cell. Further details of the experimental procedure have been discussed previously.[88] The RH, monitored with a RH sensor (Honeywell, HIH-3602-L), was regulated by changing the ratio of wet/dry air. Each sample was allowed to equilibrate with water vapor for 30 minutes at each RH studied. The QCM quantifies adsorbed water in terms of a mass ratio of adsorbed water to the dry sample mass. The fractional monolayer coverage, assuming

one monolayer is $1x10^{15}$ molec cm^{-2}, was estimated using the measured BET surface area of $CaCO_3$.

4.3.3 Size Distribution and CCN Activation

Cloud droplet activation measurements and size distributions were obtained using a Multi-Analysis Aerosol flow Reaction System (MAARS) developed at the University of Iowa and previously described in the literature.[81, 129] The important experimental components of MAARS in the present study consist of a constant output atomizer (TSI, Inc. Model 3076), two diffusion dryers (TSI Inc., Model 3062), a Differential Mobility Analyzer (DMA_1; TSI, Inc. Model 3080) used for size selection, flow tubes, a scanning mobility particle sizer (SMPS; TSI, Inc. Model 3936) in which a second DMA (DMA_2) is coupled to a condensation particle counter (CPC, TSI, Inc. Model 3025A) and a continuous flow stream-wise thermal-gradient cloud condensation nuclei counter (Droplet Measurement Technologies, Model CCN-2)[86] for the measurement of CCN activity of monodisperse particles.

Experiments began with aerosol generation using an atomizer operating at 3.0 Standard Liters per Minute (SLM) with dry, particle-free air producing a polydisperse distribution of aerosol particles. The pure NaHA and SRFA were atomized from a 1.0 wt% solution in water while $CaCO_3$ and PSLs were atomized from a suspension of the insoluble particles in water. Direct atomization of a mixture of the insoluble $CaCO_3$ or PSL particles in a solution, 0.01 or 0.05 wt%, of the soluble NaHA or SRFA substances produced internally mixed particles, as shown in Figure 4-1. To reduce the CCN contribution from externally mixed particles, the concentration of NaHA and SRFA solutions was chosen so that overlap of the PSL or $CaCO_3$ size distributions with that of the soluble humic and fulvic acid is minimized while the concentration of the insoluble particles is maximized. This method has been used previously to generate internally mixed dust[80] or organics[122] with soluble salts.

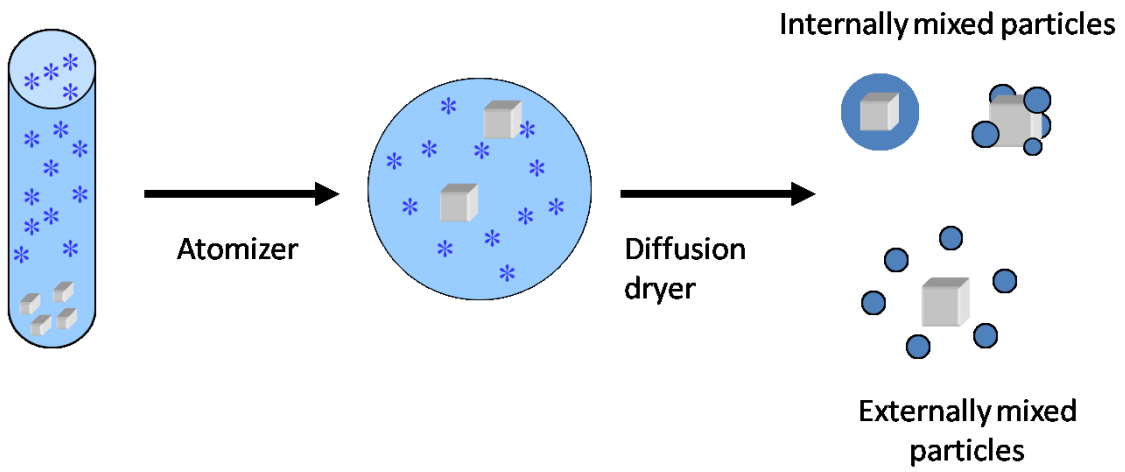

Figure 4-1 Internally mixed particles are generated from a suspension of an insoluble material in an aqueous solution. Droplets containing the insoluble particles are generated by the atomizer. Diffusion dryers are used to remove water vapor leaving the soluble material coating or internally mixed with the insoluble material. External mixtures are formed, as well.

Upon atomization, the polydisperse aerosol was directed through two diffusion dryers that dry the aerosol to less than 12% RH. The dry particle stream then either bypassed or was directed into DMA_1 to produce polydisperse or monodisperse aerosol, respectively. The dry particles were directed into flow tubes maintained at <1% RH. Upon exiting the flow tubes, size distributions of the dry particles were measured by the SMPS based on the electrostatic mobility diameter by scanning for 210 seconds with flow rates of 2.0 (sheath) and 0.2 (aerosol) SLM. Mean diameters and distribution widths of the polydisperse aerosol obtained by fitting lognormal distributions to the measured size distributions and averaging over multiple scans are reported in Table 4-1 for each aerosol studied. Errors in the reported lognormal distribution parameters represent uncertainty from the reproducibility of the SMPS data. The accuracy of the average diameter was determined from the percent difference between SMPS measurements of

several PSL particles having a broad range of diameters and the manufacturer-specified PSL diameter and was found to be ±4%.

For CCN measurements, monodisperse particles were generated by size-selecting using DMA_1 prior to introducing particles into the flow tubes. The sizing accuracy of DMA_1 was determined by measuring the size-selected diameter by DMA_2 and was found to vary by ~1 nm. To measure the CCN activity, the monodisperse aerosol exiting the flow tubes was split and simultaneously traveled the same distance to either the CPC or CCN counter. The CCN active aerosol fraction was obtained by ratioing the number of particles that act as CCN (#CCN) measured by the CCN counter at a given percent supersaturation, %s, to the total number of particles (#CN) measured by the CPC. The CCN counter was calibrated based on ammonium sulfate (Fisher Scientific, ACS) CCN activity.[87] Typical particle concentrations were maintained between $1x10^3$ and $4x10^3$ molecules/cm^3 for all CCN measurements reported here.

In theory, the plateau of the fraction of CCN active particles as a function of %s should occur at a #CCN/#CN ratio of unity, indicating that 100% of the condensation nuclei have become active. In practice, the plateau occurs at an activation ratio between 0.86 and 1.2. Similar results are commonly reported in the literature[117, 119] and may be due to counting inefficiencies of the CPC or CCN instruments. However, as indicated by the flatness of the plateau at large %S values, full activation of the sampled aerosol is observed. To correct for this, the experimental #CCN/#CN ratios were normalized by multiplying by the reciprocal of the average value of the fully activated fraction.

4.3.4 Calculation of the Hygroscopicity Parameter

A theoretical framework called κ-Köhler theory has recently been developed relating the dry aerosol diameter and the CCN activity using a single hygroscopicity parameter, κ.[99] Kappa describes the relative hygroscopicity of various components found in the atmosphere such that for common CCN active soluble salts, κ ranges from

0.5 to 1.4 and approaches a value of zero for non-hygroscopic aerosol. The saturation ratio, *S*, over an aqueous solution droplet can be calculated from *κ*-Köhler theory using equation (4-2)[99]:

$$S = \left(\frac{D_p^3 - D_o^3}{D_p^3 - D_o^3(1-\kappa)} \right) \exp\left(\frac{4M_w\sigma_s}{RT\rho_w D_p} \right) \tag{4-2}$$

where D_p and D_d are the aqueous droplet diameter and the dry diameter, respectively, σ_s is the surface tension of the solution/air interface, R is the ideal gas constant, T is the temperature, and M_w and ρ_w are the molecular weight and density of water, respectively. The critical saturation (related to the critical supersaturation by $S_c = s_c + 1$) is determined by finding maximum of the *κ*-Köhler curve in equation (4-2). By solving for the critical diameter (D_p at S_c) an equation for *κ*, can be derived. Using this equation (4-3) the measured CCN activity can be used to determine the hygroscopicity parameter.[99]

$$\kappa = \frac{4A^3}{27D_d^3 \ln^2 S_c} \tag{4-3}$$

where

$$A = \frac{4\sigma_{sol}M_w}{RT\rho_w} \tag{4-4}$$

The surface tension of pure water, 0.072 J/m^2,[130] and a temperature of 298.15 K were assumed to calculate *κ* values for all aerosol particles studied based on the experimental critical percent saturation, %s_c, defined as the %s at which 50% of the

monodisperse aerosol is activated. Despite the fact that humic substances are surface active and the surface tension may be suppressed relative to that of pure water leading to an overestimation of the κ value, Petters and Kreidenweis suggest that the use of the surface tension of water is adequate for describing hygroscopic behavior of both single-component and mixed aerosol particles as long as the assumption is consistent between the measured κ value and the use of experimental κ values to predict $\%s_c$.

Based on the κ values for the individual components, it is shown that the κ values for the multi-component systems can be estimated according to a simple mixing rule:

$$\kappa = \sum_i \varepsilon_i \kappa_i \tag{4-5}$$

where ε_i is the volume fraction of the individual components.

4.4 Results and Discussion

4.4.1 Water Adsorption on $CaCO_3$ and Mixtures of $CaCO_3$ with Model HULIS

Gravimetric measurements indicate continuous water adsorption on $CaCO_3$ and $CaCO_3$ coated with NaHA or SRFA over the range of RH values studied. Figure 4-2 shows the adsorbed water content measured by QCM in terms of the mass ratio of adsorbed water to the dry sample mass. The error represents variability in multiple measurements collected at the same RH. As shown in Figure 4-2, above 40% RH, the water content of the $CaCO_3$ sample mixed with NaHA increases significantly compared to the sample in which only $CaCO_3$ is present. This result is in agreement with a previous study of water adsorption on montmorillonite clay in the presence of short-chain organic acids in which enhanced water adsorption above 40% RH was observed.[131] Figure 4-2 shows that the $CaCO_3$/SRFA mixture has more adsorbed water below 40% RH compared

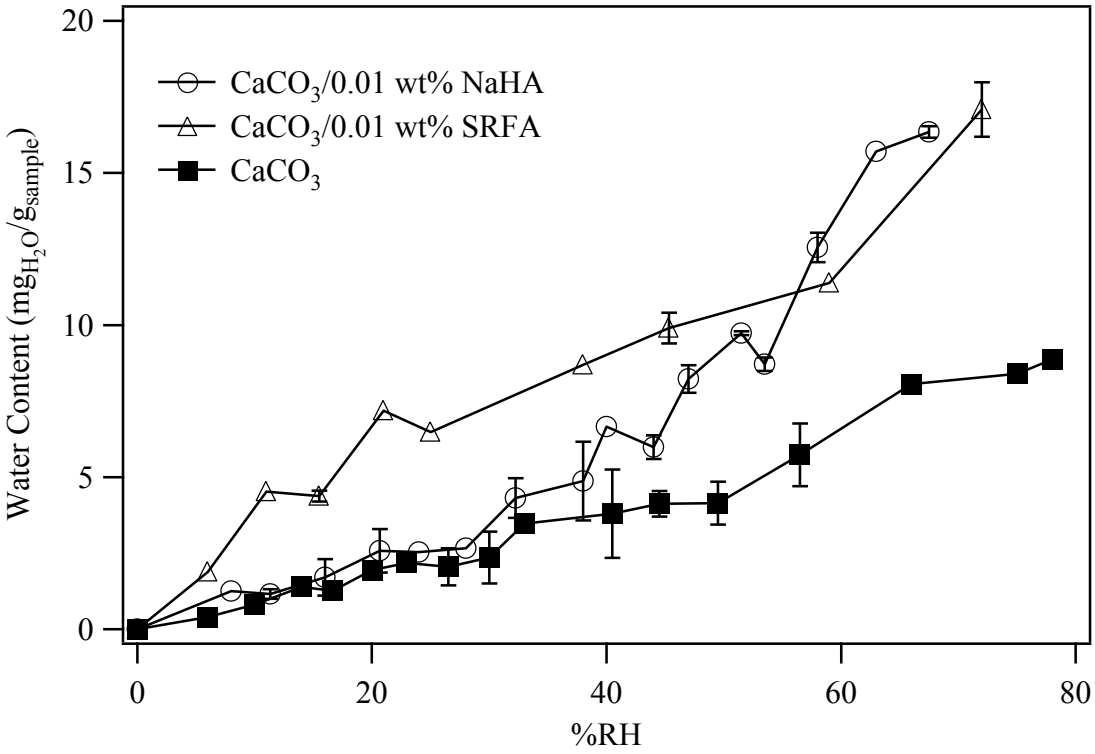

Figure 4-2 Water content (mg_{H_2O}/g_{sample}) on $CaCO_3$ and on a mixture of $CaCO_3$ with NaHA or SRFA as measured by the QCM as a function of %RH. The lines are added to guide the eye.

to the $CaCO_3$/NaHA mixture and $CaCO_3$ alone. This is possibly due to the more acidic nature of SRFA compared to NaHA. However, above 40% RH, the $CaCO_3$/SRFA mixture takes up a comparable amount of water to the $CaCO_3$/NaHA sample. Atapproximately 70% RH, the water content is enhanced by a factor of two for samples in which $CaCO_3$ is mixed with NaHA or SRFA relative to the $CaCO_3$ only sample.

Using the BET surface area of $CaCO_3$, the mass ratio can be converted to the fractional monolayer coverage. The coverage of water on $CaCO_3$ at 78% RH was estimated to be approximately three layers, in agreement with previous studies.[132-133] Assuming the same surface area can be used for the mixed samples, It is estimated that six and sixteen layers of water adsorb to the $CaCO_3$/NaHA and $CaCO_3$/SRFA mixtures, respectively, at the highest RH values studied. Enhanced water adsorption at high humidities compared to the $CaCO_3$ alone suggests that dust mixed with humic substances is more CCN active than dust with no coating. In the following sections, the effectiveness of generating humic coatings on insoluble aerosols are discussed and the the water adsorption isotherm for $CaCO_3$ is used to test a modified Köhler theory for predicting CCN activity of wettable, insoluble particles.

4.4.2 TEM Images of Aerosols Studied

Polystyrene latex spheres were used as model systems for insoluble mineral aerosol to better understand how humic substances coat and activate dust particles as CCN. Transmission electron microscope (TEM: JEOL JEM-1230) images, shown in Figure 4-3, were obtained by exposing carbon-coated copper TEM grids (Ted Pella, Inc., Type-B, 300 mesh) to the flow of size-selected aerosol. Figure 4-3a shows the TEM image of a 235 nm NaHA aerosol generated by atomizing a solution of 1.0 wt% NaHA. Figure 4-3b shows a typical 235 nm particle atomized from a suspension of the PSL particles in 0.01 wt% NaHA. As observed, both particles are spherical in shape. Due to the different densities of the materials combining to form the internally mixed particle, it

is possible to distinguish the humic material from the PSL. As the humic material is denser than the PSL it appears darker in the images. One would expect the upper left corner of the particle shown in Figure 4-3b to be darker than the rest of the particle if this was a PSL particle containing a lump of humic material on the edge of the PSL. However, this is not the case. The coated insoluble PSL core, which has a lower density than the humic material, is observed in Figure 4-3b as the lighter, recessed edge in the upper left corner of the internally mixed particle. The coating appears as the darker substance surrounding the PSL particle due to higher density of the humic material relative to the PSL. Finally, Figure 4-3c shows the TEM image of a 235 nm $CaCO_3$ particle. As shown in the TEM image, the $CaCO_3$ is more irregularly shaped than the spherical PSL particles.

4.4.3 Size Distributions of Aerosols Studied

Figure 4-4a shows the lognormal distribution fits to the average size distributions from multiple SMPS scans of the PSL aerosol generated from a suspension of the PSL particles in water, 0.01 wt% and 0.05 wt% NaHA. The mean mobility diameter (width) increases from 228(0.08), to 235(0.10) to 244(0.13) nm for the PSL and the NaHA-coated PSL aerosol generated from 0.01 and 0.05 wt% NaHA solutions, respectively. Thus, the mean diameter shifts to larger diameters with a more polydisperse distribution as the NaHA solution becomes more concentrated and the NaHA coating thickness increases. The change in mean diameters upon increasing the NaHA coating thickness was used to determine the percent mass fraction of NaHA coating on the PSL particles.

The mass fraction of NaHA on the coated PSL spheres can be estimated from the increase in the mean diameter of the NaHA-coated PSL aerosol relative to the uncoated PSL particle diameter. As shown in Figure 4-3b, the NaHA-coated PSL aerosol is nearly spherical and thus the NaHA forms a near uniform coating on the PSL core. The difference between mean diameters of the NaHA-coated PSL aerosol and the pure PSL

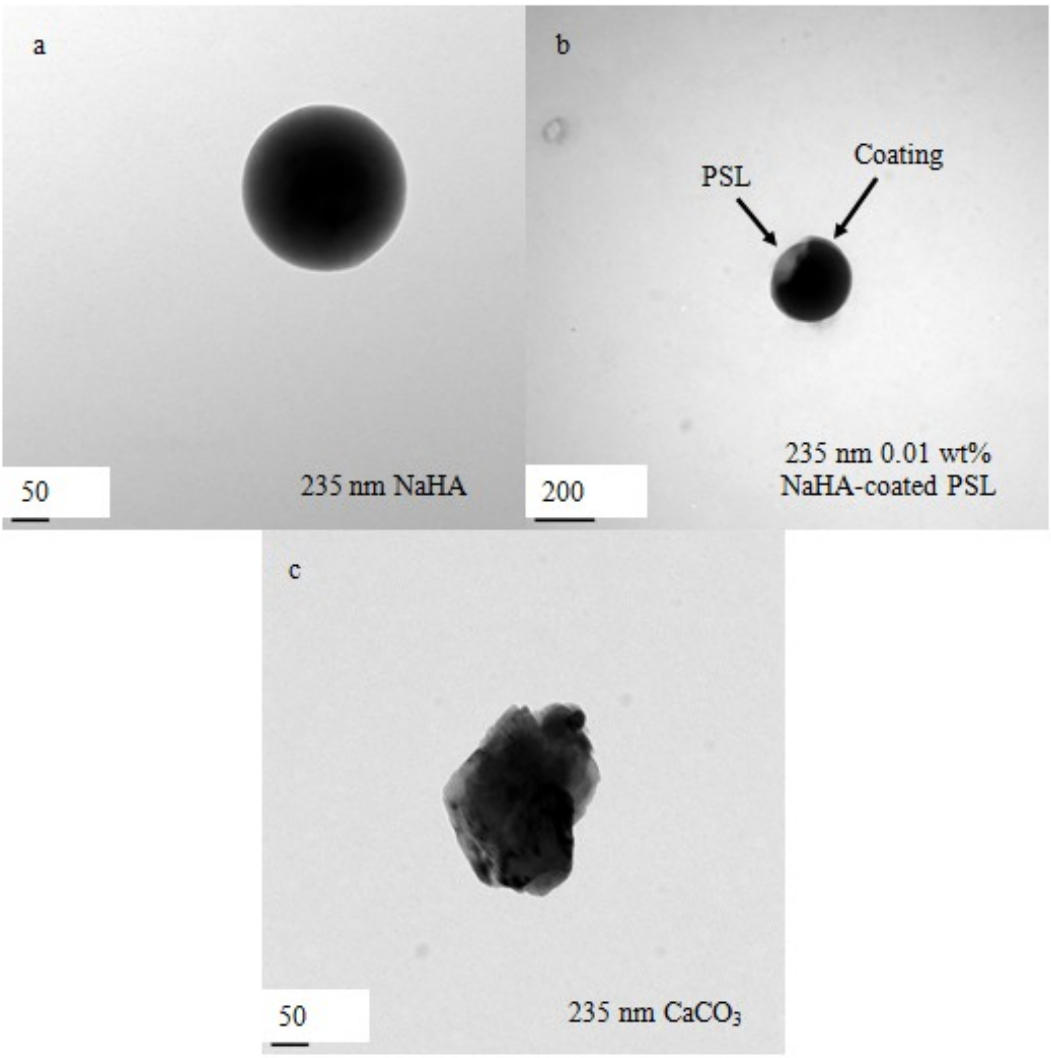

Figure 4-3 TEM images of 235 nm size-selected aerosol particles generated from (a) 1.0 wt% NaHA, (b) a suspension of PSL particles in 0.01 wt% NaHA solution and (c) a suspension of $CaCO_3$ in water and collected on a carbon-coated copper TEM grid.

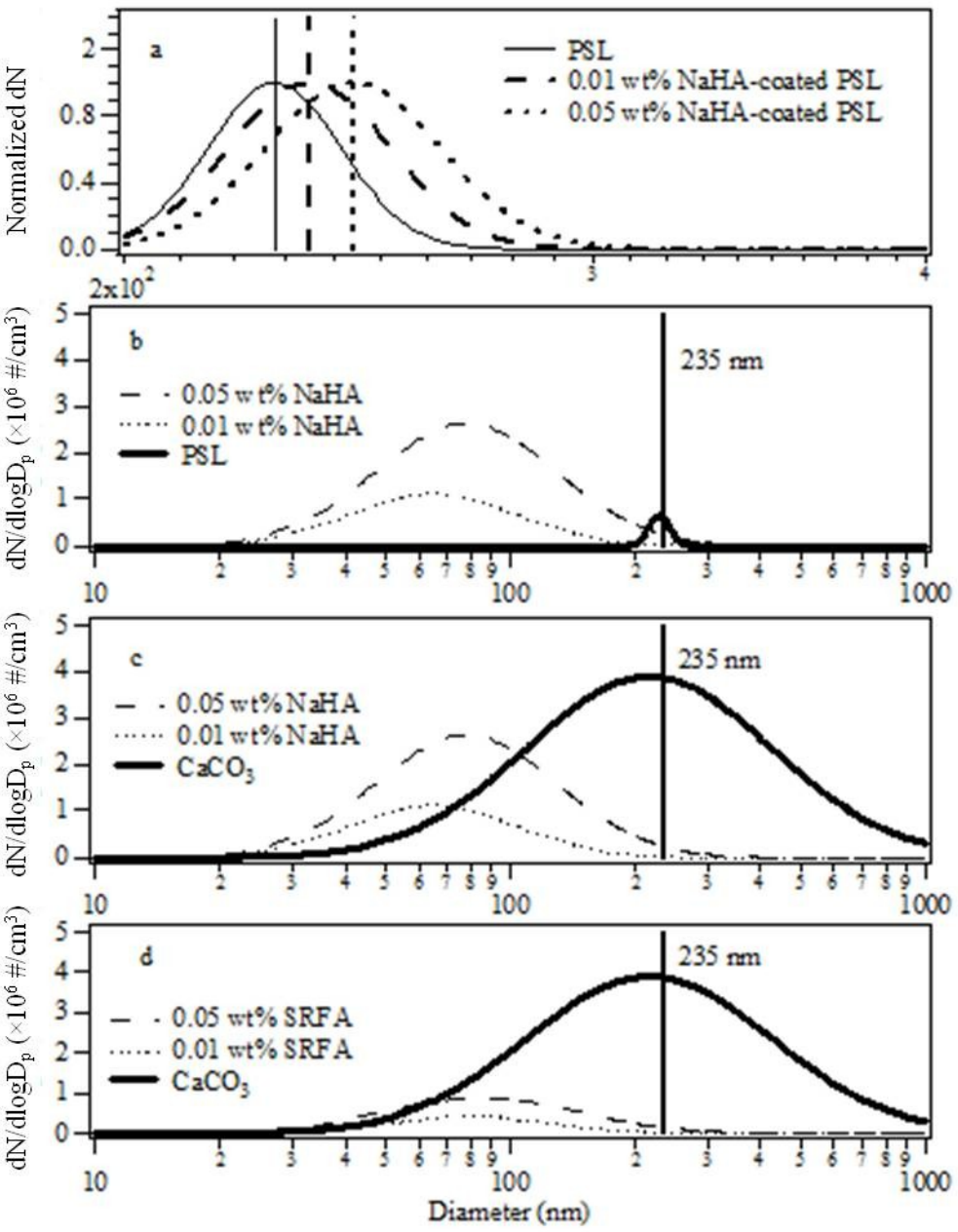

Figure 4-4 Lognormal distribution fits to the average full size distributions measured by SMPS of (a) PSL aerosol and the NaHA-coated PSL aerosol generated from a suspension of the PSL particles in water and in solutions, respectively, of either 0.01 or 0.05 wt% NaHA, aerosol generated from 0.01 and 0.05 wt% NaHA solutions compared to the size distributions of (b) PSL and (c) $CaCO_3$ aerosol, and (d) aerosol generated by atomizing 0.01 and 0.05 wt% SRFA solutions compared to the size distribution of $CaCO_3$ aerosol. The vertical lines in (b), (c) and (d) represent the size-selected particle diameter for all CCN measurements reported here.

aerosol gives an estimate of the thickness of the NaHA coating. The average diameters of the PSL and internally mixed PSL-NaHA particles are determined by averaging the mean diameters obtained by fitting lognormal distributions to multiple size distributions collected by the SMPS shown in Figure 4-4a. The mass of the PSL core (m_{PSL}) is determined from the average PSL diameter, 228(±1) nm, and the known density of PSL particles, 1.05 g/cm^3.[15] The mass of the NaHA coating is determined assuming spherical particles and volume additivity using the following equation:[134]

$$m_{NaHA} = \frac{\rho_{NaHA}\pi}{6}\left(D_p^3 - D_{PSL}^3\right) \tag{4-6}$$

where ρ_{NaHA} is the estimated density of humic acid, assumed to be equivilant to that of SRFA and atmospheric HULIS, ~1.5 g/cm^3,[94] and D_p and D_{PSL} are the dry diameters of internally mixed PSL-NaHA and the PSL core, respectively. Once m_{NaHA} and m_{PSL} are known, the percent mass fraction, $\%f_{NaHA}$ of NaHA in the coated aerosol can be calculated according to the following equation.

$$\%f_{NaHA} = \left(\frac{m_{NaHA}}{m_{NaHA} + m_{PSL}}\right) \times 100 \tag{4-7}$$

The average $\%f_{NaHA}$ is found to be approximately 12% and 24% NaHA in particles generated from a suspension of the PSLs in 0.01 and 0.05 wt% NaHA solutions, respectively. Thus, the particles studied here have slightly more humic or fulvic acid than that measured in urban dust samples, as mentioned previously.[45] However, as shown in Figure 4-3b, although the NaHA coating is nearly uniform over the PSL surface, a small fraction of the PSL particle may not be coated. Thus, the reported

$\%f_{NaHA}$ on the PSL particle may be slightly overestimated and should be regarded as an upper limit.

The percent mass fraction of NaHA, $\%f_{NaHA}$, in a 235 nm dry NaHA-coated $CaCO_3$ particles can be estimated based on the size-selected size distribution of the $CaCO_3$ core using Eqs. (4-6) and (4-7) assuming spherical particles and exchanging the core diameter of the PSL particles, D_{PSL}, with the core diameter of the $CaCO_3$, D_{CaCO_3}, aerosol. However, as shown in Figure 4-2c, $CaCO_3$ particles are non-spherical in shape and thus organic coatings may not be uniform, resulting in some uncertainty in this calculation. Figure 4-5a shows the $\%f_{NaHA}$ calculated using a particle diameter, D_p, of 235 nm as a function of the $CaCO_3$ core diameter obtained from the size-selected size distribution of the single-component $CaCO_3$ aerosol. As shown, the $\%f_{NaHA}$ in the NaHA-coated $CaCO_3$ particles increases as the $CaCO_3$ core diameter decreases. Figure 4-5b shows the frequency of occurrence for each of the calculated $\%f_{NaHA}$ values based on the normalized, size-selected size distribution of the single-component $CaCO_3$ aerosol. From Figure 4-5b, it is shown that most of the 235 nm NaHA-coated $CaCO_3$ particles have less than 10% NaHA by mass. However, this calculation is appropriate only if the NaHA coating crystallizes on the insoluble core and no adsorbed water is present. Although the aerosol is dried to less than 1% RH within the flow tubes, some adsorbed water may remain after the diffusion driers, which dry the aerosol to less than 12% RH, and thus the $\%f_{NaHA}$ shown in Figure 4-5 should be regarded as an upper limit.

In the case that the internally mixed aerosol remains in the aqueous phase produced by the atomizer without drying, the density of NaHA in Eq. (4-6) can be replaced with the concentration, c_{NaHA}, of the NaHA solutions, 0.01 and 0.05 wt% NaHA.[15, 134] Thus, the $\%f_{NaHA}$ in the NaHA-coated $CaCO_3$ droplets can be determined.

In this way it is possible to account for both the variability in the $CaCO_3$ core diameter in addition to the volume of the droplet, which also varies according to the size distribution of the aerosol produced by the atomizer, 0.35 μm mean diameter and 1.9

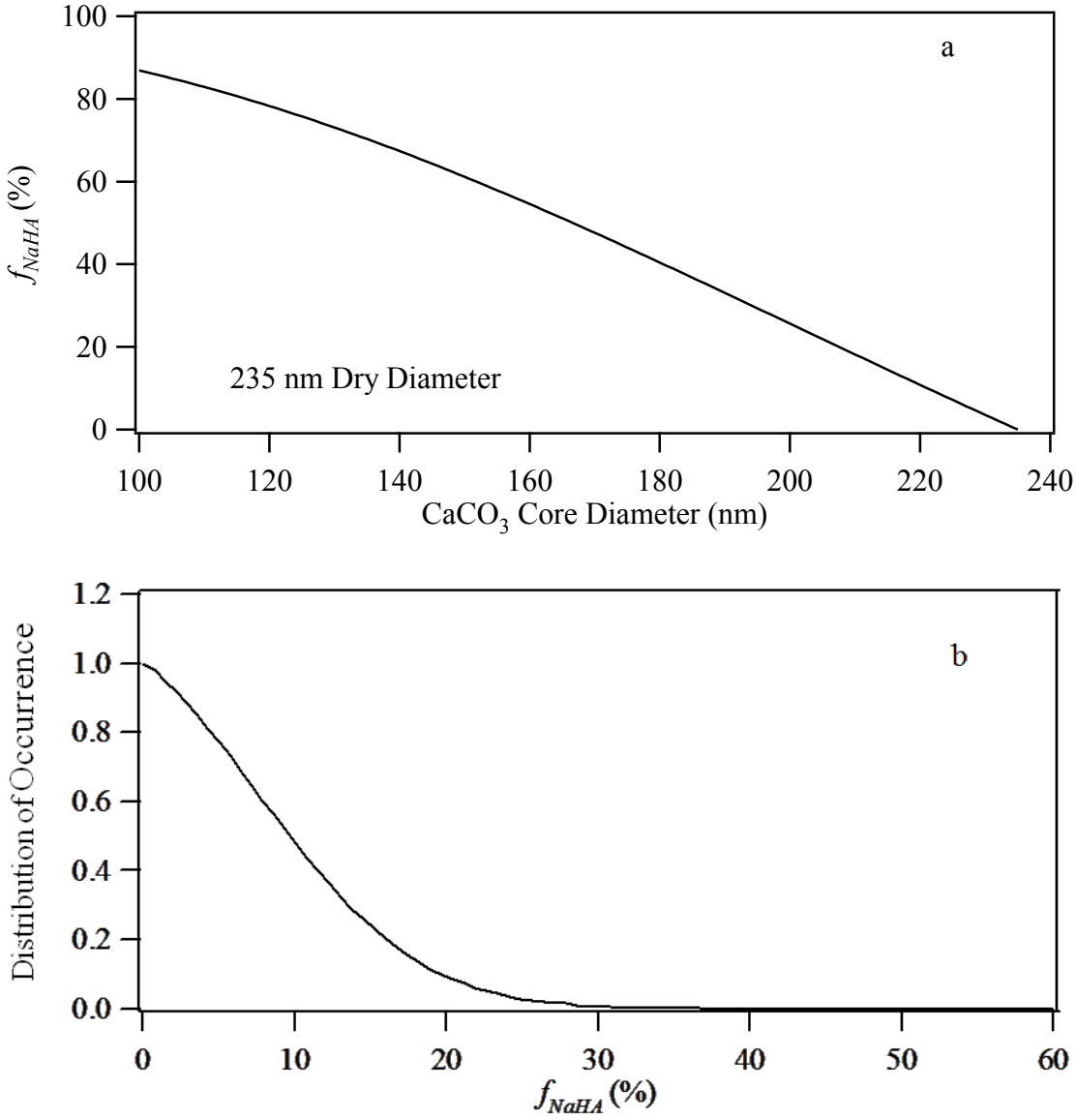

Figure 4-5 Theoretical characterization of the NaHA coating on $CaCO_3$ particles. (a) Percent mass fraction of NaHA in the dry, 235 nm NaHA-coated $CaCO_3$ particles as a function of $CaCO_3$ core diameter. (b) Distribution of occurrence of each $\%f_{NaHA}$ based on D_p = 235 nm and the normalized size distribution of the size-selected, single-component $CaCO_3$ aerosol.

width as stated my manufacturer. The $CaCO_3$ core mass and the mass of the NaHA component can be calculated as follows:[134]

$$m_{CaCO_3} = \rho_{CaCO_3} \frac{\pi}{6} \left(\frac{D_p^3 - \frac{c_{NaHA}}{\rho_{NaHA}} D_{drop}^3}{1 - \frac{c_{NaHA}}{\rho_{NaHA}}} \right) \tag{4-8}$$

$$m_{NaHA} = c_{NaHA} \left(\frac{\pi}{6} D_{drop}^3 - \frac{m_{CaCO_3}}{\rho_{CaCO_3}} \right) \tag{4-9}$$

where D_{drop} is the diameter of the solution droplet generated from the atomizer and ρ_{CaCO_3} is the density of the $CaCO_3$ core, 2.71 g/cm^3. The diameter of the solution droplet for this calculation ranges from the size-selected diameter of 235 nm, D_p, to the full width at half maximum of the aerosol generated from the atomizer, 1700 nm.

Figure 4-6a and b show the calculated core diameter and $\%f_{NaHA}$ as a function of the droplet diameter produced from the atomizer for 0.01 and 0.05 wt% NaHA solutions. As shown, the core diameter decreases as the droplet diameter becomes larger in order to accommodate the increasing volume of solution in the droplets. Additionally, the fraction of NaHA in the droplets is shown to increase depending on the concentration of the NaHA solution from which the droplets are generated. From this calculation, it is estimated that the largest the $\%f_{NaHA}$ associated with the aerosol to be approximately 1% and 7% for aerosol generated from the 0.01 and 0.05 wt% NaHA solutions, respectively. This result is in agreement with the increase in CCN activity when $CaCO_3$ is generated from a suspension of $CaCO_3$ in 0.05 wt% NaHA compared to aerosol generated from the 0.01 wt% NaHA solution. Figure 4-5 shows the distribution of occurrence for the various $\%f_{NaHA}$ values attainable from the atomized aerosol. As shown, the $\%f_{NaHA}$ in the aerosol

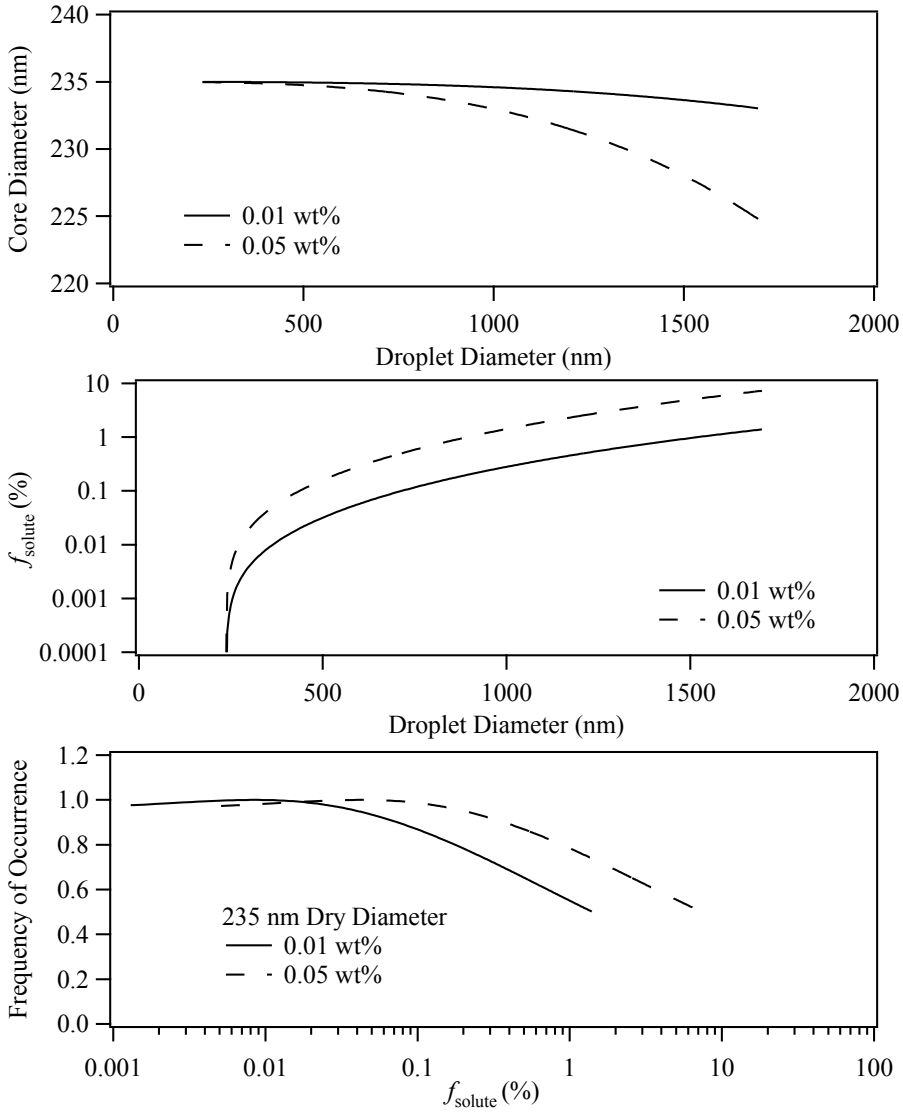

Figure 4-6 Coating of NaHA on $CaCO_3$ based on the diameter of the droplet produced by the atomizer. (a) Calculated core $CaCO_3$ diameter of 235 nm NaHA-coated $CaCO_3$ aerosol generated from 0.01 and 0.05 wt% NaHA solutions as a function of atomizer droplet diameter (D_{drop}). (b) Calculated percent mass fraction of NaHA in 235 nm NaHA-coated $CaCO_3$ aerosol as a function of D_d. (c) Estimate of the frequency of occurrence of 235 nm NaHA-coated $CaCO_3$ aerosol with a given $\%f_{NaHA}$.

is expected to be less than 1% and 7% for the NaHA-coated $CaCO_3$ aerosol generated from 0.01 and 0.05 wt% NaHA solutions, respectively. However, as seen in the figure the most probable value of $\%f_{NaHA}$ will be less than 1% NaHA by mass, which is in good agreement with results obtained using Eqs. (4-6) and (4-7). These results, suggest that even a small amount of humic material associated with the insoluble mineral dust aerosol can enhance the CCN activation and indirect climate forcing of mineral aerosol in the Earth's atmosphere.

The average $\%f_{NaHA}$ is found to be approximately 12% and 24% NaHA in particles generated from a suspension of the PSLs in 0.01 and 0.05 wt% NaHA solutions, respectively. As discussed below, multiple particle sizing techniques were used to confirm the diameter of the PSL and to confirm that the particles were dry upon entering the SMPS and the CCN counter. For purposes of comparison, all CCN measurements reported in this study are collected for 235 nm size-selected aerosols.

It is important to note that the measured mean diameter of the PSL particles, 228(±1) nm, is not consistent with manufacturer specifications, 202(±10) nm. In order to account for the difference between the measured and reported PSL diameter, the SMPS size distributions have been measured for a range of PSL particles. With the exception of the 202 nm PSL particles, the measured mobility diameters are within specifications of the manufacturer. Additionally, upon switching DMA_2 with DMA_1, it is found that there is no difference in the measured mobility diameters between the two DMAs. The diameters of the same PSLs were also measured using Dynamic Light Scattering (DLS: Malvern Instruments, Nano-ZS), giving a hydrodynamic diameter. Using DLS, the diameters of the PSL particles are within manufacturer specifications, with the exception of the 202(±10) nm PSLs used in the present study, which has a hydrodynamic diameter of 231.3(±0.8) nm. Thus, since multiple sizing techniques were used to verify the diameter of the 202 nm PSL, it is found that the diameter of this particular PSL disagrees with manufacturer specifications reported and the DMA-measured diameter is accurate.

Figures 4-4b and 4-4c show lognormal fits to the average SMPS size distributions of polydisperse aerosol generated from 0.01 and 0.05 wt% NaHA solutions. As shown, the size distribution of pure NaHA particles shifts to larger sizes and wider distributions as the concentration of NaHA is increased. Figures 4-4b and 4-4c also show lognormal fits to the average SMPS size distributions of polydisperse PSL and $CaCO_3$ aerosol, respectively. Table 4-1 shows the mean diameters and distribution widths obtained from the lognormal distributions for these aerosols. As overlap of the size distributions between the soluble and insoluble substances will result in externally mixed aerosol, the number size distributions, dN (#/cm^3), were used to estimate the fraction of externally mixed aerosol at 235 nm. Less than 5% and 30% externally mixed NaHA aerosol is found when the aerosol is generated from a suspension of the PSL particles in 0.01 and 0.05 wt% NaHA, respectively. Furthermore, the contribution of externally mixed NaHA is approximately 0.6% and 4.8% for internally mixed $CaCO_3$-NaHA aerosol generated from 0.01 and 0.05 wt% NaHA solutions, respectively. Thus, externally mixed NaHA may impact the CCN activation of the NaHA-coated PSL to a greater extent than the NaHA-coated $CaCO_3$.

Table 4-1 Full size distribution parameters for aerosol generated from NaHA and SRFA solutions, as well as $CaCO_3$ or PSL suspensions.

	wt% humic solution	mean diameter, x (nm)	width
NaHA	1	132(±4)	0.75(±0.02)
	0.05	78(±2)	0.69(±0.03)
	0.01	65(±1)	0.65(±0.01)
SRFA	1	153(±4)	0.77(±0.02)
	0.05	84(±1)	0.76(±0.02)
	0.01	80(±1)	0.68(±0.04)
$CaCO_3$		216(±2)	0.95(±0.02)
PSL		228(±1)	0.08(±0.004)

[a]Lognormal Distribution: $y = A \exp\left[-\left(\frac{\ln(x/x_0)}{width}\right)^2\right]$

Figure 4-4d shows the lognormal fits to the average size distribution of $CaCO_3$ aerosol compared to aerosol generated from 0.05 and 0.01 wt% SRFA solutions. The distribution parameters of the polydisperse aerosols shown in Figure 4-4d are reported in Table 4-1. As with the NaHA solutions, the SRFA solutions produce more particles having larger diameters and distribution widths as the concentration of the atomized solution is increased. Similar to the NaHA-coated $CaCO_3$ aerosol, 0.7% and 3.4% of the size-selected aerosol generated from suspensions of $CaCO_3$ in 0.01 and 0.05 wt% SRFA, respectively, is composed of externally mixed SRFA particles.

4.4.4 CCN Activity of Single Component Aerosols

CCN measurements were conducted for 235 nm pure humic and fulvic acid particles and 235 nm pure PSL and $CaCO_3$ particles in order to compare the CCN activity of the single-component and internally mixed aerosol. Figure 4-7a shows the CCN activation curves of 235 nm NaHA and SRFA aerosol atomized from 1.0 wt% solutions as a function of %s. The activation curves have been normalized to the average maximum fraction in which complete activation occurs and fit to sigmoidal growth curves. The %s_c values obtained from the sigmoidal fits are 0.15(±0.01) and 0.20(±0.01) for 235 nm NaHA and SRFA particles, respectively, and are indicated in Figure 4-4a by the dashed vertical lines and reported in Table 4-2. Uncertainty in the %s_c values is based on the reproducibility of the measurements. As shown in Figure 4-6a, NaHA is slightly more CCN active than SRFA. This difference in CCN activation between the two different humic materials is likely due to their different chemical nature. For example, NaHA is in a deprotonated form as indicated by the name, humic acid sodium salt while the SRFA is in a protonated form. Additionally, slight deviation of the experimental data from the sigmoid fit is observed below 20% activation. Previous studies have observed a similar deviation in CCN measurements of humic substances and have attributed it to activation bias at low % values due to non-ideal monodispersity of

the aerosol.[14, 95] From the measured $\%s_c$ values and κ-Köhler theory,[99] as discussed previously, it is found that the hygroscopicity parameters to be $\kappa = 0.047$ and $\kappa = 0.026$ for 1.0 wt% NaHA and SRFA, respectively. These values are in reasonable agreement with CCN- and hygroscopic growth-derived values reported previously.[99]

Figure 4-7b shows the normalized CCN activation curves of 235 nm $CaCO_3$ and PSL particles. The $\%s_c$ values for the single-component 235 nm PSL and $CaCO_3$ particles are 0.37(±0.05) and 0.39(±0.01), respectively. As shown in Figure. 4-7b, the 235 nm insoluble particles have similar CCN activities and the PSLs appear to be appropriate models for insoluble dust components. The small difference between the CCN activity of the PSLs and $CaCO_3$ could be due to shape effects. The 235 nm insoluble particles were also found to be less CCN active than the 235 nm NaHA and SRFA particles shown in Figure 4-7a. However, a small amount of impurities on the insoluble particles may result in artificially low $\%s_c$ values. Thus, the $\%s_c$ values reported here for $CaCO_3$ and PSL particles may be regarded as lower limits. Using Eqs. (4-3) and (4-4), low hygroscopicity parameters of 0.008 and 0.007 were found for the PSL and $CaCO_3$ particles, respectively. These low κ values indicate that the insoluble particles are less active CCN compared to the soluble humic and fulvic acid aerosol particles of the same size. Below, results are reported from the CCN activation of internal mixtures of the insoluble particles with NaHA and SRFA.

4.4.5 CCN Activity of Internally Mixed Aerosols

Figure 4-8a shows the normalized CCN activation curves of pure 235 nm PSL particles compared to pure 235 nm NaHA particles atomized from a solution of 1.0 wt% NaHA. The CCN activation curves for internally mixed 235 nm PSL aerosol atomized from 0.01 and 0.05 wt% NaHA solutions are also shown. The error in #CCN/#CN represents uncertainty from measurement reproducibility. Humic acid coatings on the PSL aerosol were found to enhance the CCN activity of the insoluble particle. The $\%s_c$

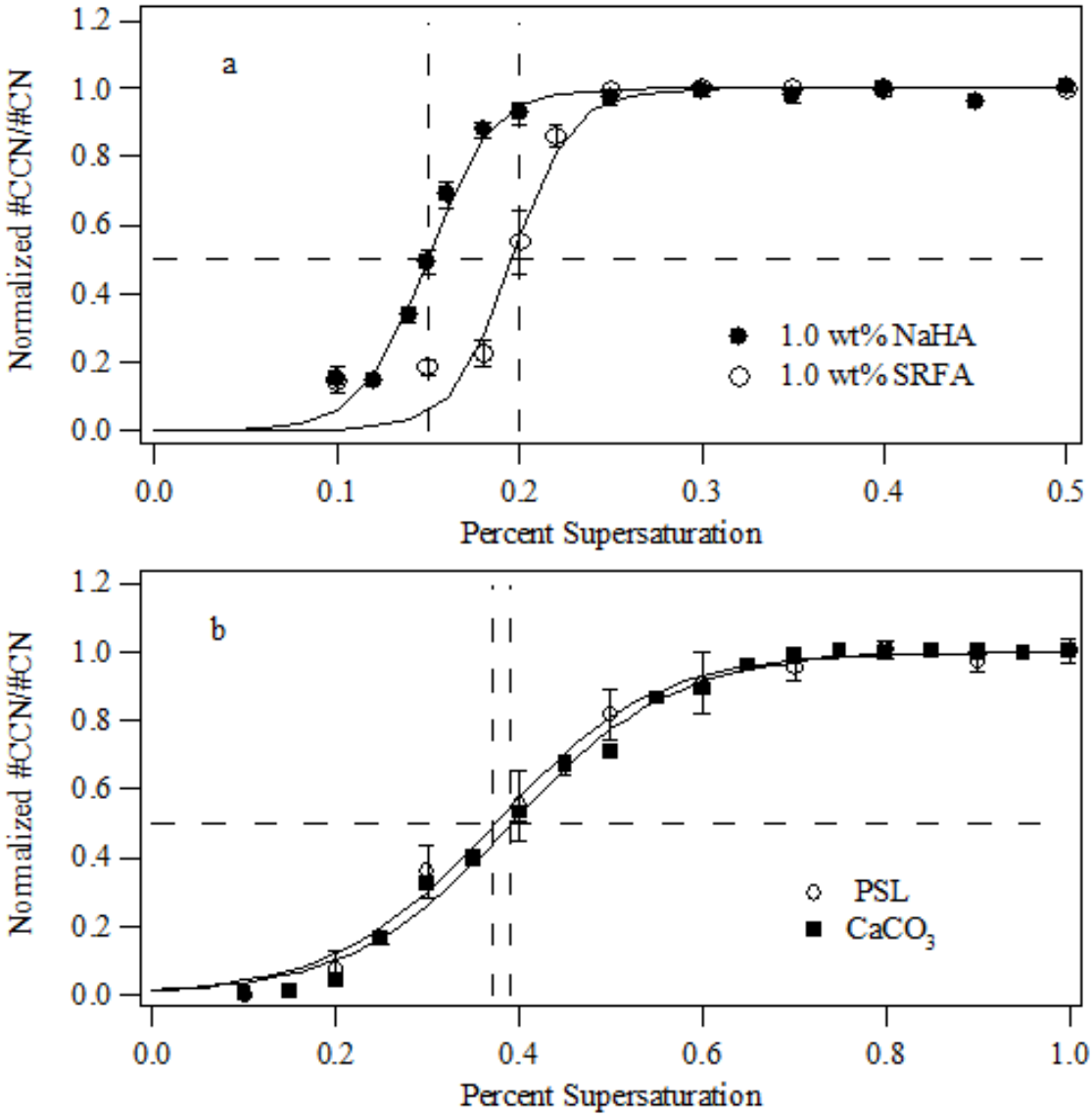

Figure 4-7 Normalized CCN activation curves for (a) 235 nm NaHA and SRFA aerosols atomized from 1.0 wt% NaHA and SRFA, respectively, and (b) 235 nm PSL and $CaCO_3$ aerosols atomized from a suspension of the particles in water. The dashed horizontal line represents 50% activation and the dashed vertical lines represent the measured $\%s_c$ obtained from the sigmoidal fits to the data.

Table 4-2 Critical percent supersaturation, $\%s_c$, values obtained from sigmoid fits[a] to the CCN data for all soluble, insoluble and coated particles size-selected at 235 nm.

Particle type	Soluble coating	wt% humic solution	$\%s_c$	$\%s_c$
NaHA		1.0	0.15	0.01
SRFA		1.0	0.20	0.01
PSL			0.37	0.05
	NaHA	0.01	0.30	0.02
	NaHA	0.05	0.30	0.03
$CaCO_3$			0.39	0.01
	NaHA	0.01	0.34	0.01
	NaHA	0.05	0.32	0.01
	SRFA	0.01	0.40	0.02
	SRFA	0.05	0.35	0.02

[a]Sigmoid fit: $y = base + \frac{max}{1 + \exp\left(\frac{x_{1/2} - x}{rate}\right)}$; $base = 0$; $max = 1$

values for the 235 nm PSL aerosol increases from 0.37(±0.05) to 0.30(±0.02) and 0.30(±0.03) for PSL aerosol generated from a suspension of PSLs in water, 0.01 and 0.05 wt% NaHA solutions, respectively. Thus, the CCN activity is not impacted by increasing the concentration of the atomized humic acid solutions from which the aerosol is generated. This result is observed because 235 nm particles, all of which have 228 nm PSL core,are size-selected and thus the mass fraction of NaHA coating does not vary and is independent of the concentration of NaHA in the solution. However, it is apparent that a small amount of soluble humic acid coating can enhance the CCN activation of the insoluble aerosol.

Figure 4-8b shows normalized CCN activation curves of the single-component 235 nm $CaCO_3$ and NaHA aerosol. As with the PSL aerosol, the $CaCO_3$ is significantly less CCN active than the pure NaHA aerosol and the $\%s_c$ for $CaCO_3$ is found to be higher by almost a factor of three compared to the pure NaHA aerosol. Figure 4-6b also shows

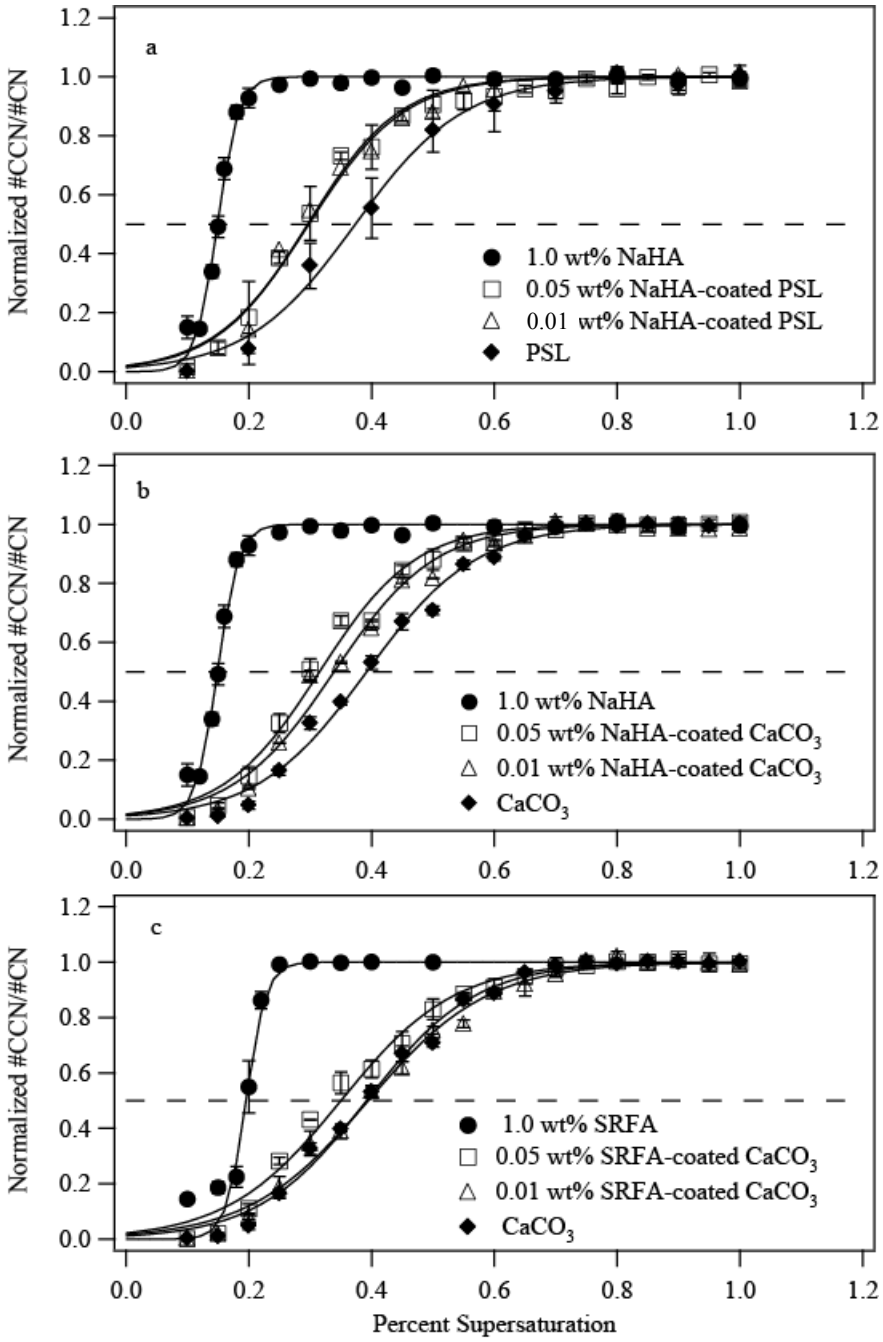

Figure 4-8 The normalized CCN activation curves and sigmoidal fits to the data for the (a) single-component 235 nm NaHA from a 1.0 wt% solution, the PSL aerosol and the 235 nm NaHA-coated PSL aerosol, (b) for single-component 235 nm $CaCO_3$ and NaHA, from a 1.0 wt% NaHA solution, and the 235 nm NaHA-coated $CaCO_3$ aerosol, and (c) 235 nm $CaCO_3$ and SRFA, from a 1.0 wt% solution, and the 235 nm SRFA-coated $CaCO_3$ aerosol. The dashed horizontal line represents 50% activation.

the CCN activation curves for 235 nm NaHA-coated $CaCO_3$ aerosol generated from a suspension of the $CaCO_3$ in 0.01 and 0.05 wt% NaHA solutions. Similar to the NaHA-coated PSLs, the CCN activity of the NaHA-coated $CaCO_3$ aerosol is enhanced compared to pure $CaCO_3$. Additionally, a slight increase in CCN activity is observed as the concentration of the NaHA solution is raised. The $\%s_c$ increases from a value of 0.39(±0.01) for the single-component $CaCO_3$ to 0.34(±0.01) and 0.32(±0.01) percent for the NaHA-coated $CaCO_3$ aerosol generated from 0.01 and 0.05 wt% NaHA solutions, respectively. This result is because as the diameter of the $CaCO_3$ core varies, the NaHA coating thickness varies depending on the concentration of NaHA solution. Thus, the coating thickness appears to influence the CCN activity of the aerosol. As shown in Table 4-2, the $\%s_c$ values for internally mixed PSL particles with NaHA are less than the values obtained for internally mixed $CaCO_3$ particles with NaHA. This result may be due to a greater contribution from externally mixed in the internal mixture of PSLs with NaHA compared to the NaHA/$CaCO_3$ internal mixture.

Figure 4-8c shows normalized CCN activation curves for pure 235 nm $CaCO_3$ aerosol compared to 235 nm SRFA particles atomized from a 1.0 wt% SRFA solution. Also shown are the normalized CCN activation curves for 235 nm SRFA-coated $CaCO_3$ particles generated from a suspension of the $CaCO_3$ particles in 0.01 and 0.05 wt% SRFA solutions. As was observed with the CCN activation of NaHA-coated $CaCO_3$ aerosol, the $\%S_c$ of the SRFA-coated $CaCO_3$ aerosol increases from 0.39(±0.01) percent for the single-component $CaCO_3$ to 0.35(±0.02) percent for aerosol generated from 0.05 wt% SRFA. However, unlike the internally mixed $CaCO_3$-NaHA particles, the CCN activity of the $CaCO_3$-SRFA aerosol generated from 0.01 wt% SRFA solution does not significantly differ from the CCN activity of the single-component $CaCO_3$ aerosol. This result is probably because SRFA is less CCN active than NaHA due to the different chemical nature of the two humic substances, as discussed previously. Thus, the SRFA alters the CCN activity of the internally mixed aerosol less than the NaHA.

Experimental $\%s_c$ values obtained from the NaHA- and SRFA-coated $CaCO_3$ aerosols can be used to calculate κ values. κ values of 0.009 and 0.010 were calculated for $CaCO_3$ particles generated from a suspension of the powder in 0.01 and 0.05 wt% NaHA, respectively, using Eqs. (4-3) and (4-4). Additionally, κ values of 0.007 and 0.009 were calculated for $CaCO_3$ particles generated from a suspension of the powder in 0.01 and 0.05 wt% SRFA, respectively. These values are similar to those calculated for the insoluble components. Based on the simple mixing rule given in Eq. (4-5), the κ value of the multi-component aerosol can be predicted. Given the calculated percent mass fractions of soluble material calculated for the particles as less than 1% and 7% humic by mass and using densities of 2.85 and 1.5 g/cm^3 for the $CaCO_3$ and humic substances, respectively, the volume fraction of the single components in the coated particles can be estimated. Predictions based on the simple mixing rule result in κ values of <0.008 and <0.012 for $CaCO_3$ particles generated form 0.01 and 0.05 wt% NaHA solutions, respectively. Additionally, κ values of <0.007 and <0.009 are predicted for $CaCO_3$ particles generated from 0.01 and 0.05 wt% SRFA solutions, respectively. These values are in excellent agreement with those calculated from experimental data. Thus, κ values can be accurately predicted if the volume fractions of the individual components are known.

CCN measurements of humic-coated mineral dust suggest that a small amount of soluble humic material associated with mineral particles can impact the indirect climate effect of mineral dust aerosol. However, application of our CCN results to atmospheric HULIS must be made with caution because previous studies have shown that terrestrially-derived humic substances may behave differently from atmospheric HULIS. For example, atmospheric HULIS has been found to be more CCN active[50, 93] and more hygroscopic[93] than fulvic acid. As a result, the measured $\%S_c$ values reported here are likely to be upper limits to the true values for HULIS aerosol and thus the enhanced CCN

activity of the coated mineral aerosol may be even more important in the Earth's atmosphere.

4.4.6 Modeling CCN Activity of $CaCO_3$

Köhler theory does not work well for insoluble particles.[14, 79] However, previous results suggest that wettable, insoluble particles may be important CCN under atmospheric conditions.[79] The CCN activation of wettable, insoluble particles, assuming droplet growth by multilayer adsorption, has recently been studied theoretically.[79] Conceptually, Köhler theory is modified by replacing the solute term with a water adsorption isotherm, using the Frenkel, Halsey and Hill (FHH) or Brunauer, Emmet and Teller (BET) multilayer adsorption models. However, this theory has yet to be tested experimentally. To test this theory, the water adsorption isotherm for $CaCO_3$ from QCM measurements was used, as shown in Figure 4-9. The FHH isotherm gives the saturation ratio of the gas-phase (S) as a function of the fractional monolayer (ML) coverage (θ) and is represented by the following equation:

$$S = \exp\left(\frac{-A}{\theta^B}\right) \tag{4-10}$$

where A and B are adjustable parameters and are characterize the interactions between molecules in the first layer with the surface and adjacent molecules, and interaction between the surface with adsorbate in layers beyond the first, respectively. Figure 4-7a shows the fractional ML coverage of water on $CaCO_3$ as a function of saturation ratio using the BET surface area of $CaCO_3$. Fits to the data using the FHH adsorption model (Eq. 4-10) are also shown in Figure 4-7a. As shown by the solid line, upon fitting all of the experimental data over the entire range of humidities studied, the FHH model does not fit the data well at high humidities. Thus, an FHH fit to the experimental data from

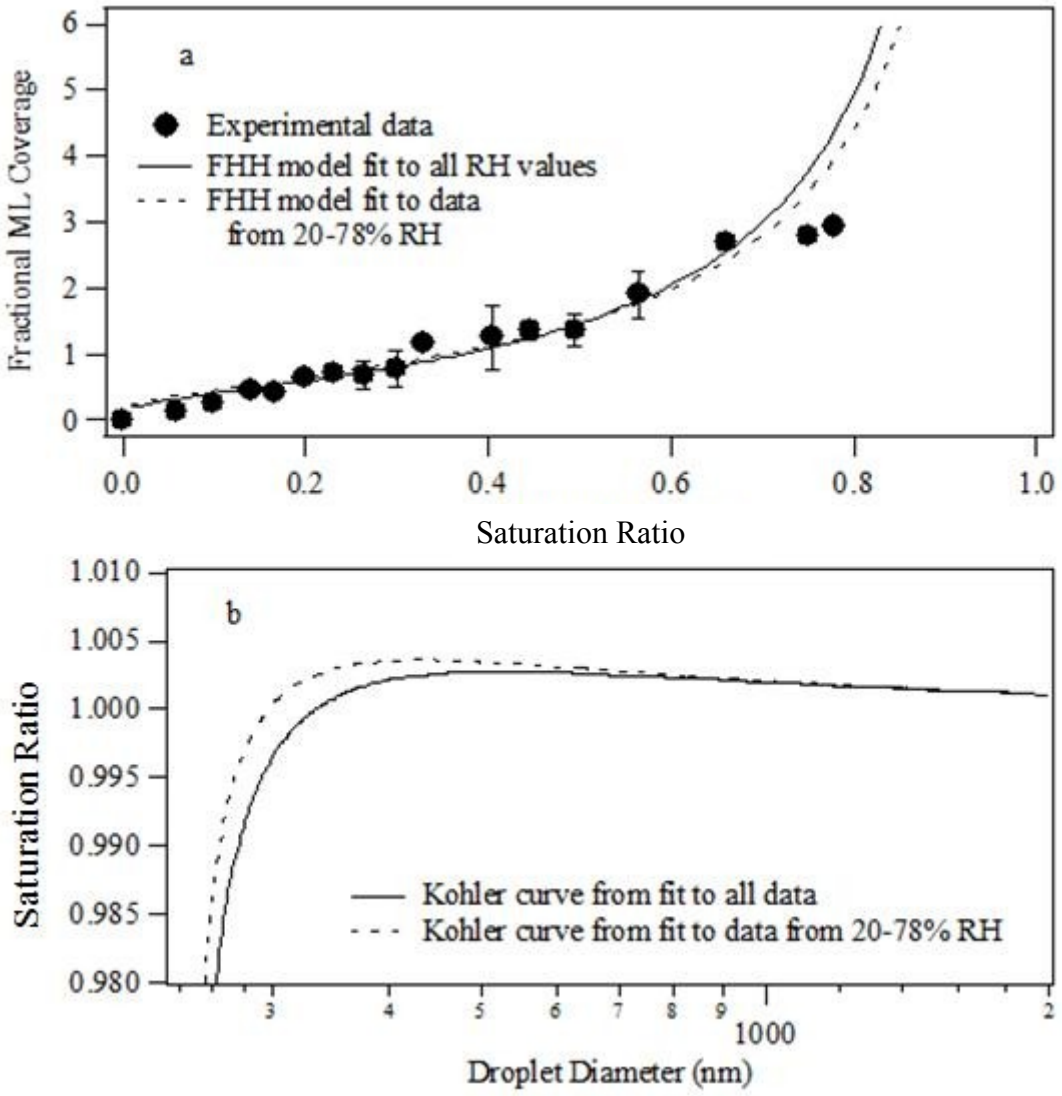

Figure 4-9 The fractional monolayer coverage of water on $CaCO_3$ obtained from the QCM and fits to the data using the FHH model over the entire range of humidities studied and from 20% to 78% RH. (b) The Köhler curves calculated using the fits the experimental data shown in (a).

20% to 78% RH is also shown. When the low relative humidity data are not included, a better fit to the high humidity data is obtained. Accurate fits to the high RH data is important for predictions of CCN activity as shown below.

In traditional Köhler theory, the saturation ratio of water vapor (S) over a solution droplet of a certain diameter (D) depends on the water activity (a_w) and the curvature of the droplet (Kelvin effect) as shown below:

$$S = a_w \exp\left(\frac{4\sigma M_w}{\rho_w RTD}\right) \tag{4-11}$$

where σ is the surface tension, assumed to be that of pure water, M_w and ρ_w are the molecular weight and density of water, respectively, and R and T are the ideal gas constant and temperature, respectively. Assuming that the driving force for insoluble particle growth is water adsorption in multiple layers on the particle surfaces, the water activity in Eq. (4-11) can be substituted with the saturation ratio calculated from the FHH adsorption isotherm to give Eq. (4-12).[79]

$$S = \exp\left(\frac{4\sigma M_w}{RT\rho_w D}\right) \times \exp\left(-A \times \theta^{-B}\right) \tag{4-12}$$

Figure 4-9b shows the Köhler curves obtained using the values for the parameters A and B determined from the FHH fit to the data shown in Figure 4-9a. From the Köhler curve obtained from fitting the FHH model over the entire range of humidities studied, a predicted $\%s_c$ of 0.28% is found. This value is less than the experimental $\%s_c$ for a 235 nm $CaCO_3$ particle by 0.11%. However, difficulty in this method may arise from uncertainty in water adsorption at high RH values, as discussed above. From the Köhler

curve obtained from fitting the FHH model from 20% to 78% RH, a predicted $\%s_c$ of 0.37% is found. This value is very close to the measured $\%s_c$ of 0.39% for the $CaCO_3$ particles. Although this new theoretical model is interesting from the perspective of water uptake over the full dynamic range, uncertainty at high humidities will result in significant error in CCN predictions. Thus, this theory may not be appropriate when water adsorption measurements at high RH values are not available or the adsorption model does not fit the data appropriately.

4.5 Conclusions and Atmospheric Implications

Atmospheric HULIS is an important substance in the Earth's atmosphere because of its light absorbing and water adsorption properties which can influence our climate directly and indirectly, respectively. Additionally, as humic substances are known to readily adsorb and retain carcinogenic species, such as polycyclic aromatic hydrocarbons,[135] submicron particles that may contain these substances may be dangerous to human health. Thus, it is important to understand the processes that govern the particle size, lifetime and climatic effects of these species, including water adsorption and CCN activation.

The water adsorption and CCN activation of two model humic substances, NaHA and SRFA, has been studied as single components and binary aerosol containing insoluble mineral particles. It is found that the CCN activity of the single-component humic substances is more efficient than that of the insoluble mineral aerosol. Additionally, our results for the SRFA, $\%s_c = 0.20$, agrees with previous studies which found a $\%s_c$ value of 0.20 for 222 nm SRFA aerosol.[95] Furthermore, the CCN activity of model humic substances is found to be similar to common biomass combustion products, such as levoglucosan and saccharides.[136] These results indicate that a small amount of humic coating on insoluble mineral particles can enhance the water adsorption and CCN activation of insoluble mineral aerosol. However, this effect may be more substantial in

the atmosphere as HULIS is more hygroscopic[93] and CCN active[50, 95] than the model humic substances studied here. Furthermore, once the cloud droplets containing HULIS have formed, the presence of light absorbing humic material in the droplets may alter the radiative impacts of clouds. This issue is worthy of additional studies as it may be an important implication for global and regional climate change.

This material is based upon work supported by the National Science Foundation under grants CHE503854 and ATM0613124. Any opinions, findings and conclusions or recommendations expressed in this material are those of the authors and do not reflect the views of the National Science Foundation. This work has been published in Hatch, C. D.; Gierlus, K. M.; Schuttlefield, J. D.; Grassian, V. H. "Water adsorption and cloud condensation nuclei activity of calcite and calcite coated with model humic and fulvic acids", *Atmospheric Environment*, **2008**, *42*, 5672-2684.

CHAPTER FIVE
LABORATORY STUDY OF THE EFFECT OF OXALIC ACID ON THE CLOUD CONDENSATION NUCLEI ACTIVITY OF MINERAL DUST AEROSOL

5.1 Abstract

Dicarboxylic acids, which make up a significant portion of the atmospheric organic aerosol, are emitted directly through biomass burning and automobile combustion as well as produced through the oxidation of volatile organic compounds. Carbonates, a significant and reactive component of mineral dust aerosol, have been found enriched in some cloud residual samples[6] providing evidence that there is potential for these coatings or aqueous reactions to occur. Oxalic acid, the most abundant of the dicarboxylic acids has been shown by recent field studies to be present in mineral dust aerosol particles. The presence of these internally mixed organic compounds can alter the water adsorption and cloud condensation nuclei (CCN) abilities of mineral particles in the Earth's atmosphere. The CCN activity of internally mixed particles that were generated from a mixture of either calcite or polystyrene latex spheres (PSLs) in an aqueous solution of oxalic acid has been measured. CCN measurements indicate that the internally mixed oxalate/calcite particles showed nearly identical CCN activity compared to the original calcite particles whereas oxalic acid/PSL internally mixed particles showed much greater CCN activity compared to PSL particles alone. This difference is due to the reaction of calcite with oxalic acid, which produces a relatively insoluble calcium oxalate coating on the particle surface and not a soluble coating as it does on the PSL particle. Our results suggest that atmospheric processing of mineral dust aerosol through heterogeneous reactions will likely depend on mineralogy and the specific chemistry involved. For reactions with oxalic acid, increases in the CCN activity can only be expected for unreactive insoluble dust particles that form a soluble coating.

5.2 Introduction

Dicarboxylic acids (DCAs) are a significant portion of the organic aerosol mass concentration, with oxalic acid being the most abundant[61-67] and having concentrations measured as high as 1.43 μg m^{-3} [63] and accounting for as much as 84% of the total DCAs. [62] The formation pathways of oxalic acid are still being investigated, but one primary source is known to be biomass burning. [68-69] Secondary production of oxalic acid occurs as well. One mechanism involves the photo oxidation of longer-chain DCAs [67, 70-71] which can be further enhanced through aqueous-phase reactions in cloud droplets. [72-74] Field measurements by Hsieh et al. of suburban aerosol in southern Taiwan reported that peak concentrations of oxalic acid occurred in the droplet mode, indicating an association with cloud-processing.[62] Model simulations [73, 75] and field studies [76] and have shown the production of secondary organic aerosols (SOAs), including oxalic acid, to be enhanced in the presence of clouds. Additionally, measurements of the contribution of oxalic acid to the total water soluble organic concentrations in New Delhi showed higher mass fractions of oxalate during nighttime compared to daytime, suggesting the production of oxalate via the oxidation of longer-chain DCAs in aqueous aerosols which were more abundant under higher relative humidity conditions present during the nighttime. [63] Similarly, sulfate which has been long recognized to form during cloud processing has been shown to have concentrations highly correlated with those of oxalate, suggesting oxalate is produced via cloud processing as well. [38, 66, 69]

Along with heterogeneous gas-phase reactions,[7-10] cloud processing has also been shown to be an important pathway for the formation of coated or internally mixed mineral dust aerosol. [6, 11] Generated from windblown soil, mineral dust can be transported globally with atmospheric lifetimes of days to weeks, during which time it can impact the Earth's climate as well as the chemical balance of the atmosphere. [3] Coating of the mineral dust particles can occur through cloud processing as the particles are collected by existing cloud droplets which were nucleated by soluble particles and

that dissolved soluble material is redistributed until evaporation leaves internally mixed particles. On a global average it has been estimated that any particular atmospheric aerosol has undergone the evaporation/condensation cycle three times, [12] and repetition of this cycle has been shown to significantly increase the mass of soluble material incorporated in dust particles. [13] Furthermore, the cloud processing of dust aerosols has been shown to increase hygroscopicity and cloud condensation nuclei (CCN) activity [17] as well as impact the location of the deposition of the dust. [18]

In a study of Asian aerosol by Sullivan and Prather, 2007, 10.2% of the mineral dust particles contained oxalic acid which was only detected in the dust particles. They have hypothesized that DCAs may be found in increased amounts in mineral dust due to their ability to chelate divalent cations such as Ca^{2+} and Mg^{2+}.[10] The presence of internally mixed oxalate has also been measured in another Asian dust aerosol, as well as a Saharan dust aerosol. [21, 69] It is also possible for calcite to react with oxalic acid to form calcium oxalate, according to:

$$CaCO_3 + H_2C_2O_4 \leftrightarrow CaC_2O_4 + CO_2 + H_2O \qquad (5\text{-}1)$$

Although the hygroscopicity [18, 77-78] and CCN activity [21] of dicarboxylic acids such as oxalic acid has been measured previously, it is still not clear how internally mixed DCAs may impact the climate forcing properties of mineral dust. Xue et al. reported increased light scattering and absorption of soot aggregates with thin coatings of dicarboxylic acids, which was further enhanced when the coated soot was exposed to high relative humidity [137] and increases in hygroscopicity and CCN activity have been measured when calcite was internally mixed with organic humic substances. [30, 138] In this study, measurements of the CCN activity of internally mixed particles generated from mixtures of either calcite ($CaCO_3$) or polystyrene latex spheres (PSLs) in an aqueous

solution of oxalic acid were made. $CaCO_3$ and PSLs were used as models for mineral dust aerosol with one being a reactive component and the other an unreactive, insoluble component. Additionally attenuated total reflectance (ATR) Fourier transform infrared (FT-IR) measurements were performed to confirm speciation of oxalate in the internally mixed calcite particles.

5.3 Experimental Methods

5.3.1 Materials

All of the chemicals used in this study were commercially available and used as received. Oxalic acid (99.999%) was purchased from Aldrich, and aerosols were generated from a 0.2 wt% by volume solution using Optima water (Fisher Scientific). Calcite (OMYA) and PSLs (Polysciences, Inc., Cat. #07304) were atomized from suspensions in Optima water. Internally mixed particles were generated by atomizing a suspension of insoluble powder in an aqueous solution of soluble material. Calcium oxalate monohydrate (99.9985%) was purchased from Alfa Aesar.

5.3.2 Size Distribution and Cloud Condensation Nuclei Activity Measurements

Size distributions and cloud droplet activation measurements have been described in detail elsewhere. [81] Aerosols were generated by a constant output atomizer (Model 3076, TSI, Inc.) from an aqueous solution or suspension as described above. The aerosol was then passed through two diffusion dryers (Model 3062, TSI, Inc.) and dried to a low relative humidity ($RH \leq 10\%$). For the CCN measurements the aerosol was passed through a differential mobility analyzer (DMA_1; Model 3080, TSI, Inc.) in order to size-select 100 nm or 200 nm monodisperse particles. This monodisperse aerosol was then split between a continuous flow streamwise thermal-gradient cloud condensation nuclei counter (Droplet Measurement Technologies; Model CCN-2) [86] and a condensation

particle counter (CPC; Model 3025A, TSI, Inc.). For a given diameter and supersaturation the CCN activity is reported as the ratio of particles that act as a cloud condensation nuclei (#CCN) to the number of particles counted by the CPC (#CN). The ammonium sulfate activity data presented by Tang and Munkelwitz was used to calibrate the supersaturation generated in the CCN counter to the thermal gradient of the diffusion chamber. [87] This is useful so as to compare to other measurements made previously in our laboratory. Full size distributions were measured by bypassing DMA_1 and directing the dry polydisperse aerosol into a scanning mobility particle sizer (SMPS; Model 3936, TSI, Inc.), which consists of a second DMA (DMA_2) coupled to the CPC.

5.3.3 Infrared Absorption Measurements

ATR-FTIR spectroscopy was used to measure infrared spectra of thin films of calcium oxalate, calcite, and calcite reacted with oxalic acid from 800 to 4000 wavenumbers (cm^{-1}) at 4 cm^{-1} resolution by averaging 256 scans, employing a single beam spectrometer (Thermo Nicolet, Model 6700, equipped with a nitrogen-cooled MCT/A detector). For these measurements samples were spray deposited on a 7.3 cm by 0.7 cm area of the ATR-FTIR internal reflection element (IRE), resulting in a homogeneously dispersed sample, which was dried under a constant flow of air (>12 hours, RH less than 5%). The calcite and calcium oxalate were used as purchased. The reacted sample of calcite was collected from a suspension of calcite in oxalic acid that had been in the atomizer for one hour. All ATR-FTIR spectra were referenced to the background signal of the blank IRE collected under dry conditions.

5.3.4 Theoretical Methods

A hygroscopicity parameter, κ, has recently been developed using "κ-Köhler theory" [99-100] in order to determine a single parameter which can be used to describe both hygroscopic growth and CCN activity. In κ-Köhler theory, the saturation ratio, *S*, is expressed in the following equation:

$$S = \left(\frac{D_p^3 - D_o^3}{D_p^3 - D_o^3(1-\kappa)} \right) \exp\left(\frac{4M_w\sigma_s}{RT\rho_w D_p} \right) \tag{5-2}$$

where κ is the hygroscopicity parameter, D and D_d are the aqueous droplet diameter and the dry diameter, respectively, σ_s is the surface tension of the solution/air interface, R is the ideal gas constant, T is the temperature, and M_w and ρ_w are the molecular weight and density of water, respectively. The following equations [99] can be used to determine the hygroscopicity parameter:

$$\kappa = \frac{4A^3}{27D_d^3 \ln^2 S_c} \tag{5-3}$$

$$A = \frac{4\sigma_s M_w}{RT\rho_w} \tag{5-4}$$

where S_c, the critical saturation, is the saturation needed for half of the particles to nucleate cloud droplets, and is related to the critical supersaturation, s_c, by $s_c=S_c-1$. For calculation of the κ values of the aerosol particles studied a temperature of 298.15 K and a surface tension for pure water of 0.072 Jm^{-2} were assumed. [130]

5.4 Results and Discussion

5.4.1 Size Distributions

Full size distributions for the individual components studied are shown in Figure 5-1 by lognormal curve fits to the average of multiple measurements. Peak diameters are 45 nm for 0.2 wt% oxalic acid (long dashed curve), 195 nm for calcite (solid curve), and

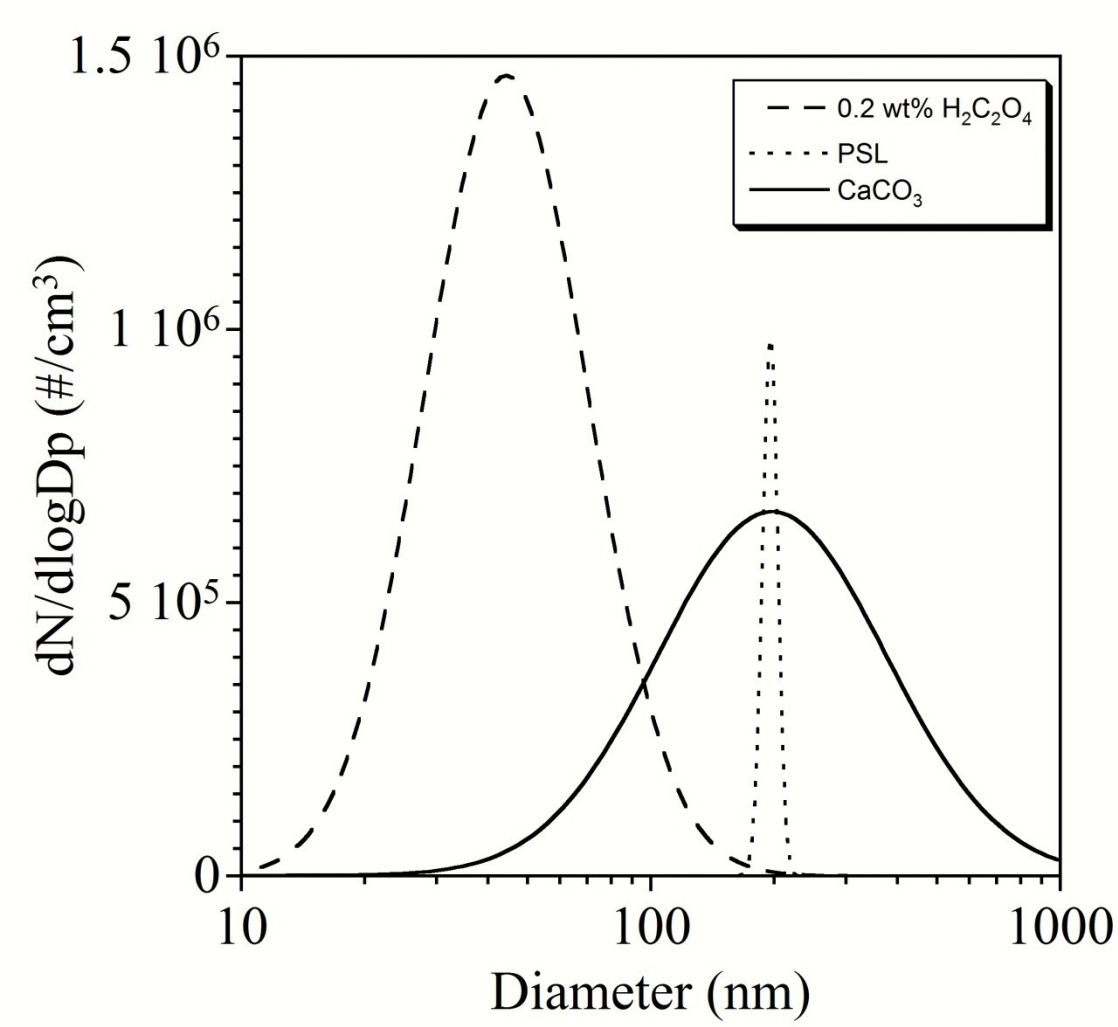

Figure 5-1 Lognormal curve fits to the average of multiple measurements of the full size distributions of 0.2 wt% $H_2C_2O_4$ (dashed), PSL (dotted), and $CaCO_3$ (solid).

196 nm for PSLs (short dashed curve). When generating internally mixed particles the insoluble component (calcite or PSLs) was atomized in a 0.2 wt % solution of the soluble component (oxalic acid), and size selected at 200 nm. The use of a particle size near 200 nm was necessary to minimize the amount of externally mixed oxalic acid. The amount of externally mixed oxalic acid or ammonium sulfate particles can be predicted to a first approximation by dividing the concentration of soluble particles at 200 nm by the total concentration of particles at 200 nm (soluble plus insoluble component), as measured by the CCN. From the size distributions of the individual components, it is estimated that for $CaCO_3$ there would less than 1.0% externally mixed oxalic acid and for PSLs there would be less than 0.7% externally mixed particles.

Figure 5-2 shows the full size distributions of the particles generated by atomizing calcite in an aqueous solution of oxalic acid. Size distributions were measured continuously over intervals of three and a half minutes for about 1.5 hr. The size distributions have been normalized such that the maximum concentration of the peak centered at approximately 200 nm is one. The arrow demonstrates the decrease in concentration with time of the peak at smaller diameters. When calcite was atomized in a solution of 0.2 wt% oxalic acid initially the size distribution was bimodal demonstrating the presence of externally mixed oxalic acid particles at approximately 60 nm, however, this peak is found to decrease significantly as a function of time and is near baseline after ca. 30 minutes. This change is attributed to the reaction of oxalic acid with calcite to yield calcium oxalate. In comparison when PSLs were atomized in a solution of 0.2 wt% oxalic acid the externally mixed oxalic acid particles showed little decrease in concentration and peak diameter.

5.4.2 CCN Activity of 200 nm Particles

In order to study the effect on CCN activity, internally mixed or reacted particles were generated from a mixture of either PSLs or $CaCO_3$ in an aqueous solution of 0.2

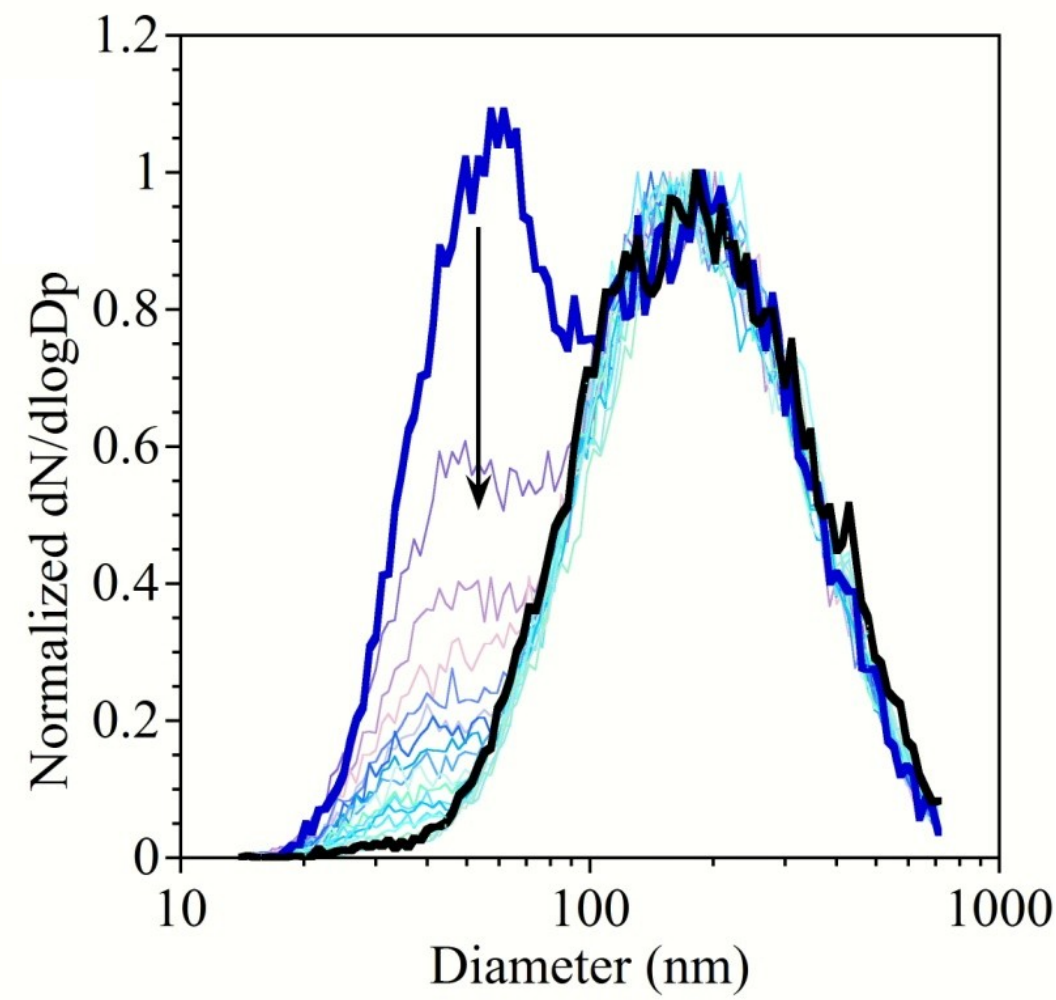

Figure 5-2 Full size distributions of calcite atomized in a solution of 0.2 wt% oxalic acid. The size distributions have been normalized such that the maximum concentration of the peak centered at approximately 200 nm is one. The arrows demonstrate the decrease in the peak at approximately 45 nm over time with the first measurement shown by the bold blue curve and the last by the bold black curve.

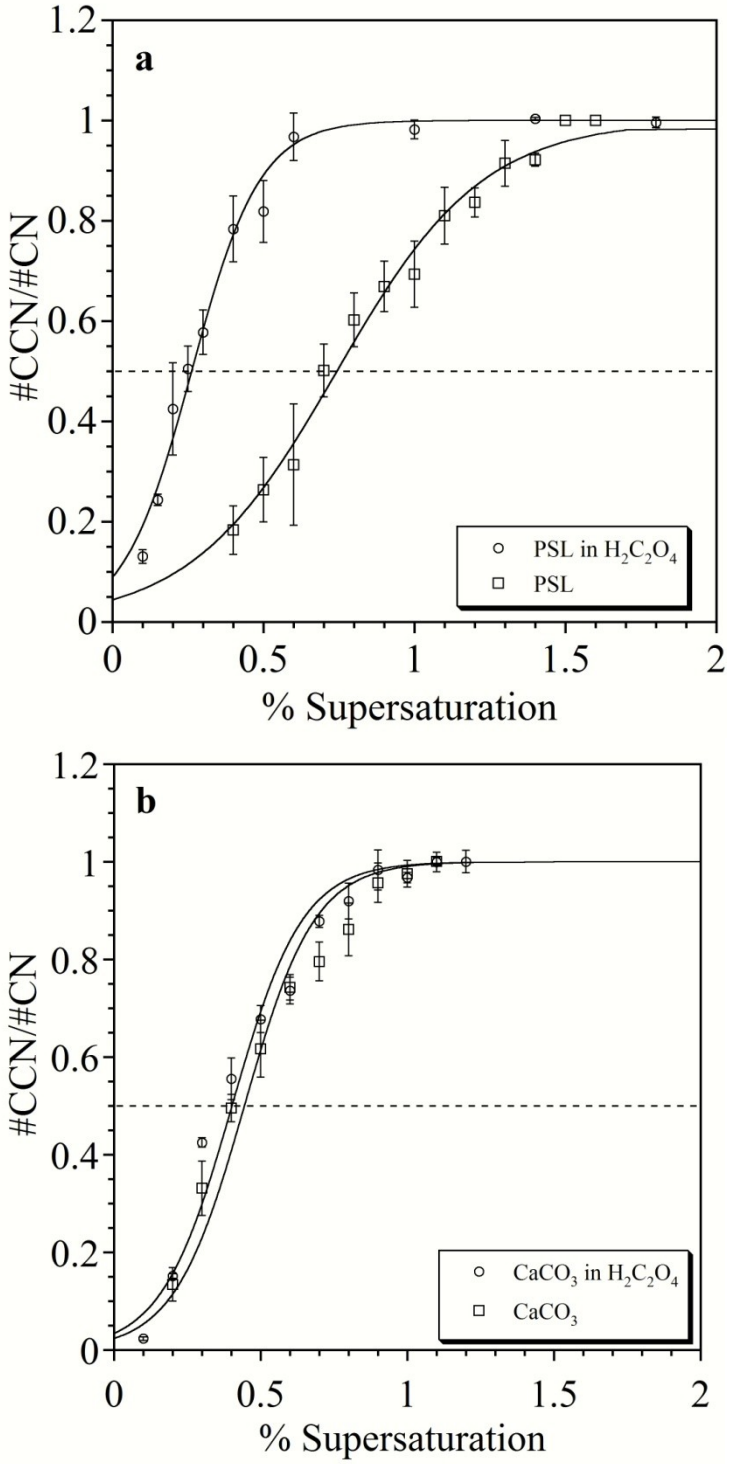

Figure 5-3 CCN activity of 200 nm (a) PSL (squares) and PSLs atomized in oxalic acid (circles) and (b) calcite (squares) and calcite atomized in oxalic acid (circles). Each data point is the average of 3-10 measurements and the error bars represent the standard deviation of these multiple measurements. The solid black lines represent sigmoidal fits to the data. The dashed line represents the 50% activation point.

Table 5-1 Measured values of % s_c and corresponding hygroscopicity parameters for 200 nm particles.

Particle Type	Measured % s_c	Hygroscopicity Parameter
PSL	0.74 ± 0.09	0.003
Oxalic acid coated PSL	0.26 ± 0.03	0.025
Calcite	0.44 ± 0.04	0.009
Oxalate reacted calcite	0.40 ± 0.03	0.011

wt% oxalic acid. Figure 5-3a shows normalized CCN activity of PSLs atomized in oxalic acid and size selected at 200 nm. The % s_c of the PSLs decreased from 0.74 ± 0.09 (κ = 0.003) for uncoated to 0.26 ± 0.03 (κ = 0.025) for PSLs with internally mixed oxalic acid.

This large increase in CCN activity demonstrates that the incorporation of small amounts of soluble material can significantly alter the nucleation properties of insoluble aerosols. The CCN activity of pure 200 nm oxalic acid was not measured as it lies outside the range of our instrument (% s_c < 0.1%). It should also be noted that the PSL sample used in this study was different than the PSL sample used in Chapter Four. This PSL sample has a much larger %s_c than the PSLs used in Chapter Four. This can partially be attributed to a difference in the size-selected diameter (200 nm for these and 235 nm for the previous study). The presence of soluble material in the PSL surfactant will also increase the CCN activity of the particles, and this also contributes to the variability in CCN activity.

Figure 5-3b shows the CCN activity of calcite and oxalate/calcite particles. The % s_c of the 200 nm calcite particles was measured to be 0.44 ± 0.04 (κ =0.009) which is in agreement with previous measurements made in our laboratory (% s_c = 0.37 ± 0.02), [15] however, is much lower than those reported for calcite aerosolized using a dry technique (% s_c = 0.730) [78] It has been suggested that this difference is due to trace contaminants in the water used for atomization leading to enhanced hygroscopicity of the insoluble particles being generated. [125, 139] When atomized in aqueous oxalic acid for > 30 min. the

resulting calcite particles had a % s_c of 0.40 ± 0.03 (κ = 0.011), which is only slightly more CCN active than the pure calcite particles. This is a much smaller enhancement, essentially no enhancement, in CCN activity as compared to the internally mixed oxalic acid-PSL particles. This difference in CCN enhancement is due to the reaction of the calcite with oxalic acid to produce a coating of calcium oxalate. As described in the next section, spectroscopic measurements provide evidence of the reaction product.

5.4.3 ATR FT-IR Measurements.

ATR FT-IR spectroscopy measurements of thin films were performed in order to confirm the presence of calcium oxalate in the reacted calcite particles. Spectra of calcium oxalate and calcite were also collected for comparison. As seen in Figure 5-4 the reference spectra for calcium oxalate shows absorption bands at 1607 and 1317 cm^{-1} due to the asymmetric carbonyl stretching mode and symmetric carbonyl stretching mode, respectively. This is consistent with calcium oxalate monohydrate which has been shown to have bands at 1618 and 1317 cm^{-1}, compared to the dhydrate or trihydrate which have bands at 1646 and 1327 cm^{-1} or 1670 and 1325 cm^{-1}, respectively [140]. Observed bands at lower wavenumbers are also characteristic of the monohydrated calcium oxalate (948 and 884 cm^{-1}), compared to the dihydrate (914 cm^{-1}) or trihydrate (876 and 845 cm^{-1}) [140]. ATR FT-IR spectrum of pure calcite does not have any of these peaks, as seen in the reference spectrum. Peaks characteristic of calcite are seen at 874 and 1396 cm^{-1}. However, calcite after reaction with oxalic acid shows additional peaks close in frequency to that of calcium oxalate. In particular, the spectrum of oxalic acid-reacted calcite shows absorptions at 849, 1325, and 1620 cm^{-1} suggesting the presence of calcium oxalate monohydrate and trihydrate species. These data confirm that reaction chemistry can be used to explain the CCN activity as calcium oxalate coats the surface and is an insoluble coating compared to oxalic acid, and therefore does not enhance the CCN activity of the calcite.

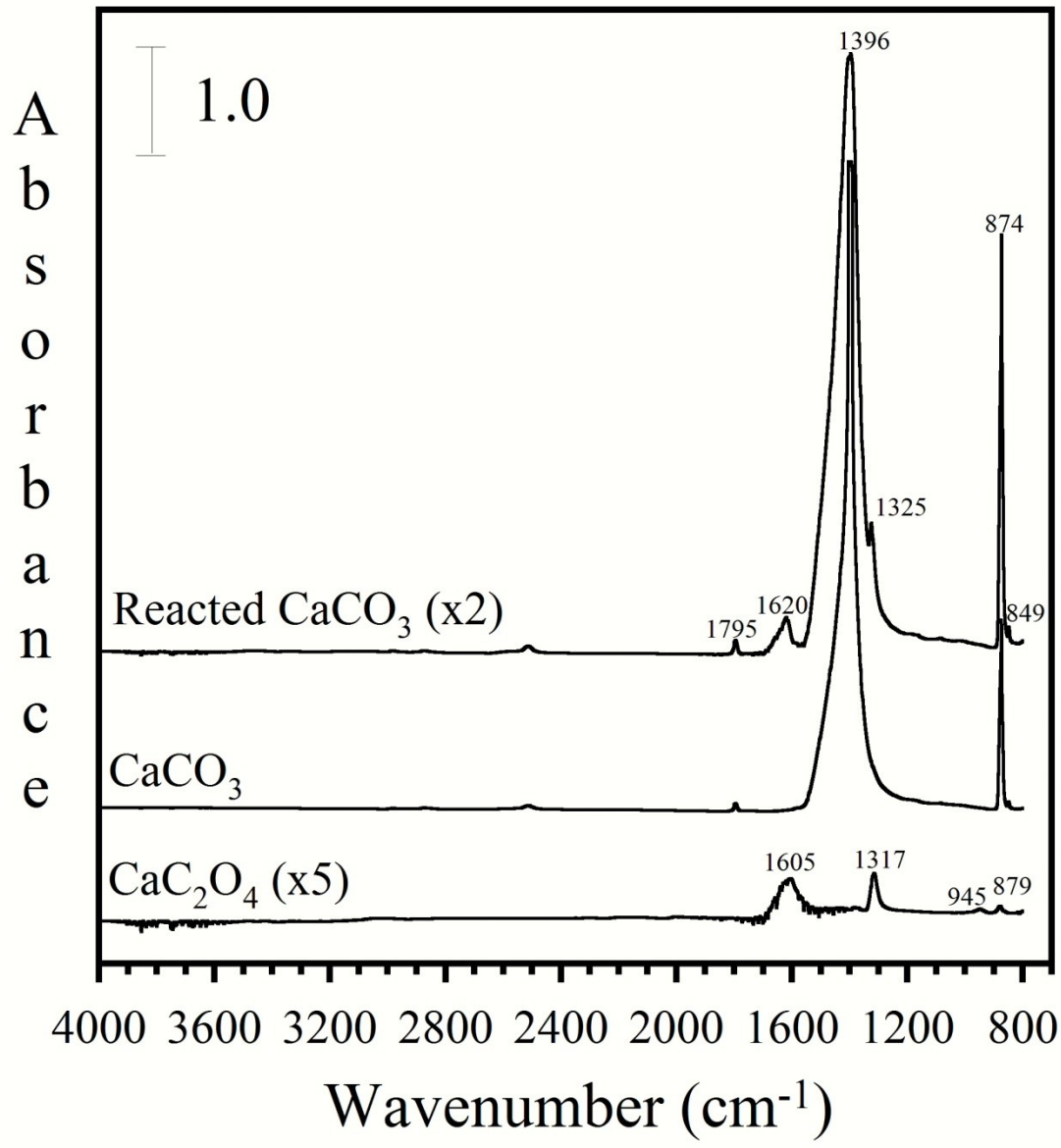

Figure 5-7 ATR FT-IR spectra collected for calcium oxalate, calcite, and calcite reacted with oxalic acid during atomization. The calcium oxalate data has been enhanced by a factor of 5 and the reacted calcite by a factor of 2.

5.5 Summary

Internally mixed particles were generated to model processed dust in the atmosphere. PSL particles which had been generated from a suspension in oxalic acid were significantly more CCN active than PSL particles alone. These mixed composition particles represent a model for an unreactive mineral dust core with a soluble coating. However, in some cases, components of mineral dust aerosol will likely react such as seen in the formation of calcium oxalate from oxalic acid. CCN measurements indicated that the internally mixed oxalate/calcite particles were showed no significant enhancement in CCN activity compared to the internally mixed PSL particles, which is reflective of the decreased hygroscopicity and CCN activity of the oxalate species as compared to oxalic acid. ATR FT-IR measurements were used to confirm the presence of a calcium oxalate coating on the calcite particle. This study demonstrates the link between interfacial chemistry and climate, the specificity of mineral dust aerosol chemistry and the importance of mineralogy.

This material is based upon work supported by the National Science Foundation under Grant No. CHE-0952605. Any opinions, findings, and conclusions or recommendations expressed in this material are those of the author and do not necessarily reflect the views of the National Science Foundation. This work has been accepted by *Atmospheric Environment* for publication.

CHAPTER SIX

CONCLUSIONS

The hygroscopicity and CCN activity of atmospheric aerosol play a key role in understanding the radiative balance. This includes the direct and indirect aerosol effects, both of which currently have a low level of scientific understanding.[2] Much of the uncertainty in these areas reflects the complexity of aerosol composition. The composition of freshly emitted mineral dust aerosol varies depending on the region from which it originates.[4-5] Understanding of the composition is further complicated by the fact that fresh mineral dust can quickly be processed and aged as it is transported in the atmosphere. Both heterogeneous reactions and cloud processing can contribute to the atmospheric aging of the aerosol. These processes will in turn have an effect on the physicochemical properties of the aerosol.

In this work, the effect of atmospheric aging on the physicochemical properties of mineral dust aerosol was investigated. Hygroscopicity and CCN activity measurements were performed using laboratory generated aerosol which modeled the type of processed dust that has been found in the atmosphere. Calcite or polystyrene latex (PSL) spheres were used as models for the insoluble mineral dust component, and humic acid, fulvic acid, and oxalic acid were used to study the effect of internally mixed or reacted organics.

The hygroscopic growth of humic acid and fulvic acid aerosols was measured using hTDMA. Further investigation of the composition of the humic and fulvic acids and the water uptake properties of thin films and aerosol was done by ATR and extinction FTIR, respectively. The results from these studies demonstrated that humic and fulvic acids do have comparable hygroscopicity to the humic-like substances (HULIS) found in the atmosphere, and can, with some care, be used as models for HULIS. The physicochemical properties of humic and fulvic acid were further investigated by measurement of their CCN activities. Additionally, the CCN activity of

calcite and PSLs was measured and found to be comparable to one another, but significantly less than that measured for the humic and fulvic acids. This suggests that the processing of mineral dust aerosol with HULIS will increase the CNN activity. By generating internally mixed humic acid/PSLs and humic acid/calcite particles this was shown to be true. The humic acid coatings formed on the insoluble particles were characterized using SMPS size distributions and TEM. The CCN activities for these internally mixed particles were also shown to be enhanced in comparison to the uncoated calcite or PSL aerosol. This enhancement in water uptake was also demonstrated at sub-saturated relative humidities by the use of QCM to measure adsorbed water on calcite internally mixed with humic/fulvic acid.

Oxalic acid, the most abundant of the dicarboxylic acids, is readily found in the atmosphere, and the processing of mineral dust with oxalic acid was investigated. An oxalic acid coating would be expected to enhance the CCN acitivty of an insoluble core particle, and this was demonstrated by generating internally mixed oxalic acid/PSL particles. However, rather than simply coating the calcite, the oxalic acid reacted with the calcite during particle generation to produce oxalate on the particles' surface. The speciation of the oxalate coating on the calcite particles was confirmed by ATR FTIR measurements. Because calcium oxalate has a much lower CCN activity than oxalic acid, no significant enhancement of the calcite CCN activity was found when reacted with oxalic acid.

This work very clearly demonstrates the relationship between the physicochemical properties of an aerosol and the changes in surface composition due to atmospheric processing. In order to improve our understanding of the contribution of the aerosol effects to the climate's radiative balance, a continued effort to improve our understanding of the atmospheric processing of aerosols is needed. This begins with additional field studies to better elucidate not only the composition of atmospheric particles, but also the mechanisms by which they are processed (i.e. heterogeneous

reactions, cloud processing, etc.). As field measurements of atmospheric aerosols continue to increase in number and detail, future laboratory work should continue to focus on ways to better model atmospheric processing. In this work the coated or reacted particles best model the type of processing that occurs in cloud droplets. In the future, further modification of the MAARS system could enable the study of heterogeneous reactions as a method of aerosol processing. Additionally, while there has been much focus on the CCN activity of aerosols, there is a need for additional studies of ice nucleation (IN) activity. Lastly, modeling studies will need to incorporate field and laboratory findings in order to improve the estimates of the aerosol direct and indirect radiative forcing effects. This combined effort is necessary to better understand the contributions of aerosols to the balance of the climate.

REFERENCES

1. Lohmann, U.; Feichter, J., *Atmospheric Chemistry and Physics* **2005,** *5*, 715-737.

2. IPCC, *Cambridge University Press* **2007**.

3. Bauer, S. E.; Balkanski, Y.; M., S.; Hauglustaine, D. A.; Dentener, F., *J. Geophys. Res.* **2004,** *109*.

4. Claquin, T.; Schulz, M.; Balkanski, Y., *J. Geophys. Res.* **1999,** *104* (D18).

5. Formenti, P.; Shutz, L.; Balkanski, Y.; Desboeufs, K.; Ebert, M.; Kandler, K.; Petzold, A.; Scheuvens, D.; Weinbruch, S.; Zhang, D., *Atmos. Chem. Phys.* **2011,** *11*, 8231-8256.

6. Matsuki, A.; Schwarzenboeck, A.; Venzac, H.; Laj, P.; Crumeyrolle, S.; Gomes, L., *Atmos. Chem. Phys.* **2010,** *10*, 1057-1069.

7. Sullivan, R. C.; Moore, M. J. K.; Petters, M. D.; Kreidenweis, S. M.; Roberts, G. C.; Prather, K. A., *Phys. Chem. Chem. Phys.* **2009,** *11*, 7826-7837.

8. Krueger, B. J.; Grassian, V. H.; Cowin, J. P.; Laskin, A., *Atmospheric Environment* **2004,** *38* (36), 6253-6261.

9. Usher, C. R.; Michel, A. E.; Grassian, V. H., *Chem. Rev.* **2003,** *103* (12), 4883-4939.

10. Sullivan, R. C.; Prather, K. A., *Environ. Sci. Technol.* **2007,** *41* (8062-8069), 8062.

11. Liu, X.; Zhu, J.; Espen, P. V.; Adams, F.; Xiao, R.; Dong, S.; Li, Y., *Atmospheric Environment* **2005,** *39*, 6909-6918.

12. Pruppacher, H. R.; Jaenicke, R., *Atmospheric Research* **1995,** *38*, 283-295.

13. Wurzler, S.; Reisin, T. G.; Levin, Z., *J. Geophys. Res.* **2000,** *105*, 4501-4512.

14. Kumar, P. P.; Broekhuzien, K.; Abbatt, J. P. D., *Atmospheric Chemistry and Physics* **2003,** *3*, 509-520.

15. Gibson, E. R.; Gierlus, K. M.; Hudson, P. K.; Grassian, V. H., *Aerosol Sci. Technol.* **2007,** *41*, 914-924.

16. Pruppacher, H. R.; Klett, J. D., *Microphysics of Clouds and Precipitation*. Reidel Publishing Company: Dordredecht, 1980.

17. Crumeyrolle, S.; Gomes, L.; Tulet, P.; Matsuki, A.; Schwarzenboeck, A.; Crahan, K., *Atmospheric Chemistry and Physics* **2008,** *8*, 6907-6924.

18. Fan, S.-M.; Horowitz, L. W.; II, H. L.; Moxim, W. J., *Geophysical Research Letters* **2004,** *31*, L102104.

19. Simoneit, B. R. T.; Cahill, T. A.; Mazurek, M. A., *Journal of the Air Pollution Control Association* **1980,** *30*, 387-390.

20. Russell, L. M.; Maria, S. F.; Myneni, S. C. B., *Geophysical Research Letters* **2002,** *29*.

21. Falkovich, A. H.; Schkolnik, G.; Ganor, E.; Rudich, Y., *J. Geophys. Res.* **2004,** *109*.

22. Saxena, P.; Hildermann, L. M.; McMurry, P. H.; Seinfeld, J. H., *Journal of Geophysical Research - Atmospheres* **1995,** *100*, 18755-18770.

23. Andreae, M. O.; Crutzen, P. J., *Science* **1997,** *276*.

24. Saxena, P.; Hildermann, L. M., *Journal of Atmospheric Chemistry* **1996,** *24*.

25. Fuzzi, S.; Andreae, M. O.; Huebert, B. J.; Kulmala, M.; Bond, T. C.; Boy, M.; Doherty, S. J.; Buenther, M.; Kanakidou, V.-M.; Lohmann, U.; Russell, L. M.; Poschl, U., *Atmospheric Chemistry and Physics* **2006,** *6*.

26. Kanakidou, V.-M.; Seinfeld, J. H.; Pandis, S. N.; Dentener, F. J.; Facchini, M. C.; Van Dingenen, R.; Ervens, B.; Nenes, A.; Nielson, C. J.; Swietlicki, E.; Putaud, J. P.; Balkanski, Y.; Fuzzi, S.; Horth, J.; Moortgat, G. K.; Winterhalter, R.; Myhre, C. E. L.; Tsigaridis, K.; Vignati, E.; Stephanou, E. G.; Wilson, J., *Atmospheric Chemistry and Physics* **2005,** *5*.

27. Abdul-Razzak, H.; Ghan, S. J., *Journal of Geophysical Research* **2005,** *110*.

28. Chan, M. N.; Chan, C. K., *Environmental Science & Technology* **2003,** *32*, 5109-5115.

29. Dinar, E.; Anttila, T.; Rudich, Y., *Environmental Science & Technology* **2008,** *42*, 793.

30. Hatch, C. D.; Gierlus, K. M.; Schuttlefield, J. D.; Grassian, V. H., *Atmospheric Environment* **2008,** *42*, 5672-5684.

31. Hemming, B. L.; Seinfeld, J. H., *Ind. Eng. Chem. Res.* **2001,** *40*.

32. Alves, C.; Pio, C.; Duarte, A., *Atmospheric Environment* **2001,** *35*.

33. Graham, B.; Mayol-Bracero, O. L.; Guyon, P.; Roberts, G. C.; Decesari, S.; Facchini, M. C.; Artaxo, P.; Maehaut, W.; Koll, P.; Andreae, M. O., *Journal of Geophysical Research* **2002,** *107* (D20).

34. Pio, C.; Alves, C.; Duarte, A., *Atmospheric Environment* **2001,** *35*.

35. Rogge, W. F.; Mazurek, M. A.; Hildermann, L. M.; Cass, G. R.; Simoneit, B. R. T., *Atmospheric Environment* **1993,** *27A*.

36. Alves, C.; Carvalho, A.; Pio, C., *Journal of Geophysical Research* **2002,** *107* (D21).

37. Salma, I.; Ocskay, R.; Varga, W.; Maenhaut, W., *Journal of Geophysical Research* **2006,** *111*.

38. Yu, J. Z.; Huang, X.-F.; Xu, J.; Hu, M., *Environ. Sci. Technol.* **2005,** *39*, 128-133.

39. Donaldson, D. J.; Vaida, V., *Chem. Rev.* **2006,** *106*.

40. Falkovich, A. H.; Graber, E. R.; Schkolnik, G.; Rudich, Y.; Maenhaut, W.; Artaxo, P., *Atmospheric Chemistry and Physics* **2005,** *5*.

41. Stevenson, F. J., *Humus Chemistry*. Wiley: New York, 1994.

42. Stevenson, F. J., *Humus chemistry genesis, composition, reactions.* . Willey Interscience: New York, 1982.

43. Cini, R.; Petronio, B. M.; Deliinnocenti, N.; Stortini, A. M.; Braguglia, C.; Calace, N., *Annali di Chimica* **1994,** *84*, 425-430.

44. Cavalli, F.; Facchini, M. C.; Decesari, S.; Mircea, M.; Emblico, L.; Fuzzi, S.; Ceburnis, D.; Yoon, Y. J.; O'Dowd, C. D.; Putaud, J. P.; Dell'Acqua, A., *Journal of Geophysical Research - Atmospheres* **2004,** *109*.

45. Havers, N.; Burba, P.; Lambert, J.; Klockow, D., *Journal of Atmospheric Chemistry* **1998,** *29*, 45-54.

46. Facchini, M. C.; Mircea, M.; Fuzzi, S.; Charlson, R. J., *Nature* **1999,** *401*, 257-259.

47. Zappoli, S.; Andracchio, A.; Fuzzi, S.; Facchini, M. C.; Gelencser, A.; Kiselev, A.; Krivacsy, Y., *Atmospheric Environment* **1999,** *33*, 2733-2743.

48. Mayol-Bracero, O. L.; Guyon, P.; Graham, B.; Roberts, G.; Andreae, M. O.; Decesari, S.; Facchini, M. C.; Fuzzi, S.; Artaxo, P., *Journal of Geophysical Research* **2002,** *107* (D20).

49. Decesari, S.; Fuzzi, S.; Facchini, M. C.; Mircea, M.; Emblico, L.; Cavalli, F.; Maenhaut, W.; Chi, X.; Schkolnik, G.; Falkovich, A. H.; Rudich, Y.; Claeys, M.; Pashynska, V.; Vas, G.; Kourtchev, I.; Vermeylen, R.; Hoffer, A.; Andreae, M. O.; Tagliavini, E.; Moretti, F.; Artaxo, P., *Atmospheric Chemistry and Physics* **2006,** *6*.

50. Graber, E. R.; Rudich, Y., *Atmospheric Chemistry and Physics* **2006,** *6*, 729-753.

51. Hung, H.-M.; Katrib, Y.; Martin, S. T., *Journal of Physical Chemistry A* **2005,** *109*.

52. Zahardis, J.; LaFranchi, B. W.; Petrucci, G. A., *Atmospheric Environment* **2006,** *40*.

53. Jang, M.; Czoschke, N. M.; Kamens, R. M., *Science* **2002,** *298*.

54. Tolocka, M. P.; Jang, M.; Ginter, J. M.; Cox, F. J.; Kamens, R. M.; Johnston, M. V., *Environmental Science & Technology* **2004,** *38*.

55. Baltensperger, U.; Kalberer, M.; Dommen, J.; Paulsen, D.; Alfarra, M. R.; Coe, H.; Fisseha, R.; Gascho, A.; Gysel, M.; Nyeki, S.; Sax, M.; Steinbacher, M.; Prevot, A. S. H.; Sjogren, S.; Weingartner, E.; Zenobi, R., *Faraday Discussions* **2005,** *130*, 265-278.

56. Kalberer, M.; Paulsen, D.; Sax, M.; Steinbacher, M.; Dommen, J.; Prevot, A. S. H.; Fisseha, R.; Weingartner, E.; Frankevich, V.; Zenobi, R.; Baltensperger, U., *Science* **2004,** *303*, 1659-1662.

57. Holmes, B. J.; Petrucci, G. A., *Journal of Atmospheric Chemistry* **2007,** *58*.

58. Limbeck, A.; Handler, M.; Neuberger, B.; Klatzer, B.; Puxbaum, H., *Analytical Chemistry* **2005,** *77*, 7288-7293.

59. Havers, N.; Burba, P.; Klockow, D.; Kockow-Beck, A., *Chromatographia* **1998,** *47*, 619-624.

60. Kiss, G.; Tombacz, E.; Hansson, H. C., *Journal of Atmospheric Chemistry* **2005,** *50*, 279-294.

61. Hsu, C.-L.; Ding, W.-H., *Talanta* **2009,** *80*, 1025-1028.

62. Hsieh, L.-Y.; Kuo, S.-C.; Chen, C.-L.; Tsai, Y. I., *Atmospheric Environment* **2009,** *43*, 4396-4406.

63. Miyazaki, Y.; Aggarwal, S. G.; Singh, K.; Gupta, P. K.; Kawamura, K., *J. Geophys. Res.* **2009,** *114*.

64. Martinelango, P. K.; Dasgupta, P. K.; Al-Horr, R. S., *Atmospheric Environment* **2007,** *41*, 4258-4269.

65. Legrand, M.; Preunkert, S.; Gally-Lacaux, C.; Liousse, C.; Wagenbach, D., *J. Geophys. Res.* **2005,** *110*.

66. Sorooshian, A.; Varutbangkul, V.; Brechtel, F. J.; Ervens, B.; Feingold, G.; Bahreini, R.; Murphy, S. M.; Holloway, J. S.; Atlas, E. L.; Buzorius, G.; Jonsson, H.; Flagan, R. C.; Seinfeld, J. H., *J. Geophys. Res.* **2006,** *111*.

67. Kundu, S.; Kawamura, K.; Andreae, T. W.; Hoffer, A.; Andreae, M. O., *Atmospheric Chemistry and Physics* **2010,** *10*, 2209-2225.

68. Li, M.; Chen, H.; Yang, X.; Chen, J.; Li, C., *Atmospheric Environment* **2009,** *43*, 2717-2720.

69. Yang, F.; Chen, H.; Wang, Z.; Yang, X.; Du, J.; Chen, J., *Atmospheric Environment* **2009,** *43*, 3876-3882.

70. Yang, L.; Ray, M. B.; Yu, L. E., *Atmospheric Environment* **2008,** *42*, 856-867.

71. Yang, L.; Ray, M. B.; Yu, L. E., *Atmospheric Environment* **2008,** *42*, 868-880.

72. Ervens, B.; Carlton, A. G.; Turpin, B. J.; Altieri, K. E.; Kreidenweis, S. M.; Feingold, G., *Geophysical Research Letters* **2008,** *35*.

73. Chen, J.; Griffin, R. J.; Grini, A.; Tulet, P., *Atmospheric Chemistry and Physics* **2007,** *7*, 5343-5355.

74. Carlton, A. G.; Turpin, B. J.; Altieri, K. E.; Seitzinger, S.; Reff, A.; Lim, H.-J.; Ervens, B., *Atmospheric Environment* **2007,** *41* (7588-7602).

75. Ervens, B.; Feingold, G.; Frost, G. J.; Kreidenweis, S. M., *J. Geophys. Res.* **2004,** *109*.

76. Tan, Y.; Perri, M. J.; Seitzinger, S. P.; Turpin, B. J., *Environ. Sci. Technol.* **2009,** *43*, 8105-8112.

77. Prenni, A. J.; DeMott, P. J.; Kreidenweis, S. M.; Sherman, D. E., *J. Phys. Chem. A* **2001,** *106=5*, 11240-11248.

78. Sullivan, R. C.; Moore, M. J. K.; Petters, M. D.; Kreidenweis, S. M.; Roberts, G. C.; Prather, K. A., *Atmospheric Chemistry and Physics* **2009,** *9*, 3303-3316.

79. Sorjamaa, R.; Laaksonen, A., *Atmospheric Chemistry and Physics* **2007,** *7*, 8141-8158.

80. Gibson, E. R. Ph. D. Dissertation. University of Iowa, 2007.

81. Gibson, E. R.; Hudson, P. K.; Grassian, V. H., *J. Phys. Chem. A* **2006,** *110*, 11785-11799.

82. Wiedensohler, A., *J. Aerosol Sci.* **1988,** *19* (3), 387-9.

83. Wiedensohler, A.; Luetkemeier, E.; Feldpausch, M.; Helsper, C., *J. Aerosol Sci.* **1986,** *17* (3), 413-16.

84. Hinds, W. C., *Aerosol Technology: properties, behavior, and measurement of airborne particles*. 2nd ed.; Wiley: New York, 1999.

85. Knutson, E. O.; Whitby, K. T., *J. Aerosol Sci.* **1975,** *6* (6), 443-451.

86. Roberts, G.; Nenes, A., *Aerosol Sci. Technol.* **2005,** *39*, 206-221.

87. Tang, I. N.; Munkelwitz, H. R., *J. Geophys. Res.* **1994,** *99*, 18801.

88. Schuttlefield, J.; Al-Hosney, H.; Zachariah, A.; Grassian, V. H., *Appl. Spectrosc.* **2007,** *61*.

89. Sauerbrey, G., *Zeitschrift fur Physik* **1959,** *155*, 206-222.

90. Calace, N.; Petronio, B. M.; Cini, R.; Stortini, A. M.; Pampaloni, B.; Udisti, R., *Int. J. Environ. An. Ch.* **2001,** *79*.

91. Dinar, E.; Mentel, T. F.; Rudich, Y., *Atmospheric Chemistry and Physics* **2006,** *6*.

92. Wex, H.; Hennig, T.; Salma, I.; Ocskay, R.; Kiselev, A.; Henning, S.; Massling, A.; Wiedensohler, A.; Stratmann, F., *Geophysical Research Letters* **2007,** *112*.

93. Dinar, E.; Taraniuk, I.; Graber, E. R.; Anttila, T.; Mentel, T. F.; Rudich, Y., *Journal of Geophysical Research - Atmospheres* **2007,** *112*.

94. Hoffer, A.; Gelencser, A.; Guyon, P.; Kiss, G.; Schmid, O.; Frank, G. P.; Artaxo, P.; Andreae, M. O., *Atmospheric Chemistry and Physics* **2006,** *6*.

95. Dinar, E.; Taraniuk, I.; Graber, E. R.; Katsman, S.; Moise, T.; Anttila, T.; Mentel, T. F.; Rudich, Y., *Atmospheric Chemistry and Physics* **2006,** *6*, 2465-2481.

96. Samburova, V.; Zenobi, R.; Kalberer, M., *Atmospheric Chemistry and Physics* **2005,** *5*, 2163-2170.

97. Timonen, H. J.; Saarikoski, S. K.; Aurela, M. A.; Saarnio, K. M.; Hillamo, R. E. J., *Boreal Environ. Res.* **2008,** *13*.

98. Sjogren, S.; Gysel, M.; Weingartner, E.; Baltensperger, U.; Cubison, M. J.; Coe, H.; Zardini, A. A.; Marcolli, C.; Krieger, U. K.; Peter, T., *Journal of Aerosol Science* **2007,** *38*, 157-171.

99. Petters, M. D.; Kreidenweis, S. M., *Atmos. Chem. Phys.* **2007,** *7*.

100. Petters, M. D.; Kreidenweis, S. M., *Atmos. Chem. Phys.* **2008,** *8*.

101. Badger, C. L.; George, I.; Griffiths, P. T.; Braban, C. F.; Cox, R. A.; Abbatt, J. P. D., *Atmospheric Chemistry and Physics* **2006,** *6*, 755-768.

102. Gysel, M.; Weingartner, E.; Nyeki, S.; Paulsen, D.; Baltensperger, U.; Galambos, L.; Kiss, G., *Atmospheric Chemistry and Physics* **2004,** *4*, 35-50.

103. Brooks, S. D.; DeMott, P. J.; Kreidenweis, S. M., *Atmospheric Environment* **2004,** *38*, 1859-1868.

104. Svenningsson, B.; Rissler, J.; Swietlicki, E.; Mircea, M.; Bilde, M.; Facchini, M. C.; Decesari, S.; Fuzzi, S.; Zhou, J.; Monster, J.; Rosenorn, T., *Atmospheric Chemistry and Physics* **2006,** *6*.

105. Malcolm, R. I.; MacCarthy, P., *Environmental Science & Technology* **1986,** *20*.

106. Kokkola, H.; Sorjamaa, R.; Peraniemi, A.; Raatikainen, T.; Laaksonen, A., *Geophysical Research Letters* **2006,** *33*.

107. Fu, H.; Quan, X., *Chemosphere* **2006,** *63*.

108. Li, D.; Gaussoin, R., *USGA Turfgrass and Environ. Res. Online* **2008,** *7*.

109. Lumsdon, D. G.; Fraser, A. R., *Environmental Science & Technology* **2005,** *39*.

110. Socrates, G., *Infrared and Raman Characteristic Group Frequencies: Tables and Charts*. 3rd ed.; Wiley: Chichester, 2001.

111. Socrates, G., *Infrared Characteristic Group Frequencies Tables and Charts*. Wiley: New York, 1994.

112. Silverstein, R. M.; Morrill, T. C.; Bassler, G. C., *Spectrometric Identification of Organic Compounds*. Wiley: New York, 1991.

113. Duarte, R. M. B. O.; Santos, E. B. H.; Pio, C. A.; Duarte, A. C., *Atmospheric Environment* **2007,** *41*.

114. Yoon, T. H.; Johnson, S. B.; Brown Jr., G. E., *Langmuir* **2005,** *21*.

115. Hoffer, A.; Kiss, G.; Blazso, M.; Gelencser, A., *Geophysical Research Letters* **2004,** *31*.

116. Wex, H.; Kiselev, A.; Stratmann, F.; Zoboki, J.; Brechtel, F., *Journal of Geophysical Research - Atmospheres* **2005,** *110*.

117. Cruz, C. N.; Pandis, S. N., *Atmospheric Environment* **1997,** *31*, 2205-2214.

118. Cruz, C. N.; Pandis, S. N., *Journal of Geophysical Research - Atmospheres* **1998,** *103*, 13111-13123.

119. Corrigan, C. E.; Novakov, T., *Atmospheric Environment* **1999,** *33*, 2661-2668.

120. Raymond, T. M.; Pandis, S. N., *Journal of Geophysical Research - Atmospheres* **2002,** *107*.

121. Choi, M. Y.; Chan, C. K., *Environmental Science & Technology* **2002,** *36*, 2422-2428.

122. Hameri, K.; Charlson, R. J.; Hansson, H. C., *AlChE Journal* **2002,** *48*, 1309-1316.

123. Wise, M. E.; Surratt, J. D.; Curtis, D. B.; Shilling, J. E.; Tolbert, M. A., *Journal of Geophysical Research - Atmospheres* **2003,** *108*.

124. Topping, D. O.; McFiggans, G.; Coe, H., *Atmospheric Chemistry and Physics* **2005,** *5*, 1223-1242.

125. Bilde, M.; Svenningsson, B., *Tellus Series B - Chemical and Physical meteroloty* **2004,** *56*, 128-134.

126. Abbatt, J. P. D.; Broekhuzien, K.; Kumar, P. P., *Atmospheric Environment* **2005,** *39*, 4767-4778.

127. Dinar, E.; Rizig, A.; Spindler, C.; Erlick, C.; Kiss, G.; Rudich, Y., *Faraday Discussions* **2007,** *137*.

128. Abdul-Razzak, H.; Ghan, S. J., *Journal of Geophysical Research - Atmospheres* **2004,** *109*.

129. Hudson, P. K.; Gibson, E. R.; Young, M. A.; Kleiber, P. D.; Grassian, V. H., *Aerosol Science and Technology* **2007,** *41*, 701-710.

130. In *CRC Handbook of Chemistry and Physics*, Lide, D. R., Ed. CRC Press: Boca Raton, 2004.

131. Hatch, C. D.; Gough, R. V.; Tolbert, M. A., *Atmospheric Chemistry and Physics* **2007,** *7*, 1-14.

132. Al-Hosney, H. A.; Grassian, V. H., *Physical Chemistry Chemical Physics* **2005,** *7*, 1266-1276.

133. Gustafsson, R. J.; Orlov, A.; Badger, C. L.; Griffiths, P. T.; Cox, R. A.; Lambert, R. M., *Atmospheric Chemistry and Physics* **2005,** *5*, 3415-3421.

134. Dusek, U.; Reischl, G. P.; Hitzenberger, R., *Environ. Sci. Technol.* **2006,** *40*, 1223-1230.

135. Kollist-Siigur, K.; Nielson, T.; Gron, C.; Hansen, P. E.; Helweg, C.; Jonassen, K. E. N.; Jorgensen, O.; Kirso, U., *Journal of Environmental Quality* **2001,** *30*, 526-537.

136. Rosenorn, T.; Kiss, G.; Blide, M., *Atmospheric Environment* **2006,** *40*, 1794-1802.

137. Xue, H.; Khalizov, A. F.; Wang, L.; Zheng, J.; Zhang, R., *Phys. Chem. Chem. Phys.* **2009,** *11*, 7869-7875.

138. Hatch, C. D.; Gierlus, K. M.; Zahardis, J.; Schuttlefield, J.; Grassian, V. H., *Environmental Chemistry* **2009,** *6*, 380-388.

139. Koehler, K. A.; Kreidenweis, S. M.; DeMott, P. J.; Petters, M. D.; Prenni, A. J.; Carrico, C. M., *Geophysical Research Letters* **2009,** *36* (L08805).

140. Ouyang, J.-M.; Deng, S.-P.; Zhou, N.; Tieke, B., *Colloids and Surfaces A* **2005,** *256*, 21-27.